

# Lithium depletion boundary, stellar associations, and Gaia<sup>★</sup>

F. J. Galindo-Guil<sup>1,2</sup>, D. Barrado<sup>3</sup>, H. Bouy<sup>4</sup>, J. Olivares<sup>4,5</sup>, A. Bayo<sup>6,7,8</sup>, M. Morales-Calderón<sup>3</sup>, N. Huélamo<sup>3</sup>, L. M. Sarro<sup>9</sup>, P. Rivière-Marichalar<sup>10</sup>, H. Stoev<sup>11</sup>, B. Montesinos<sup>3</sup>, and J. R. Stauffer<sup>12,†</sup> **★★**

<sup>1</sup> Nordic Optical Telescope, Rambla José Ana Fernández Pérez 7, E-38711 San Antonio, Breña Baja, Santa Cruz de Tenerife, Spain.

<sup>2</sup> Centro de Estudios de Física del Cosmos de Aragón (CEFCA), Plaza San Juan 1, 44001 Teruel, Spain.

<sup>3</sup> Departamento de Astrofísica, Centro de Astrobiología (CAB, CSIC-INTA), ESAC Campus, Camino Bajo del Castillo s/n, 28692 Villanueva de la Cañada, Madrid, Spain.

<sup>4</sup> Laboratoire d'astrophysique de Bordeaux, Univ. Bordeaux, CNRS, B18N, Allée Geoffroy Saint-Hilaire, 33615 Pessac, France.

<sup>5</sup> Instituto de Astrofísica de Canarias, E-38205 La Laguna, Tenerife, Spain; Universidad de La Laguna, Dpto. Astrofísica, E-38206 La Laguna, Tenerife, Spain.

<sup>6</sup> Inst. Física y Astronomía, Fac. Ciencias, Universidad de Valparaíso, Gran Bretaña 1111, Valparaíso, Chile.

<sup>7</sup> Núcleo Milenio Formación Planetaria - NPF, Valparaíso, Chile

<sup>8</sup> European Organisation for Astronomical Research in the Southern Hemisphere (ESO), Karl-Schwarzschild-Str. 2, 85748, Garching bei München, Germany.

<sup>9</sup> Departamento de Inteligencia Artificial, UNED, Juan del Rosal 16, 28040 Madrid, Spain.

<sup>10</sup> Observatorio Astronómico Nacional (OAN-IGN) – Observatorio de Madrid, Alfonso XII, 3, 28014 Madrid, Spain.

<sup>11</sup> Fundación Galileo Galilei – INAF, Rambla José Ana Fernández Pérez 7, 38712 Breña Baja, Santa Cruz de Tenerife, Spain.

<sup>12</sup> Spitzer Science Center, California Institute of Technology, Pasadena, CA 91125, USA.

May 16, 2022

## ABSTRACT

**Context.** Stellar ages are key to improving our understanding of different astrophysical phenomena. However, many techniques to estimate stellar ages are highly model-dependent. The lithium depletion boundary (LDB), based on the presence or absence of lithium in low-mass stars, can be used to derive ages in stellar associations of between 20 and 500 Ma.

**Aims.** The purpose of this work is to revise former LDB ages in stellar associations in a consistent way, taking advantage of the homogeneous *Gaia* parallaxes as well as bolometric luminosity estimations that do not rely on monochromatic bolometric corrections.

**Methods.** We studied nine open clusters and three moving groups characterised by a previous determination of the LDB age. We gathered all the available information from our data and the literature: membership, distances, photometric data, reddening, metallicity, and surface gravity. We re-assigned membership and calculated bolometric luminosities and effective temperatures using distances derived from *Gaia* DR2 and multi-wavelength photometry for individual objects around the former LDB. We located the LDB using a homogeneous method for all the stellar associations. Finally, we estimated the age by comparing it with different evolutionary models.

**Results.** We located the LDB for the twelve stellar associations and derived their ages using several theoretical evolutionary models. We compared the LDB ages among them, along with data obtained with other techniques, such as isochrone fitting, ultimately finding some discrepancies among the various approaches. Finally, we remark that the 32 Ori MG is likely to be composed of at least two populations of different ages.

**Conclusions.**

**Key words.** open clusters and associations: general – stars: fundamental parameters, low-mass stars, brown dwarfs

## 1. Introduction

One of the most fundamental parameters necessary for the characterisation of any astrophysical object, from planets, stars, and galaxies up through the whole universe, is age. There are only two true pillars holding up the scale of astrophysical age. The first is the age of the Sun, which comes from radiometric measurements of the oldest Solar System material, which yields  $4.55 \pm 0.07$  Ga (see Patterson 1956 or the recent value  $4.5672 \pm 0.6$  Ga from Amelin et al. 2002). The second is the age of the universe, with an estimate of 13.8 Ga, based on the Lambda cold

dark matter cosmological model ( $\Lambda$ CDM, Planck Collaboration et al. 2020).

All other ages are subject to significant uncertainties, and their determinations face multiple observational and theoretical challenges. Ages are generally better determined in stellar associations<sup>1</sup> than in isolated stars and, more precisely, open clusters are very convenient for this purpose. They usually provide a significant sample of objects when testing the hypothesis that they were born simultaneously from the same molecular cloud and with an identical composition. Two excellent and complete sum-

Send offprint requests to: pgalindo@hotmail.cl; pgalindo@cefca.es

\* Table E.4. is only available in electronic form at the CDS via anonymous ftp to cdsarc.u-strasbg.fr (130.79.128.5) or via <http://cdsweb.u-strasbg.fr/cgi-bin/qcat?J/A+A/>

\*\* † Deceased : <https://baas.aas.org/pub/2021i0306/release/1>

<sup>1</sup> We use the term stellar association to refer both to open clusters and moving groups. A moving group is a stream of stars with common age and motion through the Milky Way and with no overdensity of stars discernible in any region (Zuckerman & Song 2004). An open cluster is a group of gravitationally bound stars that shows a clear concentration above the surrounding stellar background (Moraux 2016).

maries of techniques for estimating ages in ensembles of stars can be found in Mermilliod (2000) and Soderblom (2010).

There are several methods and techniques aimed at assigning ages at present, however, each of them is valid within a specific age interval. Ages can vary as much as 50% depending on the technique, as in the case of stellar associations with ages below 150 Ma (see Stauffer et al. 1995b or Barrado y Navascués et al. 1999a). Even when using the same technique, there can be broad variations depending solely on the different grids of theoretical models.

Several features and characteristics are taken into account when deriving ages in stellar associations. The isochrone fitting technique is the most widely used since it covers all ages and masses, making use of colour-magnitude or Hertzsprung-Russell diagrams (HRDs). The turn-off isochrone fitting consists of reproducing the morphology of the cluster sequence close to the turn-off region, which is where stars are approaching the end of hydrogen burning at their core. The pre-main-sequence (PMS) isochrone fitting consists of reproducing the position of PMS stars in the cluster. However, there are significant deviations between ages derived using PMS stars still contracting onto the main sequence, and high-mass ones that have already evolved away from it (Lyra et al. 2006, Naylor 2009). These differences can be due to the effects of binarity and rotation of the upper main-sequence stars (Mermilliod 2000) or due to the fact that the effective temperatures predicted by current PMS evolutionary models are overestimated due to the magnetic fields and star-spots (D'Antona et al. 2000, Stauffer et al. 2003, Jackson & Jeffries 2014b, and Franciosini et al. 2022). The rotation of massive stars increases the estimated age of a stellar association about 25% (Meynet & Maeder 2000), with this effect being more pronounced in younger associations, such as Alpha Persei and the Pleiades, than in older ones such as Coma Berenices, Praesepe, or the Hyades (Maeder 1971). The isochrone fitting ages estimated from models that take into account the magnetic field are systematically higher than those estimated from models that ignore this effect (Malo et al. 2014b).

There are other methods used to derive stellar ages. The kinematic age technique is based on the motions of a group of stars due to its expansion from their birthplace without experiencing any forces (see the seminal works from Ambartsumian 1947 and 1949, Blaauw 1946, and 1964, and the subsequent works with a refined methodology: Brown et al. 1997b or Miret-Roig et al. 2018). This technique is applicable to stellar associations younger than 20 Ma (Soderblom 2010).

The Strömgren photometric system  $uvby\beta$  allows us to derive effective temperatures and surface gravities for BAF-type stars and they are used to estimate the age comparing with theoretical evolutionary tracks (see Song et al. 2001 and David & Hillenbrand 2015). Also, the strength of gravity-sensitive spectrophotometric features is an age proxy in stellar associations within the 5 to 15 Ma range, with an uncertainty of 2 Ma (Lawson et al. 2009). Another technique, namely, gyrochronology, derives ages for main-sequence and low-mass stars using their rotation periods and colours, for ages older than 600 Ma (Barnes 2007). Finally, the white dwarf cooling age exploits the slope and position of its thermal evolution relative to the main-sequence with an age range of validity from 150 Ma to 4 Ga (De Gennaro et al. 2009).

The lithium depletion boundary (LDB) is a technique that allows for an independent age determination for a stellar association (Basri et al. 1996), valid for values between 20 to few hundred Ma. It is based on the presence or absence of lithium in low-mass stars and brown dwarfs (Rebolo et al. 1992). Lithium burns inside the stellar nucleus (D'Antona & Mazzitelli 1984)

and stars with masses below about  $0.3M_\odot$  are fully convective. The convection makes that the lithium surface abundance to decrease with age, and for low-mass objects, the decay is very rapid. For masses below  $\sim 0.07M_\odot$  (depending on the evolutionary theoretical model), the core temperature is never hot enough to destroy it, and its abundance (both internal or in the stellar or sub-stellar atmosphere) remains the same. The burning process is so fast and depends so strongly on mass that there is a sharp boundary between lithium-rich and lithium-poor members (D'Antona & Mazzitelli 1994, Bildsten et al. 1997, and Ushomirsky et al. 1998). The LDB technique was successfully applied to the Pleiades (Stauffer et al. 1998a) and Alpha Persei (Stauffer et al. 1999) clusters, and since then, this method has been used in a dozen of stellar associations.

Similarly to other model-dependant techniques, the LDB age is also affected by possibly assumptions made in the input physics of the stellar models it relies on (Jeffries & Naylor 2001, Burke et al. 2004, and Tognelli et al. 2015). The expected uncertainties on LDB age depends on the luminosity of the star at the LBD, ranging from about 3% percent for faint old stars to about 15% for brighter young stars (Burke et al. 2004 and Tognelli et al. 2015). In addition, the LDB technique is indirectly affected by other uncertainties: (a) stellar distances, (b) the contamination by field stars, (c) the transformation from observational quantities, magnitude, and colours, as well as theoretical ones such as bolometric luminosities and effective temperatures (Jeffries & Naylor 2001), (d) the presence of binaries or multiple systems, (e) the magnetic activity and rotation of the objects (Soderblom et al. 1993, Chabrier et al. 2007, Malo et al. 2014b), (f) the identification of a significant number of low-mass cluster members within a small magnitude range, and (g) the low quality and/or low resolution of the used stellar spectra.

The availability of photometric all-sky or wide sky surveys, such as *Gaia* DR2 (Gaia Collaboration et al. 2018a), SDSS (Alam et al. 2015), 2MASS (Skrutskie et al. 2006), WISE (Cutri 2013), or Pan-STARRS (Chambers 2017) has signalled the dawning of a new era and allowed us to address several of the factors mentioned above from a new perspective. The high-quality astrometric data of *Gaia* DR2 represent a significant advance for at least three reasons: they allow us (a) to calculate, for the first time, individual distances for each low-mass cluster member, (b) to refine the membership criteria, and in some cases (c) to determine whether an object is a multiple system. Furthermore, the use of wide-area multi-wavelength imaging surveys with ranges from ultraviolet to infrared allows us to calculate the total flux of each object without assuming any monochromatic bolometric correction, which is a noteworthy source of systematic uncertainties in the LDB age. Empirical bolometric corrections are derived from main-sequence stars and our objects have different  $\log g$  values; in addition, bolometric corrections vary as a function of metallicity, especially for temperatures less than 3 000 K (Jeffries & Naylor 2001, Burke et al. 2004, and Tognelli et al. 2015).

In this work, we present, for the first time, a homogeneous analysis for all the stellar associations with former LDB ages aimed at creating a complete set of an LDB age scale. This analysis includes new photometric data in a broad range of wavelengths, individual accurate parallaxes from *Gaia* DR2, and the effects of metallicity and gravity. The work is structured as follows. In Section 2, we introduce the stellar associations under consideration. We provide information of the data and evolutionary models used in Section 3. Section 4 shows the method scheme in detail. We analyse each stellar association, explain additional information from literature, identify outliers, and lo-



2001). It is an open cluster with similar age and distance to IC 2602 (Stauffer et al. 1997), but they are located in different sky regions, see Fig.6. Several works have studied both clusters in a parallel way: Stauffer et al. (1997), Randich et al. (2001), and D’Orazi & Randich (2009)

The IC 2391 age ranges between 25 to 50 Ma: 36.3 Ma (Mermilliod 1981), 25 to 35 Ma isochrone fitting age (Stauffer et al. 1997), 40–45 Ma (Randich et al. 2018), and  $36.4^{+2.0}_{-2.0}$  Ma, assuming  $(m - M)_0 = 5.91$  mag and  $A_V = 0.09$  mag (Bossini et al. 2019).

The LDB age was initially estimated by Barrado y Navascués et al. (1999a):  $53 \pm 5$  Ma, assuming  $A_I = 0.02$  mag and  $(m - M)_0 = 5.95 \pm 0.1$  mag. A further refinement in Barrado y Navascués et al. (2004) produced a value of  $50 \pm 5$  Ma, assuming the same distance and  $E(B - V) = 0.06$  mag. Burke et al. (2004) calculated an age of  $48 \pm 5$  Ma, using a  $(m - M) = 5.95 \pm 0.10$  mag and  $A_I = 0.02 \pm 0.02$  mag. Randich et al. (2018) re-computed the LDB age using  $(m - M)_0 = 5.82 \pm 0.10$  mag and  $E(B - V) = 0.088 \pm 0.027$  mag:  $51.3^{+5.0}_{-4.5}$  Ma.

## 2.7. The Pleiades

The Pleiades cluster is located at 136 pc ( $7.364 \pm 0.005$  mas),  $E(B - V) = 0.045$  mag, and an age of  $110^{+22}_{-14}$  Ma (Gaia Collaboration et al. 2018b). Metallicity values, [Fe/H], range from  $-0.034 \pm 0.024$  (Boesgaard & Friel 1990) to  $0.06 \pm 0.06$  (Gebran & Monier 2008). Excellent summaries of previous works can be found in Stauffer et al. (2007), Bouy et al. (2015), and Lodieu et al. (2019a).

Although it has been widely studied, its distance and age have been a matter of controversy, ranging the distance between 115 to 140 pc, depending on the work and the technique used:  $115.9 \pm 2.7$  pc (van Leeuwen & Hansen Ruiz 1997),  $131.8 \pm 2.5$  pc (Pinsonneault et al. 1998),  $139.1 \pm 3.5$  pc (Southworth et al. 2005),  $120.2 \pm 1.9$  pc assuming  $E(B - V) = 0.04$  mag (van Leeuwen 2009),  $136.2 \pm 1.2$  pc (Melis et al. 2014), and  $134.4^{+2.9}_{-2.8}$  pc (Galli et al. 2017). The age ranges between 70 to 150 Ma: 77.6 Ma (Mermilliod 1981), 150 Ma (Mazzei & Pigatto 1989) 100 Ma, assuming  $(m - M)_0 = 5.60$  mag and  $E(B - V) = 0.04$  mag (Meynet et al. 1993),  $70 \pm 10$  Ma (Stauffer et al. 1995a)<sup>2</sup>,  $115^{+3}_{-11}$  Ma, assuming  $(m - M)_0 = 5.35$  mag and  $E(B - V) = 0.02$  mag (Naylor 2009),  $132 \pm 2$  Ma (Bell et al. 2014),  $134^{+9}_{-10}$  Ma (Cargile et al. 2014),  $86^{+6}_{-3}$  Ma, assuming  $(m - M)_0 = 5.67$  mag and  $A_V = 0.14$  mag (Bossini et al. 2019), and  $132^{+26}_{-27}$  Ma, assuming  $E(B - V) = 0.045$  mag (Lodieu et al. 2019a).

Basri et al. (1996) attempted to determine the LDB age and reported a lower limit of  $\sim 115$  Ma based on the detection of lithium in the binary system PPL-15 (Basri & Martín 1999b). Later, the exhaustive study of Stauffer et al. (1998b), yielded a value of  $125 \pm 8$  Ma assuming  $(m - M)_0 = 5.60$  mag and  $A_I = 0.06$  mag. In addition, Barrado y Navascués et al. (2004) re-calculated the value at  $130 \pm 20$  Ma, whereas Burke et al. (2004) re-calculated an age of  $126 \pm 11$  Ma, both using a  $(m - M) = 5.60 \pm 0.10$  mag and  $A_I = 0.06 \pm 0.03$  mag. Finally, Dahm (2015) derived an age of  $112 \pm 5$  Ma, assuming  $136.2 \pm 1.2$  pc (Melis et al. 2014) and  $A_V = 0.12$  mag,  $A_I = 0.06$  mag,  $A_J = 0.03$  mag, and  $A_K = 0.01$  mag.

<sup>2</sup> The uncertainty is an estimate from their Figure 5c and 5d.

## 2.8. Blanco 1

Blanco 1 is located at 237 pc with  $E(B - V) = 0.001$  mag and an age of  $115^{+23}_{-15}$  Ma (Gaia Collaboration et al. 2018b)<sup>3</sup>. It has an estimated metallicity of  $[Fe/H] = +0.03 \pm 0.07$  (Netopil et al. 2016). The age ranges between 90 to 200 Ma:  $90 \pm 25$  Ma (Panagi & O’dell 1997),  $80 \pm 20$  Ma (Cargile et al. 2009, assuming  $240 \pm 10$  pc and  $E(B - V) = 0.016$  mag),  $94^{+5}_{-7}$  Ma (Bossini et al. 2019, assuming  $(m - M)_0 = 6.876$  mag and  $A_V = 0.031$  mag), and  $146^{+13}_{-14}$  Ma (Cargile et al. 2014).

Cargile et al. (2010) identified the LDB at  $\log L_{bol} = -2.94 \pm 0.12 L_\odot$  or  $\log L_{bol} = -2.90 \pm 0.09 L_\odot$  (depending on monochromatic bolometric corrections) and determined an age of  $132 \pm 24$  Ma, assuming a distance modulus of  $6.58 \pm 0.12$  mag and  $E(I - K_s) = 0.02$  mag ( $A_I = 0.03$  mag). Later, Juarez et al. (2014) used empirical activity corrections to investigate the effects of magnetic activity on the LDB age. They updated the LDB age to  $126^{+13}_{-14}$  Ma, and taking into account the activity, they gave a value of  $114^{+9}_{-10}$  Ma.

## 2.9. The Hyades

The Hyades cluster is the nearest open cluster to the Sun, 45 pc (de Bruijne et al. 2001). It has an estimated age of  $625 \pm 50$  Ma (Perryman et al. 1998) and  $[Fe/H] = +0.127 \pm 0.022$  (Boesgaard & Friel 1990). Metallicity ranges from  $[Fe/H] = +0.05 \pm 0.05$  (Gebran et al. 2010) to  $[Fe/H] = +0.13 \pm 0.05$ , derived using 61 sources (Netopil et al. 2016). Additional information can be found in Perryman et al. (1998) and Lodieu et al. (2019b). Recently, Meingast & Alves (2019) and Röser et al. (2019) reported the detection of the tidal tails. The age ranges between 500 to 1200 Ma: 661 Ma (Mermilliod 1981), an age range between 500 to 1000 Ma (Eggen 1998),  $648 \pm 45$  Ma (De Gennaro et al. 2009), 800 Ma (Brandt & Huang 2015),  $794^{+161}_{-102}$  Ma (Gaia Collaboration et al. 2018b), and  $640^{+67}_{-49}$  Ma (Lodieu et al. 2019b) Martín et al. (2018) identified the LDB in the Hyades and derived an age of  $650 \pm 70$  Ma. More recently, Lodieu et al. (2018) re-analysed the age adding to the study the source 2M0418 and inferred an age range of 580–775 Ma (mean of 700 Ma) from the bolometric luminosity, and 580–950 Ma (mean of 760 Ma) from the effective temperature.

## 2.10. Beta Pictoris moving group

The Beta Pictoris moving group, hereafter BPMG, named after the star  $\beta$  Pictoris, is a  $20 \pm 10$  Ma co-moving group of stars (Barrado y Navascués et al. 1999b) with a metallicity of  $[Fe/H] = -0.01 \pm 0.08$  (Viana Almeida et al. 2009). Several studies have addressed the BPMG age with different results:  $20 \pm 10$  Ma (Barrado y Navascués et al. 1999b),  $12^{+8}_{-4}$  Ma (Zuckerman et al. 2001), 11.5 Ma (Ortega et al. 2002),  $\sim 12$  Ma (Song et al. 2003), 15 Ma (Torres et al. 2006),  $22 \pm 12$  Ma (Makarov 2007), an age range between  $13 \pm 5$  Ma to  $21 \pm 9$  Ma (Mentuch et al. 2008),  $22 \pm 3$  Ma (Mamajek & Bell 2014)  $24 \pm 3$  Ma (Bell et al. 2015) 40 Ma (Macdonald & Mullan 2010), an age range between 15 and 28 Ma (Malo et al. 2014b),  $13^{+7}_{-0}$  Ma (Miret-Roig et al. 2018) which was updated to  $18.5^{+2.0}_{-2.4}$  Ma (Miret-Roig et al. 2020).

<sup>3</sup> They also report an age of  $200^{+40}_{-26}$  Ma, but with this value the lower main sequence is poorly fitted.

<sup>4</sup> This metallicity value has been a matter of controversy, see: Westerlund et al. 1988, Edvardsson et al. (1995), and Ford et al. (2005).

Song et al. (2002) estimated the LDB in  $< 20$  Ma. Then, Binks & Jeffries (2014) added to the study eight low-mass members and re-calculated the age:  $21 \pm 4$  Ma with an additional model-dependent uncertainty of  $\pm 1$  Ma. Messina et al. (2016), after de-correlating the lithium equivalent width from the rotation period, calculated an age of  $25 \pm 3$  Ma using the hot side of the LDB. Finally, other LDB ages have also been calculated:  $\geq 30$  Ma (Yee & Jensen 2010),  $26 \pm 3$  Ma (Malo et al. 2014b) and  $22 \pm 6$  Ma (Shkolnik et al. 2017).

### 2.11. Tucanae-Horologium moving group

At first, the Tucanae-Horologium moving group (THMG) was identified as two separate associations: the Tucanae association (Zuckerman & Webb 2000) with ten co-moving stars placed at a distance  $\sim 45$  pc, and the Horologium association (Torres et al. 2000) located at  $\sim 60$  pc. Viana Almeida et al. (2009) reported a metallicity of  $[Fe/H] = -0.03 \pm 0.05$  using nine members. The age ranges between 5–45 Ma: 40 Ma (Zuckerman & Webb 2000),  $\sim 30$  Ma (Torres et al. 2000), an age range between 10–30 Ma (Stelzer & Neuhauser 2000),  $\sim 20$  Ma (Kraus et al. 2014),  $45 \pm 4$  Ma (Bell et al. 2015), and  $5_{-0}^{+23}$  Ma (Miret-Roig et al. 2018). Kraus et al. (2014) confirmed 129 new late-type members with spectral types between K3 to M6 and these authors calculated an LDB age of 40 Ma.

### 2.12. 32 Ori moving group

The 32 Ori moving group, (32 Ori MG, also known as Mamajek 3), was noticed as a group of X-ray-bright late-type stars from the ROSAT All-Sky Survey (Alcalá et al. 2000) with similar proper motions and moving with the massive binary 32 Ori (B5V+B7V). Mamajek (2007) defined the moving group with about ten sources and estimated an age of 25 Ma (with no technique specifically given).

Bell et al. (2015) calculated an isochronal fitting PMS age of  $22_{-3}^{+4}$  Ma adopting a distance of  $91.86 \pm 2.42$  pc for all the stars. With the new census, Bell et al. (2017) calculated a PMS isochronal fitting age of  $25 \pm 5$  Ma using  $E(B-V) = 0.03 \pm 0.01$  mag ( $A_V = 0.10 \pm 0.03$  mag) and the kinematic or trigonometric distances derived for each source.

Bell et al. (2017) calculated an LDB age of  $23 \pm 4$  Ma using  $E(B-V) = 0.03 \pm 0.01$  mag ( $A_V = 0.10 \pm 0.03$  mag) and the kinematic or trigonometric distances derived for each source. They combined both results, PMS age and LDB age, and released an age of  $24 \pm 4$  Ma ( $\pm 4$  Ma statistical and  $\pm 2$  Ma systematic).

## 3. Data and evolutionary models

### 3.1. Initial census for the stellar associations

Most of the open clusters we analysed here are included in the Gaia Collaboration et al. (2018b), so we have built the initial sample of cluster members with data from that work. There are two exceptions: NGC 1960 and 32 Ori MG. For these two, we selected the members from Cantat-Gaudin et al. (2018a) for NGC 1960 and Bell et al. (2017) for the 32 Ori MG.

We created a new list restricting to only members with measured lithium equivalent widths and close to the expected LDB – hereafter referred to as the LDB sample (see Table E.4.). The selected members must satisfy the following requirements: they should have available spectral data with enough resolving power ( $\mathcal{R} > 1\,000$ ) and a moderate signal-to-noise ratio ( $S/R > 20$ ) around the lithium feature located at  $6\,707.8$  Å, (see Figure A.2).

from Bayo et al. 2011). Unfortunately, the lithium data for the same cluster are not homogeneous, as they have been obtained by several authors using different analyses and with spectra with different resolving power or signal-to-noise ratio. We compiled the dataset using the astronomical databases *Astrophysics Data System* (ADS, Murray et al. 1992), SIMBAD (Egret et al. 1991), and VizieR (Ochsenbein et al. 2000).

### 3.2. Gaia DR2: parallaxes, proper motions, and photometry

The second *Gaia* (Gaia Collaboration et al. 2016) data release, hereafter *Gaia* DR2, is an all-sky survey catalogue with celestial positions and  $G$  photometry for approximately  $1.7 \cdot 10^9$  sources; for  $1.3 \cdot 10^9$  of those sources, parallaxes and proper motions are also available (Gaia Collaboration et al. 2018a). The quality and quantity of data released by *Gaia* DR2 are unprecedented. However, we should take into account some caveats related to the astrometry: a) all the sources have been considered as single stars; so, if an object is a multiple system it likely lacks an astrometric solution or its value is corrupted; b) some sources have negative parallaxes (see Luri et al. 2018); and c) objects with separations  $\sim 0.2 - 0.3''$  and not resolved in *Gaia* DR2 can contain spurious parallax values with small uncertainties.

The *Gaia* DR2 catalogue includes photometry in three optical bands  $G, G_{BP}, G_{RP}$ , with a bright limit of  $G \approx 3$  mag and a limiting magnitude of  $G = 21$  mag (Evans et al. 2018). The analysis from Maíz Apellániz & Weiler (2018) reports a systematic linear trend in the photometric system, for the range  $G \in [6, 16]$  mag, estimated to be  $3.5 \pm 0.3$  mmag mag $^{-1}$ . These values can be greater in crowded regions, in the vicinity of bright sources, and at values of  $G \geq 19$  mag. This mainly affects  $G_{BP}$  and to a lesser extent  $G_{RP}$ . Smart et al. (2019) indicated that for their sample of cool dwarfs (with spectral types ranging from M8 to T6),  $G_{BP}$  is heavily affected. So, our faintest and furthest sources might suffer from overestimation in this band. The flux-excess factor (named `phot_bp_rp_excess_factor` and included in the catalogue) gives a quantitative indication of this effect and can be used to filter out unreliable values (see recommendations from Evans et al. 2018).

We queried the *Gaia* DR2<sup>5</sup> archive without imposing any restriction, cross-matching the positions on the sky (right ascension and declination) from our sources using a  $2.5''$  radius. When finding two or more sources for the same input, we made certain which counterpart was the correct one and we carefully investigated the images and the entries using ESASky (Baines et al. 2017) and Aladin (Bonnarel et al. 2000). We followed a different approach for the Hyades and the MGs because we lost a lot of sources in the cross-matching. This was due to two factors: a) the proximity and high proper motion of the sources, and b) our input positions on the sky are in epoch 2000, while *Gaia* DR2 uses as reference epoch 2015.5. In such cases we identified each source using the 2MASS source name and the SIMBAD database, then we checked with ESASky and Aladin whether there was a *Gaia* DR2 counterpart or not. Once we knew the *Gaia* DR2 name, we obtained the rest of the quantities, astrometric and photometric data from the archive. Throughout this work, we performed the analysis with the *Gaia* DR2 data. However, we carried out an additional check with the *Gaia* EDR3 data (Gaia Collaboration et al. 2021).

<sup>5</sup> <https://gea.esac.esa.int/archive/>

**Table 1.** Data from the literature for the twelve stellar associations with LDB ages.

Stellar association	LDB age [Ma]	Ref.	Gaia Collaboration et al. (2018b)						[Fe/H] [dex]	Other age [Ma]	Ref.
			Age [Ma]	Ref.	Parallaxes [mas]	DM [mag]	d [pc]	E(B - V) [mag]			
Alpha Persei	90 ± 10 85 ± 10	(8) (7)	71 <sup>+21</sup> <sub>-18</sub>	(23)	5.718 ± 0.005	6.214	175	0.090	(23)	+0.14 ± 0.11	51.3 <sup>+12</sup> <sub>-8</sub>
NGC 1960	22 ± 4	(1)	25	(22)	0.835 ± 0.064	10.391	1 197	0.20	(26)	-	< 22.4
IC 4665	28 ± 4 23.2 <sup>+3.5</sup> <sub>-3.1</sub>	(2) (3)	38 <sup>+5</sup> <sub>-2</sub>	(22)	2.891 ± 0.003	7.694	346	0.17	(27)	-0.03 ± 0.08	36.3 <sup>+12</sup> <sub>-8</sub>
NGC 2547	35 ± 1 37.7 <sup>+5.7</sup> <sub>-4.8</sub>	(4) (3)	40 <sup>+11</sup> <sub>-10</sub>	(23)	2.543 ± 0.002	7.980	394	0.040	(23)	-0.01 ± 0.01	57 ± 5.7
IC 2602	46 <sup>+6</sup> <sub>-5</sub> 43.7 <sup>+4.3</sup> <sub>-3.9</sub>	(5) (3)	40 <sup>+11</sup> <sub>-10</sub>	(23)	6.571 ± 0.007	5.914	152	0.031	(23)	-0.02 ± 0.02	36.3 <sup>+12</sup> <sub>-8</sub>
IC 2391	53 ± 5 50 ± 5 51.3 <sup>+5.0</sup> <sub>-4.5</sub>	(6) (7) (3)	50 <sup>+14</sup> <sub>-13</sub>	(23)	6.597 ± 0.007	5.908	152	0.030	(23)	-0.01 ± 0.03	36.3 <sup>+12</sup> <sub>-8</sub>
The Pleiades	125 ± 8 130 ± 20 112 ± 5	(9) (7) (10)	110 <sup>+22</sup> <sub>-15</sub>	(23)	7.364 ± 0.005	5.667	136	0.045	(23)	-0.01 ± 0.05	77.6 <sup>+13</sup> <sub>-15</sub>
Blanco 1	132 ± 24 126 <sup>+13</sup> <sub>-14</sub>	(11) (12)	115 <sup>+23</sup> <sub>-15</sub> 200 <sup>+40</sup> <sub>-26</sub>	(23)	4.216 ± 0.003	6.876	237	0.010	(23)	+0.03 ± 0.07	90 ± 25
The Hyades	650 ± 70 678 ± 98	(13) (14)	794 <sup>+161</sup> <sub>-102</sub>	(23)	21.052 ± 0.065	3.389	48	0.001	(23)	+0.13 ± 0.05	661 <sub>-215</sub>
BPMG	< 20 21 ± 4 26 ± 3 25 ± 3 22 ± 6	(15) (16) (17) (18) (19)	12-22	(24)	-	-	9-73	-		-0.01 ± 0.08	20 ± 10
THMG	40 ± 3	(20)	10-40	(24)	-	-	36-71	-		-0.03 ± 0.05	30
32 Ori MG	23 ± 4	(21)	22 <sup>+4</sup> <sub>-3</sub>	(25)	-	-	70-110	0.03 ± 0.01	(28)	-	25.0 ± 2.5

**Notes:** The “Parallaxes” and “DM” values comes from Gaia Collaboration et al. (2018b) with the exception of NGC 1960 that comes from Cantat-Gaudin et al. (2018a). The “d” values come from Gaia Collaboration et al. (2018b) with the exception of BPMG and THMG (Malo et al. 2013); and 32 Ori MG (Bell et al. 2017). We took the “[Fe/H]” values from Netopil et al. (2016), with the exception of NGC 2547 (Randich et al. 2018), and BPMG and THMG (Viana Almeida et al. 2009). We assumed solar abundances for NGC 1960 and the 32 Ori MG because lack metallicity values in the literature. Mermilliod (1981) does not provide age errors, so we estimated them from the log  $t$ .

**References:** (1) Jeffries et al. (2013); (2) Manzi et al. (2008); (3) Randich et al. (2018); (4) Jeffries & Oliveira (2005); (5) Dobbie et al. (2010); (6) Barrado y Navascués et al. (1999a); (7) Barrado y Navascués et al. (2004); (8) Stauffer et al. (1999); (9) Stauffer et al. (1998b); (10) Dahm (2015); (11) Cargile et al. (2010); (12) Juarez et al. (2014); (13) Martín et al. (2018); (14) Lodieu et al. (2018); (15) Song et al. (2002); (16) Binks & Jeffries (2014); (17) Malo et al. (2014b); (18) Messina et al. (2016); (19) Shkolnik et al. (2017); (20) Kraus et al. (2014); (21) Bell et al. (2017); (22) Bossini et al. (2019); (23) Gaia Collaboration et al. (2018b); (24) Malo et al. (2013); (25) Bell et al. (2015); (26) Cantat-Gaudin et al. (2018a); (27) Cargile & James (2010); (28) Bell et al. (2017); (29) Mermilliod (1981); (30) Claria (1982); (31) Panagi & O’dell (1997); (32) Barrado y Navascués et al. (1999b); (33) Torres et al. (2008); (34) Mamajek (2007).

### 3.3. Photometry

We gathered photometric data from the literature. For each association, these came from studies carried out with different telescopes and instruments and, therefore, with heterogeneous uncertainties and different completeness and limiting magnitudes. Additionally, we gathered data from all-sky or wide-area multi-wavelength imaging surveys, with ranges from the ultraviolet to the infrared, using, whenever possible, the Virtual Observatory SED Analyzer (VOSA, Bayo et al. 2008), together with the SIMBAD and VizieR databases. We cross-matched the celestial position of each source with the catalogues provided using a matching radius of 3.0''. The catalogues adopted for the analysis are the following: Tycho-2 (Høg et al. 2000)  $B_T V_T$  bands; 2MASS (Cutri et al. 2003)  $JHK_s$  bands; CMC 14 (Evans et al.

2002)  $r$  band; DENIS (DENIS Consortium 2005)  $iJK_s$  bands; UKIDSS (Lawrence et al. 2007) bands  $ZYJHK_s$ ; APASS DR9 (Henden et al. 2009)  $BV gri$  bands; GALEX (Bianchi & Team 2000)  $FUV NUV$  bands; WISE (Cutri 2013)  $W1 W2 W3 W4$  bands; IPHAS DR2 (Barentsen et al. 2014)  $riHa$  bands; SDSS DR12 (Alam et al. 2015)  $ugriz$  bands; VPHAS DR2 (Drew et al. 2016)  $ugri$  bands; and Pan-STARRS1 (Chambers 2017)  $gp_1 rp_1 ip_1 zp_1 yp_1$  bands. As described in Section 3.2, here we also checked all the images to avoid any misidentification. We show the collected photometric bands in Appendix E.

### 3.4. Evolutionary theoretical models and LDB

To estimate the LDB age, we used the luminosity-age relationships from: (a) Burke et al. (2004), calculated by assuming a solar metallicity of  $Z = 0.0188$  and  $Y = 0.27$ ; and (b) Tognelli et al. (2015) with  $Z = 0.013$  and  $Z = 0.016$ .<sup>6</sup> In both the cases, the LDB has been defined as the model in which lithium is depleted by a factor of 100 from its initial value. Moreover, we took the mass-tracks or the isochrones provided from other works and calculated the LDB bolometric luminosity-age relationships as well as the point where lithium has been depleted by a factor of 100: (c) Burrows et al. (1993 and 1997) calculated it on the basis of solar metallicities (Anders & Grevesse 1989); (d) D'Antona & Mazzitelli (1994) calculated it based on solar metallicities (Anders & Grevesse 1989), using the Canuto & Mazzitelli (1991) convection model and opacities from Alexander et al. (1983); (e) BT-Settl models (Allard et al. 2012) using  $[M/H] = 0.0$  (following Asplund et al. 2009); and (f) Siess et al. (2000) using solar composition  $Z = 0.02$ . These relationships also provide other stellar parameters: mass, radius, surface gravity and effective temperature.

Also, we used isochrone models from Tognelli et al. (2011), and a Zero Age Main Sequence from Stahler & Palla (2005), to identify background, foreground sources or multiple systems in the HRDs.

## 4. Method

We built an HRD to locate the LDB in each stellar association, including only those sources with a moderate signal-to-noise ratio ( $S/N > 20$ ), in the region of the lithium absorption line. The way we derived the bolometric luminosities will be discussed in Section 4.3. According to Kraus et al. (2014), the LDB determined using bolometric luminosities or bolometric magnitudes is more unambiguous due to their large dynamical range over which it varies across the relevant age scales. Thus, we demarcated the LDB in terms of bolometric luminosity.

To estimate subsequent quantities, we first need to estimate the distance of the cluster. To do this, using the member list we evaluated the median distance and size of each open cluster constructing a kernel density estimation<sup>7</sup> (KDE) function, as suggested in Luri et al. (2018). Following this method, we obtained the mode parallax ( $\varpi_{\text{mode}}$ ), the median, the weighted median, the weighted variance, the quartiles, the 2.5th percentile, and the 97.5th percentile. Finally, we calculated distances at different percentiles with  $d = 1/\varpi$ . In Table 2 we provide the estimated parallaxes together with the calculated distances for each stellar association. As an example, Figure 1 shows the parallax probability density function (PDF) for Alpha Persei. Unlike open clusters, the sources belonging to BPMG, THMG, and 32 Ori MG are positioned across a wide range of distances (see Table 1 and Malo et al. 2013). For this reason, we avoided calculating the average value and we used the distance (parallax) available for each source.

<sup>6</sup> In the Tognelli et al. (2015) models,  $[Fe/H] = 0.0$  correspond to  $Z = 0.013$ , and  $[Fe/H] = +0.1$  to  $Z = 0.016$ . We estimated the ages for Alpha Persei and the Hyades using  $Z = 0.016$  and for the rest  $Z = 0.013$ , due to their metallicities, see Table 1.

<sup>7</sup> We used the library `scikit-learn` (Pedregosa et al. 2011) to calculate it.

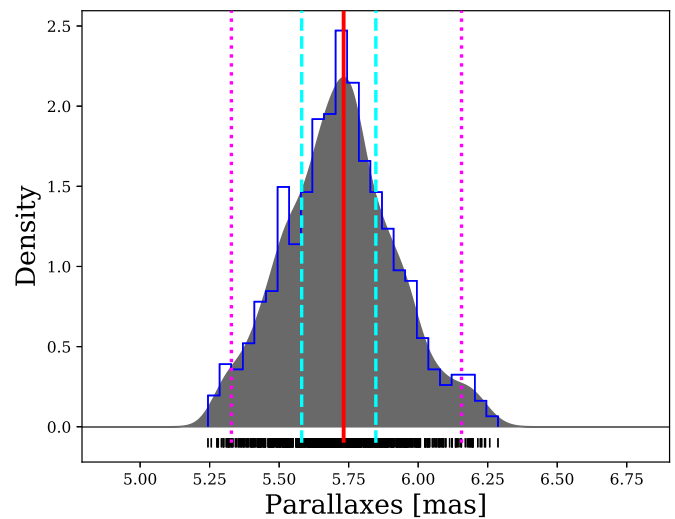


**Fig. 1.** Parallax PDF for the Alpha Persei members (taken from Gaia Collaboration et al. 2018b). The modelled PDF is shown in gray and a superimposed histogram in blue. The two magenta vertical dotted lines point the 2.5th and 97.5th percentiles; the two cyan vertical dashed lines point the quartiles and the red vertical line shows the mode of the PDF. The small vertical black lines below the horizontal axis (below  $y = 0.0$ ) show the parallaxes of each source.

### 4.1. Outliers based on proper motions and parallaxes

The accurate proper motions and parallaxes obtained from *Gaia* DR2 allowed us remove possible outliers in the different LDB samples. As an example, Figure 2 shows the proper motion vector point diagram (VPD) for the Alpha Persei with sources from the LDB sample and the comparison sample. Several sparse sources do not share proper motions with the rest, so we considered them, based on visual inspection, as outliers and were discarded as members. We plotted the proper motions as ellipses because we took into account the uncertainties and the correlation coefficients between them, as recommended in Brown et al. (1997a) (see Lindegren et al. 2016 & 2018, Luri et al. 2018 and examples in Cantat-Gaudin et al. 2018b). Similarly, we compared the parallaxes, see Figure 3 for Alpha Persei. We discarded in the LDB analysis the sources with parallaxes outside the range delimited by the values at the 2.5th and 97.5th percentiles, taking into account the uncertainties of the individual measurements. These values are shown with a grey filled area and the quartiles with a red superimposed area. The lack of radial velocities with enough resolving power for all objects in all associations prevents us from performing a further complete analysis using positions, parallaxes, proper motions, and radial velocities. We proceeded in the same way in all the open clusters. The figures can be found in Appendix A.

### 4.2. Distances from parallaxes

One of the innovations of this work is the inclusion of individual distances for each object. The conversion of  $d = 1/\varpi$  might not be used to assess the distance and to deal with this issue. Previous works (see Maíz Apellániz 2005, Bailer-Jones 2015 and Luri et al. 2018) suggested that we derive distances as an inference problem using a Bayesian approach. Thus, we inferred the distance of each source individually, drawn from the parallax using the *Kalkayotl* code (Olivares et al. 2020) after 10 000 iterations. We tested all prior families (see Olivares et al. 2020) and

**Table 2.** Parallax distributions from the initial sample of cluster members using a KDE based on *Gaia* DR2 data.

Stellar association	$\varpi_{\text{mode}}$ [mas]	$\varpi_{\text{KDE}}$ [mas]				$d_{\text{mode}}$ [pc]	$d_{\text{KDE}}$ [pc]		
		2.5th	25th	75th	97.5th		2.5th	25th	75th
Alpha Persei	5.73192	5.32825	5.58102	5.84774	6.15589	174.461	187.678	179.178	171.006
NGC 1960	0.82873	0.65783	0.77649	0.87735	0.99241	1 206.665	1 520.149	1 287.846	1 139.795
IC 4665	2.88239	2.34501	2.72233	2.99779	3.28228	346.934	426.437	367.332	333.579
NGC 2547	2.52757	1.98269	2.40987	2.61619	2.89936	397.379	504.365	414.960	382.235
IC 2602	6.57185	6.11623	6.42974	6.70321	7.08069	152.164	163.499	155.527	149.182
IC 2391	6.59159	6.14352	6.44991	6.71406	7.11775	151.708	162.773	155.040	148.941
The Pleiades	7.35915	6.77853	7.18755	7.51509	8.02017	135.885	147.524	139.129	133.065
Blanco 1	4.17949	3.98254	4.13539	4.30490	4.47278	239.264	251.096	241.815	232.293
The Hyades	21.08226	16.44997	19.67124	22.48718	27.34499	47.433	60.790	50.835	44.469
32 Ori MG	9.62252 <sup>a</sup>	8.30029	8.97758	10.19470	10.76314	103.922 <sup>b</sup>	120.477	111.388	98.090

<sup>a</sup> This value is not the  $\varpi_{\text{mode}}$  it is the 50th percentile of the parallax PDF,  $\varpi_{\text{KDE}}$ .

<sup>b</sup> The value is calculated using the value marked as <sup>a</sup>.

found that the Gaussian prior proves to be the one most suited to describe the parallax distribution. The Gaussian prior is defined by two parameters: the `prior_loc` and the `prior_scale`. The `prior_loc` is the open cluster distance value taken from Gaia Collaboration et al. (2018b) or Cantat-Gaudin et al. (2018a) and the `prior_scale` is five times the maximum radius of the open cluster (Olivares et al. 2020).

We assumed the same prior for all objects belonging to the same stellar association. For each open cluster, we calculated the maximum radius using the comparison lists, comparing their sky-positions with the sky-position of the centre derived from Gaia Collaboration et al. (2018b) (private communication F. van Leeuwen). On the other hand, in the MGs, the members are distributed in a wide range of distances without being grouped or ‘clustered’ in a particular area of the sky. For instance, BPMG members are located between 9–73 pc, THMG members between 36–71 pc (see Malo et al. 2013) and 32 Ori MG members between 71–131 pc (see Bell et al. 2017). We chose the median value of the distance for the `prior_loc`, and a `prior_scale` of 200 (roughly two times the larger distance). In Table E.1 we show the priors used in the calculations.

We obtained a distance distribution for each source where the maximum-a-posteriori describes the distance of the object ( $d_{MAP}$ ), and the two values at the 2.5th and 97.5th percentiles determine its minimum and maximum distances ( $d_{min}$  and  $d_{max}$ ).

For those objects without parallaxes or with negative values, we assumed the distribution corresponding to the association they belong. The parallax is the mode of the PDF,  $\varpi_{\text{mode}}$ , and the uncertainties are the values at the 2.5th and the 97.5th percentiles. We calculated the distances and the uncertainties by taking the reciprocal of the parallax values. Regarding 32 Ori MG, we proceeded differently. We took all the members from Bell et al. (2017) and calculated the parallax PDF. In this way, we realized that several sources are outliers, and we considered a sub-sample of objects with parallaxes in the range of  $\varpi \in (8.0, 11.0)$  mas. We used this sub-sample to derive the 32 Ori MG distance. We did not apply this procedure to BPMG and THMG due to the wide range of parallaxes of their members.

Other works, such as that of Lodieu et al. (2019b), determine parallaxes for the faintest Hyades objects. We computed distances from these parallaxes in the same way as before, by using the same prior (see Table E.1). Table 2 lists the values of the parallaxes (mode, KDE), the percentiles, and the derived distance with its uncertainties for each analysed stellar association.

#### 4.3. Bolometric luminosities and effective temperatures

The bolometric luminosity and effective temperatures were evaluated reconstructing the spectral energy distribution (SED) of each analysed source. To do this, we relied on the several photometric bands in order to have a complete coverage of the stellar spectra in a broad range of wavelengths. We used the data of the photometric surveys listed in Section 3.3.

The SED was built using the VOSA tool (Bayo et al. 2008). In a first step, VOSA brings together all the photometric values of each source and transforms the magnitudes into fluxes. The total observed flux is computed adding all the photometric bands. When measurements of overlapping bands are taken, VOSA estimates the overlapping wavelength regions and weights the fluxes accordingly to avoid overestimating the total flux. In addition, each photometric value is de-reddened taking into account the values of  $A_V$ <sup>8</sup> and the extinction law from Indebetouw et al. (2005). Secondly, VOSA compares the flux values with synthetic photometry from several grids of theoretical spectra, using a  $\chi^2$  test and determines which model reproduces the observed data. Thirdly, the best-fitting model infers the flux in the wavelength range where there are no data, calculates the final total flux for the source ( $F_{\text{tot}}$ ), its uncertainty ( $F_{\text{err}}$ ), and its stellar parameters with their respective uncertainties. Blue and infrared excesses are not taken into account, and the analysis does not include UV or  $u$  bands.

We used two sets of theoretical models to fit the SEDs: Kurucz (Castelli et al. 1997) and BT-Settl (Allard et al. 2013) grids. Both grids and the range of validity of each one have been studied before (see Bouy et al. 2015, Barrado et al. 2016, Bayo et al. 2017, and Solano et al. 2019 and 2021). We restricted the parameters to:  $T_{\text{eff}} \geq 4\,500$  K for Kurucz models and  $T_{\text{eff}} \leq 4\,500$  K for BT-Settl, where they work best. We fixed the metallicity to the value of each association, see Table 1, and the surface gravity to the fair value of  $\log g = 4.5$  dex, except for the Hyades members where we assumed  $\log g = 5.0$  dex. This assumption is in line with the BT-Settl evolutionary models (Allard et al. 2012): very low-mass stars with masses from 0.006 to  $1.4 M_{\odot}$  and ages between 10 Ma to 1 Ga, have  $\log g \in [4.4, 5.3]$  dex. From an empirical point of view, Reid & Hawley (2005) pointed out that the values for M0–M5 spectral types are ranged  $\log g \in [4.5, 5.0]$  dex. Based on our previous experience with VOSA, we fixed these values to explore the effective temperature range

<sup>8</sup> The  $A_V$  were calculated from  $E(B-V)$  with  $R_V = 3.1$ .

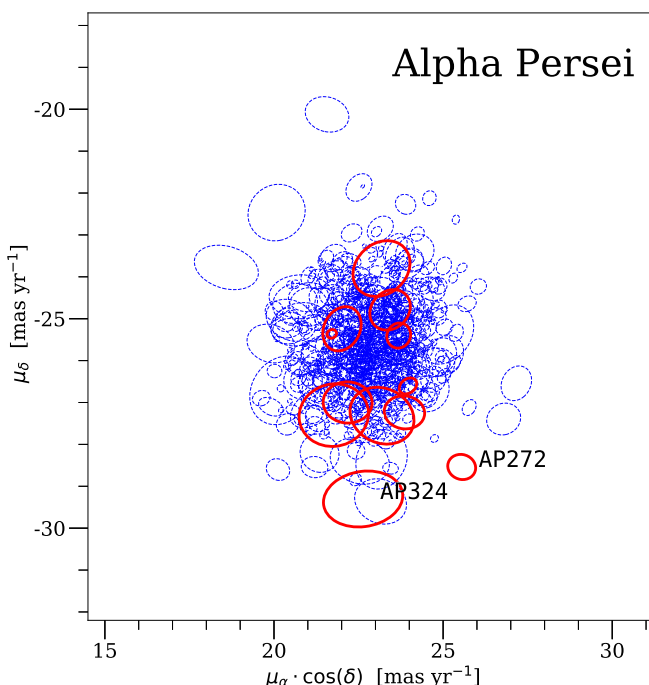
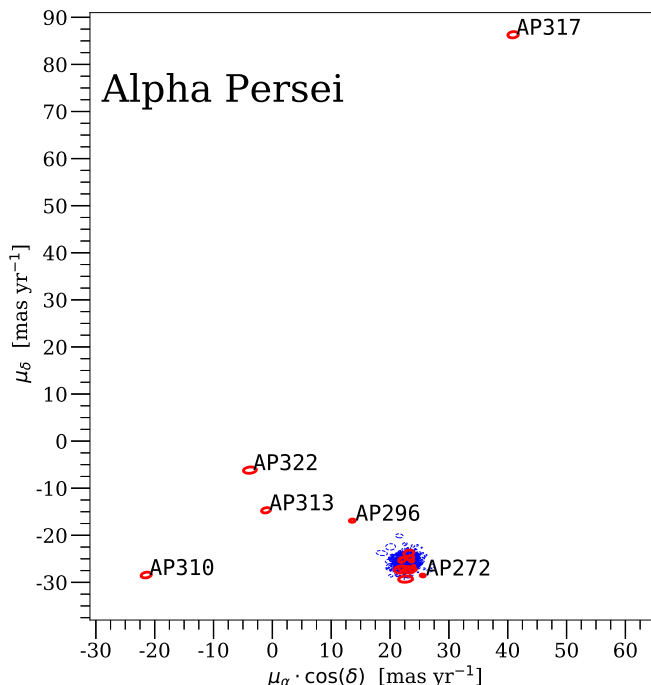


**Fig. 2.** VPD for Alpha Persei. **Top:** Blue dashed ellipses are the members taken from Gaia Collaboration et al. 2018b; red ones are the LDB sample objects. Five sources (AP296, AP310, AP313, AP317, and AP322) possess a proper motion different from that of the rest of the members. AP272 is also shown (see the text). Uncertainties in the proper motions and its correlations are taken into account and shown as ellipses. All data have been taken from the *Gaia* DR2 catalogue. **Bottom:** Zoom on the previous plot.

more effectively<sup>9</sup>. A large number of photometric bands, as well

<sup>9</sup> Information related to VOSA quality tests and caveats are in Cifuentes et al. (2020), and in the VOSA Help and Documentation: <http://svo2.cab.inta-csic.es/svo/theory/vosa50/helpw4.php?otype=star&action=help&what=fit#fit:bollum>.

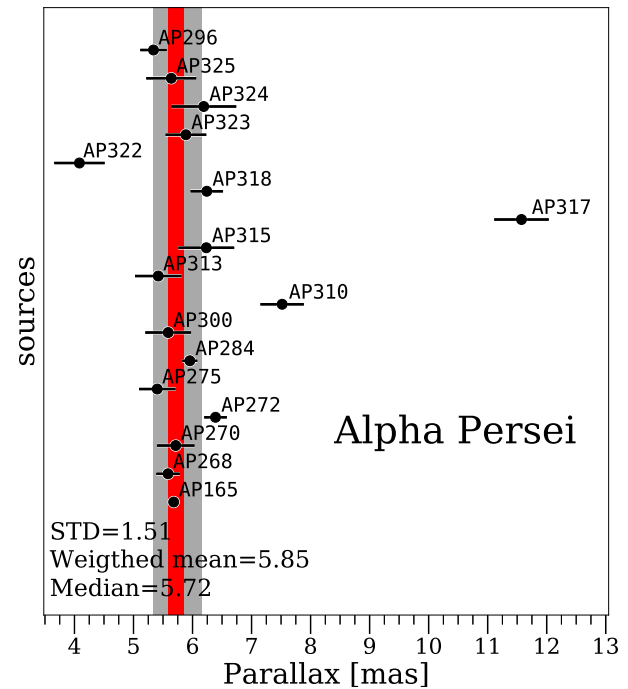


**Fig. 3.** Parallaxes for 17 selected Alpha Persei sources close to the LDB. The grey filled area shows the parallax distribution from Gaia Collaboration et al. (2018b) between the percentiles 2.5th and 97.5th, while the distribution quartiles are delimited by a red filled area superimposed. All the parallaxes have been taken from the *Gaia* DR2 catalogue. The standard deviation (STD), the weighted mean, and the median of the LDB sample are also displayed.

as the wide spectral range they cover, allows us to say that the vast majority of the  $F_{\text{tot}}$  from the object comes from observations ( $\geq 70\%$ ) and not from any model. We checked all the SEDs to detect and avoid spurious photometric bands, false detections, or contamination due to background sources. We fitted a cubic spline over the five best models, minimizing the  $\chi^2$  in order to avoid the discrete values in  $T_{\text{eff}}$  returned by VOSA (Barrado et al. 2016). The analysis of the uncertainties on our calculated bolometric luminosities and effective temperatures, as well as the assumed values for metallicity, surface gravity, and reddening, are discussed in Section 6.

We calculated bolometric luminosities using  $L_{\text{bol}} = 4\pi d^2 F_{\text{tot}}$ , where  $F_{\text{tot}}$  is the total observed flux obtained from VOSA, and  $d$  is the distance of the object. In the case of sources with parallaxes, we calculated bolometric luminosities generating a Gaussian random sample of  $F_{\text{tot}}$  considering its uncertainty  $F_{\text{err}}$ , and using its distance distribution as we mentioned in Section 4.2. The maximum-a-posteriori of this distribution is the  $L_{\text{bol}}$  and the 2.5th and 97.5th percentiles determine its uncertainties.

#### 4.4. LDB loci determination

Previous works (Jeffries & Oliveira 2005, Juarez et al. 2014 or Binks & Jeffries 2014) have defined the LDB loci in the HRD, ( $(T_{\text{eff,LDB}}, L_{\text{bol,LDB}})$ ) as the mid-point between the coldest lithium-poor source and the hottest lithium-rich one (in terms of effective

[http://svo2.cab.inta-csic.es/svo/theory/vosa50/helpw4.php?otype=star&action=help&what=qua\\_libraries](http://svo2.cab.inta-csic.es/svo/theory/vosa50/helpw4.php?otype=star&action=help&what=qua_libraries).

temperature) and the faintest lithium-poor source and the brightest lithium-rich one (in terms of bolometric luminosity).

Using the LDB samples defined previously, we discarded all the non-members (NM) using the *Gaia* data and confirmed multiple systems (hereafter CMS, such as spectroscopic binaries) that contribute to blur the LDB for this analysis. We took the faintest lithium-poor object and considered all the sources whose bolometric luminosities were in the interval between  $L_{\text{bol}}$  97.5th and  $L_{\text{bol}}$  2.5th. Likewise, we did the same for the brightest lithium-rich object. Some objects can be considered as multiple systems because of their location in the HRD or analogous diagrams. However, there is no explicit confirmation of whether they are<sup>10</sup>. In this case, we have performed the LDB analysis considering both cases: (a) assuming it is a single star, (b) or it is a multiple system and was excluded in the determination of the LDB.

Applying this procedure, we obtain (for any stellar association) a sample of  $n$ -sources close to the LDB locus. In some cases (IC 2602, Blanco 1), we can select only two sources, a lithium-poor and a lithium-rich one, and this is insufficient for the analysis. We would require at least two lithium-poor sources and two lithium-rich ones. Thus, the resulting sub-samples should have at least four sources.

To estimate the LDB and quantify the uncertainty associated, we used a jackknife method with a bootstrap re-sampling. We split the sub-sample of  $n$  sources into  $n$  sets containing all but one source: the first set contains all but source 1, the second set contains all but source 2, and so forth. For each set, we generated 10 000 simulated bootstrap samples. A bootstrap sample contains  $n - 1$  bolometric luminosities, one from each source. They were generated using a Gaussian random value of the  $F_{\text{tot}}$  considering its uncertainty  $\Delta F_{\text{tot}}$ , and a random value of the distance derived from its distribution (Section 4.2).

We calculated the LDB luminosity as the equal middle point between the bolometric luminosity of the faintest lithium-poor object and the brightest lithium-rich object. The result is a bolometric luminosity distribution of the LDB loci obtained from all the simulations, where the LDB is located at the mode, and the uncertainties are given at 16th and 84th percentiles, as we show in Figure 4. Finally, we derived ages using the evolutionary models presented in Section 3.4. Also, we determined the  $T_{\text{eff}} \text{ LDB}$  as the mid-point in terms of effective temperature between the coldest lithium-poor source and the hottest lithium-rich one. We estimated an uncertainty due to the models of  $\pm 71$  K based on the mean squared error of the two sources. As an example, we show in Fig. 5 the HRD for Alpha Persei with the LDB sample, the comparison sample, and our estimated  $L_{\text{bol LDB}}$ . Similar figures for the remaining stellar associations are shown in Appendix A.

## 5. Analysis of the LDB

In the following subsections, we analyse in detail each stellar association and locate its LDB. We apply the method presented in Section 4. The results are summarised in Table 3 and Figure 9.

### 5.1. Alpha Persei

We collected sources from former works around the LDB (with  $K_s > 12.0$  mag). In total, our compilation includes 17 sources: nine without lithium and six with it, from Stauffer et al. (1999)

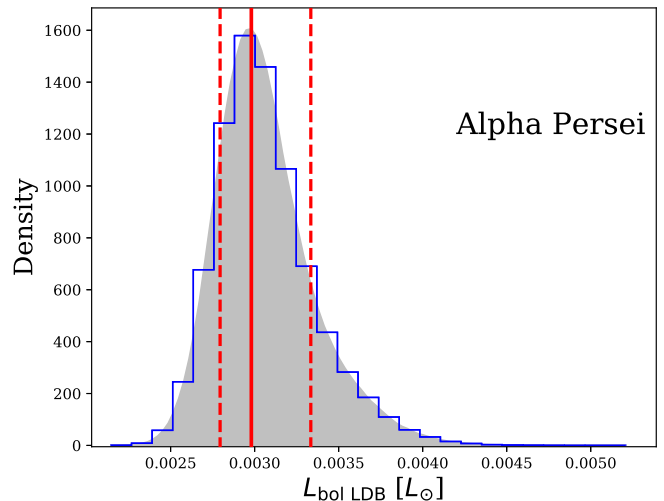


**Fig. 4.** Bolometric luminosity PDF for the Alpha Persei LDB, after run 60 000 bootstrap samples, see Section 4.4. We show all the sample distribution as a blue histogram, and we model a PDF with all the values in grey. We highlight the mode of the PDF with a red line and the percentiles at 16th and 84th with two red dashed ones.

(first work with a complete census of members around the LDB); one with lithium, AP270, from Basri & Martín (1999a) and one without lithium, AP272, from Zapatero Osorio et al. (1996).

Photometric data from previous works were used:  $R_c I_c K_s$  (Stauffer et al. 1999 and Barrado y Navascués et al. 2002), and  $F814W$  and  $F785L$  from the *Hubble Space Telescope* (Martín et al. 2003). In addition, we recovered  $VI_c$  from Prosser (1992 and 1994), and  $R_c I_c$  from Deacon & Hambly (2004). All the sources have parallaxes and proper motions in *Gaia* DR2.

Stauffer et al. (1999) included remarks about some sources: AP317 could be a background star or a possible member; AP322 (2MASSJ 03330848+4937550) is likely to be a non-member; and AP323 and AP325 could be binary systems.

The proper motions (Fig. 2) and parallaxes (Fig. 3) suggest that AP310 at 7.518 mas and AP317 at 11.573 mas, are foreground objects that do not belong to Alpha Persei, whereas we confirmed that AP322 is a background source with  $\varpi = 4.083 \pm 0.426$  mas. AP272 looks like a foreground object, 6.389 mas, but its proper motion could agree with the rest of the members. Its position on the HRD does not affect the LDB locus. AP313 shows a discrepant proper motion but a parallax (5.419 mas) consistent with the members from the comparison sample, so we considered it as a non-member. Lastly, Stauffer et al. (1999) surmised that AP325 was a binary system, and we considered it as a suspected multiple system due to its HRD location (Fig. 5).

Stauffer et al. (1999) located the LDB with the sources AP323 (lithium-rich but probably a binary system), AP310 (lithium-poor) and AP300 (lithium-rich), and they estimated a  $M_{\text{bol LDB}} = 11.40$  mag ( $L_{\text{bol LDB}} = 2.168 \cdot 10^{-3} L_\odot$ ). However, Barrado y Navascués et al. (2004) assume that the LDB is defined by AP310, AP322, and AP300 and located the LDB at  $M_{\text{bol LDB}} = 11.31$  mag ( $L_{\text{bol LDB}} = 2.355 \cdot 10^{-3} L_\odot$ ). With the new analysis, we located the LDB at  $L_{\text{bol LDB}} = 2.98_{-0.19}^{+0.35} \cdot 10^{-3} L_\odot$ , and  $T_{\text{eff LDB}} = 2857 \pm 71$  K (see the HRD in Fig. 5).

Although we considered AP323 and AP325 as suspected binaries, they may play a vital role in the LDB loci, therefore it would be necessary to study their multiplicity more reliably.

<sup>10</sup> Throughout this work, we call these objects suspected multiple systems.

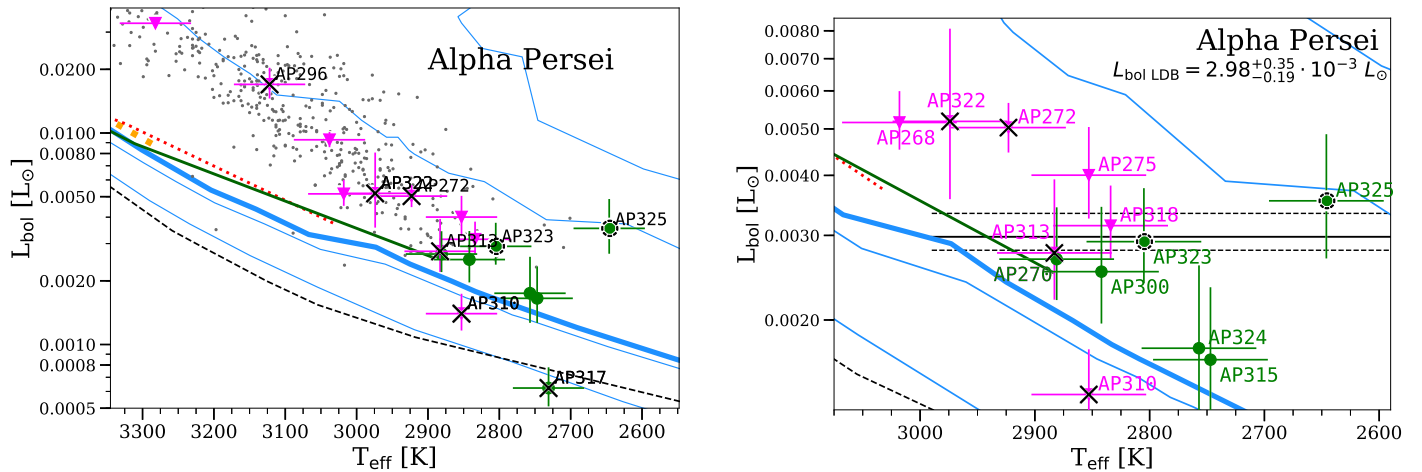


**Fig. 5.** HRD and the LDB for Alpha Persei. **Left:** Symbols are as follows: green solid circles are lithium-rich sources and magenta triangles lithium-poor ones, both from our LDB sample; empty large broken black circles are suspected multiple systems; over-imposed big black crosses are sources discarded as members after this work; and grey points are known members from Gaia Collaboration et al. (2018b). Thin blue lines correspond to isochrones of 1, 10, 100 Ma, and 1 Ga from the BT-Settl models (Allard et al. 2013), while the thick blue one to 80 Ma. The figure also includes 70 Ma isochrones from: D'Antona & Mazzitelli 1994 (black dashed line), Tognelli et al. 2011 (orange dashed dot line), Siess et al. 2000 (red dotted line), and a Zero Age Main Sequence from Stahler & Palla 2005 (the green solid line). **Right:** Zoom on the left plot. A black horizontal line marks the  $L_{\text{bol}}^{\text{LDB}}$ , together with the 16th and 84th percentiles (dotted lines). Alpha Persei is  $79.0^{+1.5}_{-2.3}$  Ma old using the BT-Settl bolometric luminosity-age relationship (Allard et al. 2012). For clarity, members from Gaia Collaboration et al. (2018b) are not shown.

## 5.2. NGC 1960 (M 36)

We created the LDB sample collecting 32 members from Jeffries et al. (2013). We used *gri* photometric data from Jeffries et al. (2013), and from our database (Galindo-Guil et al. in prep.). The source 4165 is the only one without a counterpart in *Gaia* DR2. Candidate members identified as 3028, 3590, and 3596 have counterparts, but lack parallaxes and proper motions, and the source 3081 possesses negative parallax. Jeffries et al. (2013) point out that 3080 shows evidence of being a binary system, and 3081 (the brightest object with lithium) could have depleted the  $\sim 99\%$  of its initial lithium content.

From the VPD (Fig. A.1 left), we considered as non-members 2188, 2249, 2663, 3080, and 3150. Other sources, namely, 1859, 1871, 2696, and 3073, are inside the bulk of the confirmed members by the narrowest of margins. We discarded 1269, 1859 and 2703 in the location of the LDB, because lie outside the percentiles of the parallax PDF (see Fig. A.1 right). We note that 2171 is almost outside the percentiles of the parallax PDF, and 3612 possesses a large parallax uncertainty; 3081 has negative parallax, and the bolometric luminosity was calculated based on the distance derived from the comparison sample.

We note that the abrupt transition between lithium-poor and lithium-rich objects is not visible in NGC 1960, (see the HRD in Fig. A.2a), and compared with other stellar associations (see Sects. 2.3, 2.4 and subsequent sections). Jeffries et al. (2013) locate the LDB with three lithium-rich objects: 3080, 3081, and 3596 at  $L_{\text{bol}}^{\text{LDB}} = 31.6^{+6.4}_{-5.3} \cdot 10^{-3} L_{\odot}$ . However the combination of undetected binary systems, photometric uncertainties and contamination, prevented them to detect a reliable LDB loci. Two out of the three lithium-rich sources, 3596 and 3081, do not have individual parallaxes in *Gaia* DR2, so we assumed the mean distance to the cluster (see Table 2), and we considered 3080 as a non-member because of its proper motion.

The scarcity of lithium-rich sources and the poor astrometric quality of the data (due to the faintness of the sources) did not allow us to derive a bona fide LDB age. In any case, we proceeded

in the same way as we did with Alpha Persei. We located the LDB at  $L_{\text{bol}}^{\text{LDB}} = 23.6^{+12}_{-4.9} \cdot 10^{-3} L_{\odot}$ , and  $T_{\text{eff}}^{\text{LDB}} = 3123 \pm 71$  K, see Fig. A.2a. However, if we consider the three lithium-rich objects (3080, 3081 and 3596) as multiple systems and discard them, then the faintest lithium-poor source, 4165, gives an upper limit in the LDB location at  $L_{\text{bol}}^{\text{LDB}} < 16.27 \cdot 10^{-3} L_{\odot}$  and at  $T_{\text{eff}}^{\text{LDB}} < 3016$  K (see Fig. A.2b). This object would push the minimum age to  $37.4^{+8.3}_{-8.1}$  Ma. (see Fig. A.2b).

NGC 1960 needs a deeper photometric survey followed by a spectroscopic study to determine lithium abundances in fainter objects than our LDB sample. This is because the abrupt transition between lithium-poor and lithium-rich objects is not visible in contrast to other associations. Our LDB loci might be a tentative one, and we do not discard the possibility that it could be a possible upper limit.

## 5.3. IC 4665

We recovered data from different works: 39 members from Manzi et al. (2008), 13 members from Prosser (1993) and Jeffries et al. (2009) and 15 members only from Jeffries et al. (2009). All sources from Manzi et al. (2008) and some from Jeffries et al. (2009) have been detected previously in Prosser (1993), Giampapa et al. (1998) and de Wit et al. (2006). Manzi et al. (2008) did not provide equivalent widths of lithium for their faintest members, they highlighted the presence or absence of lithium and classified them in three categories: 'Y' for a lithium-rich source, 'N' for a lithium-poor one, and '?' when the signal-to-noise ratio did not allow to confirm or reject the presence of lithium. Our LDB sample comprises a total of 67 sources and all of them have counterparts in *Gaia* DR2. P333 (with lithium) and P373 (without lithium) lack parallax and proper motion measurements. In addition, we collected photometric data in filters  $I_{\text{CFHT12}}$  and  $z_{\text{CFHT12}}$  (de Wit et al. 2006) and  $VI_c$  (Jeffries et al. 2009).

The proper motions are illustrated in Figure A.3 and parallaxes in Figure A.4. In terms of proper motions, we rejected: JCO1-530, JCO3-285, JCO3-357, JCO4-337, JCO9-120, P002, P030, P059, P065, P139 P215, P290, P331, P377, P398, and P411. Some objects lie outside the percentiles of the parallax PDF. Then, A.09.30.47, JCO4-337, P396, and P398 were considered foreground objects, while JCO1-530, JCO2-213, JCO3-285, P002, P059, P065, P139, P215, P290, P331, and P377 were taken as background sources; P344 is on the borderline of the bulk of the proper motions but we still considered it as a member.

P065, P290, P313, and P315 show variable radial velocities or evidence for a double line system, or both (Manzi et al. 2008); consequently, we considered them as multiple systems. We note that P344, as in the case of P313, could be a multiple system because both share close positions in the HRD (see Figure A.5) and have similar parallax values, so it is considered a suspected multiple system. A.09.30.14 and P238 are marked as ‘?’ in Manzi et al. (2008) and their lithium detection is uncertain. Then, P372 and P344 are marked as ‘Y?’ (Manzi et al. 2008) and we treated them as lithium-rich objects.

Manzi et al. (2008) locate the LDB between the sources P350 (lithium-poor) and P338 (lithium-rich) at  $L_{\text{bol LDB}} = 24.9_{-8.1}^{+11.1} \cdot 10^{-3} L_{\odot}$ . We located the LDB by considering two different scenarios. In the first one, we considered P344 as a single source (Fig.A.5c), while the second scenario, we considered P344 as a suspected multiple system (Fig. A.5d). In the first scenario, we located the LDB at  $L_{\text{bol LDB}} = 25.8_{-1.9}^{+3.3} \cdot 10^{-3} L_{\odot}$  and  $T_{\text{eff LDB}} = 3110 \pm 71$  K, while the second scenario resulted in  $L_{\text{bol LDB}} = 23.6_{-1.6}^{+2.1} \cdot 10^{-3} L_{\odot}$  and with equal  $T_{\text{eff LDB}}$ . For this open cluster, we decided to apply this second scenario.

We remark that the four objects, A.09.30.14, P238 P372, and P344, located around the LDB, must be studied in detail with high-quality spectra to determine their lithium abundances. Also, it would be interesting to have parallaxes for P333 (with lithium) and P373 (without lithium).

#### 5.4. NGC 2547

We took the sample of 52 radial velocity members from Jeffries & Oliveira (2005) as our LDB sample. We collected photometric data in  $BVI_c$  filters from Naylor et al. (2002),  $R_cI_cZ$  from Jeffries et al. (2004) and the *Spitzer* photometric bands  $3.6\mu\text{m}$ ,  $4.5\mu\text{m}$ ,  $5.8\mu\text{m}$ ,  $8.0\mu\text{m}$ , and  $24\mu\text{m}$  from Gorlova et al. (2007). All the sources have counterparts in *Gaia* DR2 with parallax and proper motion measurements.

Jeffries & Oliveira (2005) identified six possible multiple systems: JO-21, JO-27, JO-30, JO-31, JO-39, and JO-56. In addition, three of them, (JO-27, JO-30, and JO-31) together with JO-26, are lithium-rich objects located at brighter luminosities than the LDB (see Figures 5, 6, and 7 from Jeffries & Oliveira 2005). So, JO-26 could be an unresolved multiple system, and it was excluded from our calculation.

The analysis of the proper motions and the parallax distribution (see Figure A.6) allowed us to affirm that JO-26 and JO-30 are non-members; JO-27 and JO-31 could be multiple systems or fast rotators. We note that JO-62 has a very high uncertainty in proper motions; and JO-02, JO-07, JO-37, JO-45, and JO-57 are near the borders of the bulk of previous members. Overall, the objects that we considered as non-members based on proper motions are JO-26 and JO-30; those based on parallaxes:- JO-45, JO-57, and again JO-30.

Jeffries & Oliveira (2005) located the LDB at  $L_{\text{bol LDB}} = 11.59_{-1.84}^{+1.59} \cdot 10^{-3} L_{\odot}$ . We located the LDB at  $L_{\text{bol LDB}} = 11.13_{-0.89}^{+2.4} \cdot 10^{-3} L_{\odot}$  and  $T_{\text{eff LDB}} = 3004 \pm 71$  K (see Figure A.7).

#### 5.5. IC 2602

We selected 14 sources from Dobbie et al. (2010). Six of them are lithium-rich objects and six are lithium-poor. Dobbie et al. (2010) considered two objects: 10420419-6404236 and 10443357-6415455 as possible members, and the rest as bona fide members. From Dobbie et al. (2010), we have recovered photometric data in the band  $I_c/I_{\text{WPESO845}}$ . However, we did not use them in our SED fitting, given the large uncertainties in their photometric values, as the authors pointed out. All the sources have a counterpart in *Gaia* DR2, but 10452984-6444543 lacks parallax and proper motions.

10443357-6415455 is considered as possible member by Dobbie et al. (2010) and we confirmed that it is a background object due to its parallax (see Fig. A.8 right). Then, 10370251-6444416 can also be considered as a background object. Besides, Dobbie et al. (2010), suggest that two sources could be binary systems or young interlopers due to their positions above the cluster sequence in the colour-magnitude diagram, and with clear lithium detections: 10452984-6444543 and 10391188-6456046. The position of 10391188-6456046 in the HRD (Fig. A.9) indicates that it may be an equal-mass binary system. 10452984-6444543 is detected in *Gaia* DR2 but without astrometric solution, for this reason and taking into account its HRD position, we suggest that it is a suspected multiple system. We note that *Gaia* DR2 has revealed that this source has a fainter background counterpart, 5239800972309874176, located at  $1.8''$ , with a parallax of  $0.6386 \pm 0.5577$  mas. The fact that it is only identified in *Gaia* DR2 suggests that the photometric data released in previous surveys are a combination of two sources. Finally, 10452984 and 10391188 are two suspected binaries that need solid confirmation about their multiplicity. Dobbie et al. (2010) located the LDB between 10430890-6356228 and 10430236-6402132, at  $M_J = 8.26 \pm 0.23$  mag ( $L_{\text{bol LDB}} = 6.2_{-1.2}^{+1.5} L_{\odot}$ ). We located the LDB at  $L_{\text{bol LDB}} = 7.14_{-0.57}^{+1.2} \cdot 10^{-3} L_{\odot}$  and  $T_{\text{eff LDB}} = 2926 \pm 71$  K.

#### 5.6. IC 2391

We collected a total of 28 sources from our previous works (Barrado y Navascués et al. 1999a, 2001, and 2004 and Boudreault & Bailer-Jones (2009)). We added some objects to the LDB sample: CTIO-106, CTIO-202, and CTIO-205, which are members but lack lithium feature measurements because the low-quality spectra do not allow us to discern the presence or absence of it (Barrado y Navascués et al. 2004). We used our photometric data  $VR_cI_cZ$  from Barrado y Navascués et al. (2001) and we collected  $VR_cI_c$  from Patten & Pavlovsky (1999). All the sources have a counterpart with proper motions and parallaxes in *Gaia* DR2. Our membership criterion is in contrast to that of Boudreault & Bailer-Jones (2009), who considered as members objects without the H $\alpha$  line in emission: 20-001, 20-009, 20-024, and 20-029. Below, we will see that these sources can be considered outliers due to their parallax, proper motions, or both. Furthermore, they suggest that values of EW Li < 0.1 Å, as it happens with 20-009 and 20-014 (see their Table 6), indicate the presence of the lithium feature at 6708 Å. However they do not provide a

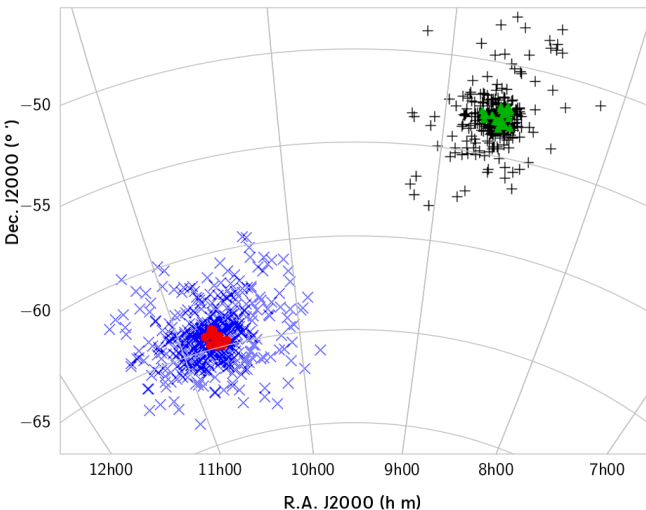


**Fig. 6.** Projected positions for IC 2391 (black pluses are members from Gaia Collaboration et al. 2018b and green triangles objects from the LDB sample) and IC 2602 (blue crosses are members from Gaia Collaboration et al. 2018b and red circles sources from the LDB sample).

reliable measurement of the equivalent width. In the same way, we go on to see that these sources are outliers.

From Barrado y Navascués et al., 1999a, and 2004, we collected some remarks about some objects: PP-07 and CTIO-206 could be possible binaries or outliers; CTIO-062 is a lithium-rich source (also studied in Boudreault & Bailer-Jones 2009 with name 20-022); the lithium detection of CTIO-077 is quite uncertain (Barrado y Navascués et al. 2004), but we considered it as a lithium-rich object.

We confirmed two foreground objects: PP-07 and 20-024, along with eight background sources: CTIO-017, CTIO-059, 20-001, 20-009, 20-012, 20-014, 20-018, and 20-029 (see Figure A.10 right). We show the proper motions from IC 2602 and IC 2391 LDB samples in the same VPD, Figure A.10 left. There are ten sources that we considered as non-members because they are far away from the bulk of the members: 20-001, 20-009, 20-012, 20-014, 20-018, 20-024, 20-029, CTIO-017, CTIO-0 59, and PP-07; these are the same objects that are not members in terms of parallaxes. We note that there is a crowded region in the VPD around  $\mu_\alpha \cdot \cos(\delta) = -12.9$  and  $\mu_\delta = 11.5 \text{ mas yr}^{-1}$ , with six sources: PP-07, CTIO-017, 20-001, 20-017, 20-018, and 20-029.

In addition, CTIO-062 (20-022), a lithium-rich member (Barrado y Navascués et al. 2004 and Boudreault & Bailer-Jones 2009), has proper motions and parallax similar to other members, as well as H $\alpha$  in emission, but it is located below the cluster sequence in the HRD. It shows a fainter bolometric luminosity than other members with the same effective temperature, so it could be an outlier. The objects without measurements of the lithium feature (CTIO-106, CTIO-202, CTIO-205, and 15-005) are not relevant in the LDB determination, except for CTIO-205 that could be a multiple system due to its position in the HRD. CTIO-081 could also be a multiple system (see the HRD, Figure A.11). According to Boudreault & Bailer-Jones (2009), the lithium-poor M7.5 dwarf 15-005 fulfills our membership criteria, but due to its position in the HRD and its spectral type, it would be expected to have lithium. The reason for the non-detection is the low signal-to-noise ratio of the spectrum ( $S/N = 8.3$ ). We considered this object a member with doubtful detection, although it does not affect the LDB location. Lastly, CTIO-077, a member with an uncertain lithium detection (Barrado y Navas-

cués et al. 2004), considered as a lithium-rich object, is not key in the determination of LDB loci.

Barrado y Navascués et al. (1999a) located the LDB between the sources PP-14, CTIO-096, and CTIO-038 at  $M_{\text{bol LDB}} = 10.29$  mag ( $L_{\text{bol LDB}} = 6.026 \cdot 10^{-3} L_\odot$ ). Subsequently, Barrado y Navascués et al. (2004) located the LDB at  $M_{\text{bol LDB}} = 10.24$  mag ( $L_{\text{bol LDB}} = 6.31 \cdot 10^{-3} L_\odot$ ). We located the LDB at  $L_{\text{bol LDB}} = 5.93^{+0.23}_{-0.13} \cdot 10^{-3} L_\odot$  and  $T_{\text{eff LDB}} = 2956 \pm 71 \text{ K}$ .

### 5.7. The Pleiades

We selected 35 sources from different works: Marcy et al. (1994), Rebolo et al. (1996), Oppenheimer et al. (1997), Stauffer et al. (1998b and 1998a), and Dahm (2015), together with photometry and lithium quantities from the DANCe database (Bouy et al. 2015 and Barrado et al. 2016 and other works: Steele et al. (1993), Bouvier et al. (1998), Zapatero Osorio et al. (1999), Martín et al. (2000), and Stauffer et al. (2007)). With the exception of Roque 5 and Roque 25, the rest of the sources have a counterpart in the *Gaia* DR2 catalogue; and with the exception of CFHT-Pl-18 and MHObd 3, all the sources have parallaxes and proper motions<sup>11</sup>.

Olivares et al. (2018) studied the probability of a source being an equal-mass binary and eight sources fulfil their criterion: HCG 509, HHJ 6, HHJ 3, PPL-15, PPL-15, Roque 13, MHObd 3, CFHT-Pl-12, and CFHT-Pl-16. Some of these sources are confirmed binary systems: CFHT-Pl-12 (Bouy et al. 2006), CFHT-Pl-18 (Martín et al. 1998), PPL-15 (Basri & Martín 1999b), and HCG 509 (Stauffer et al. 2020). Others are possible suspected binaries: PPL-1 with a strong absorption lithium feature, HHJ-6 and BPL-169 (Stauffer et al. 1998b), and Roque 12 (which might be an eclipsing binary brown dwarf as suggested by Scholz et al. 2020, based on a single eclipse).

Martín et al. (2000) claimed that the lithium-rich source CFHT-Pl-16 could be an unresolved binary (with identical components) or it could be a non-member. PPL-14 was observed once during a flare event (see Table 1, Stauffer et al. 1995b). Dahm (2015) studied its radial velocity, compatible with the cluster, and its membership. We suggest that MHObd 3 is a suspected multiple system due to the absence of astrometric solution in *Gaia* DR2 and its position in the HRD (Fig. A.14a), as previously suggested Stauffer et al. (1998b). Two sources, MHObd 1 and MHObd 3, present low signal-to-noise ratio lithium detections (Stauffer et al. 1998b and 1998a), which would indicate that they are brown dwarfs or, at least, transition objects that have burned most of its initial lithium. IPL 43 has a low signal-to-noise ratio spectrum near 6 700 Å that precludes an assessment of the lithium equivalent width (Dahm 2015). Another significant aspect is the three lithium-poor objects studied by Martín et al. (2000): Roque 12 (spectral type M7.5), Roque 5 (M9) and Roque 25 (L0), all of them fainter than the LDB assumed by us (see the HRDs, Figure A.14). This fact might be due to the low quality of the spectra.

From the parallax distribution, Figure A.13, we discarded as members HCG 332, HCG 509, Calar 3, MHObd 1, and CFHT-Pl-12. About HCG 332 (HHJ 339) and HCG 509 (HHJ

<sup>11</sup> CFHT-Pl-9 and MHObd 6 are the same source (Stauffer et al. 1998b and Bouvier et al. 1998) even though the SIMBAD database treats them as two independent sources. We carried out a visual check of the charts from Stauffer et al. (1998b) and Bouvier et al. (1998) to confirm it. Also the counterpart of CFHT-Pl-10 in 2MASS catalogue is 2MASS J03443231+2525181.

430), Oppenheimer et al. (1997) suggested that they could simply be foreground weak-line T Tauri stars with the same proper motion and only a parallax measurement could make the membership assertion more certain. Thus, they are not members of the Pleiades as Stauffer et al. (2020) recently confirmed. CFHT-Pl-15, HCG 332, and HCG 509 have proper motions that are very different from the rest of the objects, as we show in Figure A.12. Furthermore, HCG 509, HCG 332, CFHT-Pl-15, and CFHT-Pl-18 are non-members<sup>12</sup> due to the low membership probabilities in the DANCe catalogue (Bouy et al. 2015 and Olivares et al. 2018) and in the work of Stauffer et al. (2020). In short, we show all the remarks of each object in Table E.4.

Stauffer et al. 1998b located the LDB with the sources CFHT-Pl-10 and CFHT-Pl-11, at  $M_{\text{bol LDB}} = 11.99$  mag ( $L_{\text{bol LDB}} = 1.259 \cdot 10^{-3} L_{\odot}$ ). On the other hand, Barrado y Navascués et al. (2004) located the LDB with the sources CFHT-Pl-09, CFHT-Pl-10, Roque 16 (CFHT-Pl-11), and Teide 2 (CFHT-Pl-13), at  $M_{\text{bol LDB}} = 12.14$  mag ( $L_{\text{bol LDB}} = 1.096 \cdot 10^{-3} L_{\odot}$ ). Dahm (2015) located the LDB at  $M_J = 9.73 \pm 0.05$  mag ( $L_{\text{bol LDB}} = 1.464^{+0.069}_{-0.066} \cdot 10^{-3} L_{\odot}$ ), assuming the distance from Melis et al. (2014). We located the LDB at  $L_{\text{bol LDB}} = 1.321^{+0.19}_{-0.089} \cdot 10^{-3} L_{\odot}$  and  $T_{\text{eff LDB}} = 2728 \pm 71$  K.

The lithium feature in Roque 5, Roque 12, Roque 25, and IPL 43 needs to be studied in more detail. MHObd 3 lacks astrometric solution in *Gaia* DR2 and requires a further study in terms of membership due to its position in the HRD (Figure A.14) and its lithium content. MHObd 1 was considered a non-member based on its parallax, even though this one is not very different from the previous members. It likely belongs to the tidal tail of the Pleiades.

### 5.8. Blanco 1

We selected 15 sources: 9 members studied both in Cargile et al. (2010) and Juarez et al. (2014); 1 member studied only in Cargile et al. (2010) and 5 members only studied in Juarez et al. (2014). We did not find any counterpart to B1opt-6335 in any catalogue; consequently, our sample ultimately contains 14 objects. Five targets have lithium detection and the rest lack any. We took the coordinates for each source from Moraux et al. (2007) since it was not possible to find the counterparts using the coordinates from Juarez et al. (2014). We gathered photometric bands:  $I_{cz}$  from Moraux et al. (2007), and  $BV$  from Cargile et al. (2009) for the object JC0-F18-88.

All the objects have a counterpart in *Gaia* DR2, except the faintest object CFHT-BL-49. Then, CFHT-BL-36 has a negative parallax,  $\varpi = -0.28 \pm 1.35$ , and CFHT-BL-45 is detected in *Gaia* DR2 but lacks astrometric solution.

From the VPD, Fig. A.15 left, we discarded as members CFHT-BL-29 and CFHT-BL-36. We also note that sources CFHT-BL-38 and CFHT-BL-43 have large uncertainties; CFHT-BL-16, CFHT-BL-36, and CFHT-BL-38 have parallaxes outside the percentiles of the parallax PDF (see Fig. A.15) and we considered them as non-members. We note that although CFHT-BL-43 is within the parallax distribution, it has huge uncertainties. All the objects from Juarez et al. (2014) have a radial velocity within the range of 2 to  $+10$  km s $^{-1}$  in  $3\sigma$  (see Figure 4 from Juarez et al. 2014), however, some objects are not within this range in  $1\sigma$ . Under this criterion, CFHT-BL-22,

CFHT-BL-25, CFHT-BL-29, CFHT-BL-36, and CFHT-BL-45 fall into the category of non-members. Lastly, we note that CFHT-BL-22 shows lithium in its spectrum even though it is hotter and brighter than other lithium-poor objects (beyond effective temperature and bolometric luminosity uncertainties). It fulfills the proper motion, distance membership criterion and, according to Juarez et al. (2014), it is currently depleting lithium.

Cargile et al. (2010) delimited the LDB between CFHT-BL-24 and CFHT-BL-38, at  $L_{\text{bol LDB}} = 1.26^{+0.40}_{-0.30} \cdot 10^{-3} L_{\odot}$ . Juarez et al. (2014) used the sources CFHT-BL-22 and CFHT-BL-38 to establish the LDB boundaries, so the updated Blanco 1 LDB is located at  $\log(L_{\text{bol LDB}}/L_{\odot}) = -2.910^{+0.062}_{-0.105}$  ( $L_{\text{bol LDB}} = 1.230^{+0.189}_{-0.264} \cdot 10^{-3} L_{\odot}$ ). We located the LDB at  $L_{\text{bol LDB}} = 1.68^{+0.62}_{-0.26} \cdot 10^{-3} L_{\odot}$  and  $T_{\text{eff LDB}} = 2746 \pm 71$  K (see the HRD, Figure A.16b). If we discarded those sources whose radial velocities are not within the range proposed by Juarez et al. (2014) in  $1\sigma$  (see text above and Figure A.16c), we located the LDB at  $L_{\text{bol LDB}} = 1.182^{+0.69}_{-0.099} \cdot 10^{-3} L_{\odot}$  and  $T_{\text{eff LDB}} = 2746 \pm 71$  K. We consider the last criterion because it contains the cleanest sample. There are few objects around the LDB and it would be interesting to perform a monitoring process with a wealth of objects.

### 5.9. The Hyades

We gathered 34 sources from different works: 12 sources from Hogan et al. (2008), from which 6 have a spectrum to determine if they are lithium-rich objects (Martín et al. 2018); 1 source from Pérez-Garrido et al. (2017), the L5 lithium-rich brown dwarf 2MASS J04183483+2131275 (2M0418, Lodieu et al. 2018) and 21 sources from Bouvier et al. (2008), of which only CFHT-Hy-10, CFHT-Hy-11, CFHT-Hy-12, CFHT-Hy-13, CFHT-Hy-19, CFHT-Hy-20, and CFHT-Hy-21 have spectra, but do not cover the lithium feature. It is important to note that Hya10 is not considered a definitive lithium-rich object in Martín et al. (2018) due to its poor detection. Nevertheless, we studied both situations, lithium-rich and lithium-poor object, intending to examine the location of the LDB and possible variations. In short, there are only lithium measurements for 7 objects. From our selection, Hya09, Hya10, Hya12, 2M0418, CFHT-Hy-20, and CFHT-Hy-21 do not have a counterpart in *Gaia* DR2, whilst, Hya02, Hya04, Hya05, Hya07, Hya11, and CFHT-Hy-16 do have a counterpart but lack proper motions and parallaxes due to their faintness.

We collected additional data from different works: proper motions and distances from Hogan et al. (2008); photometric bands  $I_{cz}JHK$  and proper motions from Bouvier et al. (2008); photometric data in the  $J$  band, proper motions and distances from Lodieu et al. (2014); proper motions from Pérez-Garrido et al. (2017); spectrophotometric distances calculated using the photometry from Martín et al. (2018); and ground based parallaxes and proper motions from Lodieu et al. (2019b).

We considered in our study CFHT-Hy-19 (19 in Fig. A.17) and CFHT-Hy-20 (20 in Fig. A.17) as foreground sources. In addition, we noted that CFHT-Hy-21 and Hya11 have large uncertainties. We did not rule out any source from the VPD because all sources fall within the bulk of previous members.

On the question of distances and parallaxes, different works carried out calculations with different approaches: spectroscopic distances based on an absolute magnitude versus spectral type relationship (Lodieu et al. 2014, Pérez-Garrido et al. 2017 and Martín et al. 2018), or from the proper motion of the object and

<sup>12</sup> Olivares et al. (2018) use a membership probability threshold  $p = 0.84$  (the one with higher accuracy and only for classification purposes). On the other hand, Bouy et al. (2015) use a threshold of  $p = 0.75$ .

the cluster velocity (see Equation 3 from Hogan et al. 2008). We followed the same method that we used before for the open clusters with the *Gaia* DR2 data (see Section 4.3). We show all the information in Appendix E.

Martín et al. (2018) located the LDB between the lithium-poor Hya11 and the lithium-rich sources Hya09 and Hya12 at  $L_{\text{bol}} \text{LDB} = 0.079_{-0.021}^{+0.028} \cdot 10^{-3} L_{\odot}$ . They calculated bolometric luminosities of the sources assuming calibrations for field L dwarfs to avoid any dependence on the distance. Later, Lodieu et al. (2018) added the lithium-rich source 2M0418 and locate the LDB at  $L_{\text{bol}} \text{LDB} = 0.0501_{-0.0074}^{+0.0088} \cdot 10^{-3} L_{\odot}$ . We located the LDB at  $L_{\text{bol}} \text{LDB} = 0.125_{-0.013}^{+0.019} \cdot 10^{-3} L_{\odot}$ , and  $T_{\text{eff}} \text{LDB} = 2021 \pm 71 \text{ K}$  (see Figure A.18b). If we considered that Hya10 is not a lithium-rich object (see text above), the LDB location does not change, only the uncertainties change slightly:  $L_{\text{bol}} \text{LDB} = 0.124_{-0.016}^{+0.019} \cdot 10^{-3} L_{\odot}$  (Fig. A.18c).

The Hyades is the only stellar association whose LDB is placed at L spectral types. Another fact is that all sources except 2M0418 does not have the H $\alpha$  feature in emission. It would be interesting to study whether this effect takes place in L spectral type objects in younger associations and establish whether it can be an indicator of age.

### 5.10. Beta Pictoris moving group

We took a sample of 127 sources, all M dwarfs, collected from Shkolnik et al. (2017). This work is our starting point because it gathers information about multiple systems, possible outliers, and equivalent widths of the lithium feature. We cross-matched the 127 sources with *Gaia* DR2, by visual inspection using ESASky.

Our final LDB sample contains 138 sources. Some of them have several counterparts associated in the *Gaia* DR2 catalogue, and they may be multiple systems. In some cases, the multiple system is only well resolved in *Gaia* DR2 (with individual parallaxes, proper motions and photometric bands), for instance, 20085368 (Fig. 7). Consequently, the object is a merge of several sources and its stellar parameters are affected. These objects are considered multiple systems in our study (marked as ‘CMS’ in Table E.4.). In others, the initial source has several associated background objects, and they might contaminate the photometry of the main object, for instance, 18420438 (Fig. 7). We can also have a combination of both cases: a multiple system only well resolved in *Gaia* with several associated background objects, for instance, 05015881 (Fig. 7) or 03393700. The photometric data are probably blended and could have erroneous stellar parameters. We marked them as contaminated photometry (CP) in Table E.4. Finally, we searched other works to identify additional multiple systems in our LDB sample: Mason et al. (2001), Beuzit et al. (2004), Bergfors et al. (2010), and successive references.

Only three sources, (01112542, 03323578, and 05241914<sup>13</sup>) do not have a counterpart in *Gaia* DR2 and nine lack astrometric solutions. All the information related to binary, multiple systems, and background sources associated with any object that belongs to our LDB sample is shown in the Appendix C.

The members are sparse and spread over the sky, located between 9–73 pc (Malo et al. 2013), so there is not any over-density in the sky and we cannot discard any member based on their

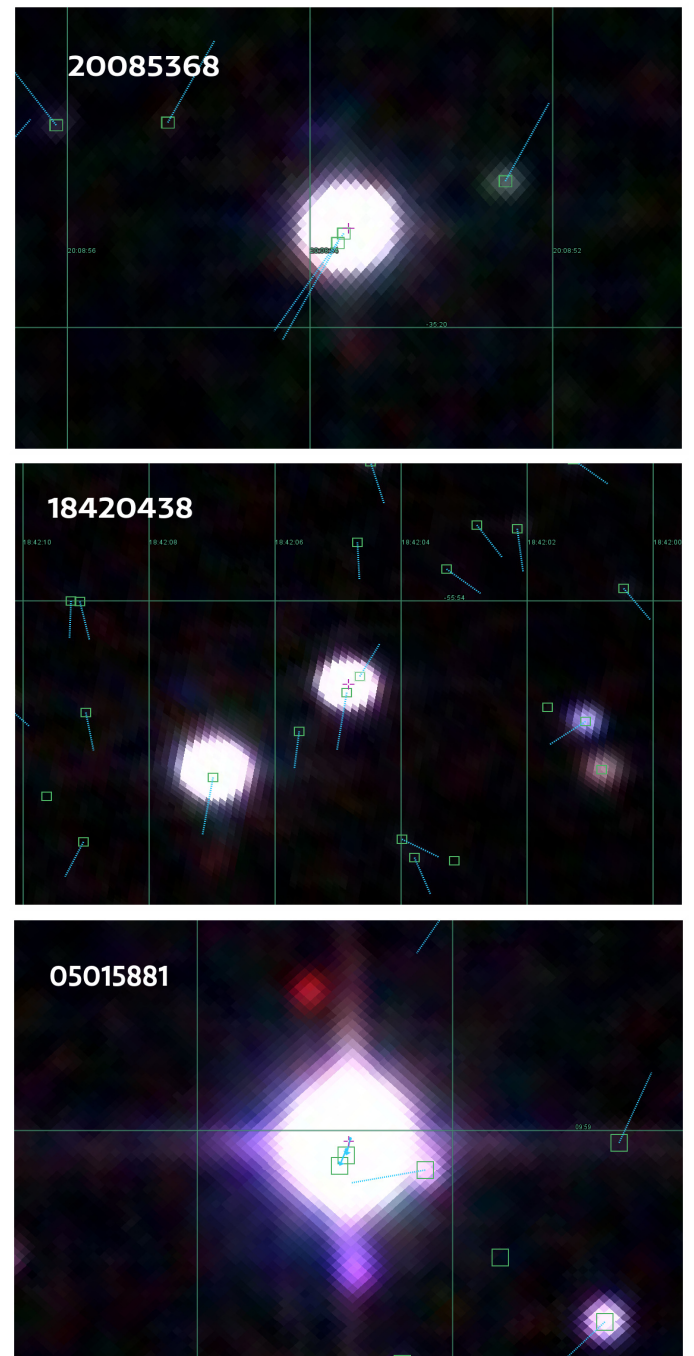


**Fig. 7.** 2MASS RGB images of three remarkable sources belonging to BPMG. The main source, 2MASS catalogue, is shown with a purple cross, the *Gaia* DR2 counterparts are shown with green squares and proper motions- with cyan dotted lines. **Top:** 20085368 is a binary system resolved with *Gaia* DR2. **Medium:** 18420438 is a source whose photometry may be contaminated by a background source. **Bottom:** 05015881 is a binary system whose photometry is resolved in *Gaia* DR2 and there is a very close background source.

VPD. Initially, we did not discard any source based on their parallaxes. Nevertheless, some of them might be outliers because they have significantly smaller parallaxes than other members: 03255277, 03370343, 11493184, 15063505, and 18435838.

We show in the HRD, Figure A.19, that most of the sources follow the main sequence and recognise the region delimited by the lithium-poor sources. The faintest ones give an idea

<sup>13</sup> These objects are not extremely faint and cool, have a counterpart in other surveys like 2MASS, and the SEDs do not have strange behaviours. The most plausible reason that they do not appear in *Gaia* DR2 is that the astrometric solution does not converge, because they are multiple systems.

of the suspected LDB, which is illustrated in Figure A.19b. There may be several explanations of why a lithium-rich source lies above the single star locus in a HRD, (e.g. multiplicity, high rotational velocities, or activity) and there is an explanation of why a lithium-poor source lies below the single star locus: it is probably a field star, older than the association (a non-member). There are six lithium-poor objects below the main sequence; three of them are: 01365516, 05363846, and 23512227, which are located at fainter bolometric luminosities than the suspected LDB and they might be non-members. In contrast, the distribution of lithium-rich sources along the main sequence is blurred. After discarding multiple systems and sources with possible contaminated photometry (see Figure A.19b), we identified eight lithium-rich sources brighter than the suspected LDB: 05082729, 20333759, 00501752, 17173128, 18030409, 02450826, 18011345, and 05061292. Two of them have undergone high activity periods: 05082729 with  $L_x/L_{\text{bol}} = -3.19$  and 20333759<sup>14</sup>, with  $L_x/L_{\text{bol}} = -3.15$  exhibited a strong X-ray to bolometric luminosity (Messina et al. 2017) and the multi-epoch radial velocity measurements (see Malo et al. 2014b) have ruled out its binary nature. This object suffered a flare with a magnitude increase of  $\Delta V = 3.29$  mag. The rest of sources are above the suspected LDB, three with  $L_{\text{bol}} \sim 50-60 \cdot 10^{-3} L_{\odot}$  (00501752, 17173128, and 18030409) and the other three with  $L_{\text{bol}} \sim 30 \cdot 10^{-3} L_{\odot}$  (02450826, 18011345, and 05061292). We may need further analysis to find out if they are outliers or if their positions are related to other effects, for instance, multiplicity.

Song et al. (2002) located the LDB between the lithium-poor WW PsA (22445794) and the lithium-rich Tx PsA (22450004), with both sources constituting the wide binary system HIP 112312, at  $L_{\text{bol LDB}} = 40.2^{+20.6}_{-13.6} \cdot 10^{-3} L_{\odot}$ . Binks & Jefries (2014) located the LDB as a rectangular region separating lithium-poor from lithium-rich sources in several colour-magnitude diagrams and calculated from the position of the central points of the boxes at  $L_{\text{bol LDB}} = 37.6^{+12.7}_{-9.5} \cdot 10^{-3} L_{\odot}$ . Malo et al. (2014b), using a maximum likelihood method for determining the LDB in terms of bolometric luminosity, located it at  $\log(L_{\text{bol LDB}}/L_{\odot}) = -1.49 \pm 0.08$  ( $L_{\text{bol LDB}} = 32.36^{+6.54}_{-5.44} \cdot 10^{-3} L_{\odot}$ ). Finally, Shkolnik et al. (2017) added new members and refined the LDB age (following the same procedure as Kraus et al. 2014 in THMG; see Section 2.11), but these authors did not find a clear gap in luminosities where there are lithium-poor and lithium-rich objects. They identified the LDB at  $M_K \text{ LDB} = 5.6 \pm 0.4$  mag, at  $L_{\text{bol LDB}} = 28.576^{+12.729}_{-8.806} \cdot 10^{-3} L_{\odot}$ , where there are an equal number of lithium-poor and lithium-rich sources, with eight stars in each group.

We located the LDB at  $L_{\text{bol LDB}} = 43.61^{+0.90}_{-0.81} \cdot 10^{-3} L_{\odot}$  and  $T_{\text{eff LDB}} = 3095 \pm 71$  K, using the following sources: 20083784, 00482667, 00193931, 18092970, 22450004, 22085034, 04480085, 04480258, 00194303, 23314492, 01303534, 05061292, 18011345, 21200779, 02450826, 21384755, 20333759, 05015665, 19300396, 05082729, 01351393, 22445794, 17173128, 02175601, 13215631, 18030409, 00501752, 05335981, 18055491, 21100535, 06131330, and 18151564, (see Figure A.19c). However, if we take into account the faintest lithium-poor sources, we can locate the LDB at  $L_{\text{bol LDB}} = 21.26^{+0.42}_{-0.21} \cdot 10^{-3} L_{\odot}$  and  $T_{\text{eff LDB}} = 2986 \pm 81$  K, see Figure A.19d. In this scenario, we discarded all the lithium-rich sources above the suspected LDB. All of them are bona-fide members, but two sources undergone high activity periods and the rest could be considered as multiple systems (see previous

paragraphs). In this case, the LDB locus is located at cooler effective temperatures and fainter bolometric luminosities  $\Delta L_{\text{bol}} = 25.35 \cdot 10^{-3} L_{\odot}$ , which leads to a 7 to 10% Ma age variation. A comparison of both criteria reveals a difference in the LDB locus of a 119% in terms of bolometric luminosity and a 36% in terms of effective temperature. We decided to use the first scenario because there is no reason to rule out the lithium-rich sources.

In addition, several blended objects require actual bolometric luminosity and effective temperature estimations. In addition, there are nine lithium-rich objects in the HRD region where lithium content should have been depleted: 02272804, 02450826, 00501752, 18011345, 17173128, 18030409, 05061292, 05082729, and 20333759, so further data are required to determine exactly how the multiplicity or activity in the X-Rays domain (or, perhaps, erroneous membership classification) might be associated with this effect. Due to the proximity of these objects, the quality of the astrometric parallax is quite good. A new membership assignment using excellent astrometric and spectroscopic data as Miret-Roig et al. (2020) for less massive objects might resolve this jigsaw puzzle.

### 5.11. Tucanae-Horologium moving group

We collected a total of 110 sources with parallax measurements from *Gaia* DR2, all of them confirmed as members, with spectral type M and lithium information taken from Kraus et al. (2014). We have followed the same criteria as them to determine whether the object is lithium-rich or not: one lithium-rich object has  $\text{EW}_{\text{Li}} > 0.100 \text{ \AA}$  and one lithium-poor object has  $\text{EW}_{\text{Li}} < 0.100 \text{ \AA}$ . We gathered all the photometric data through VOSA.

There are two binary systems confirmed through spectroscopic data (Kraus et al. 2014): 020701764406380 and 045153034647309. We deemed these objects as multiple systems, marked as “CMS” in Table E.4. Two sources deviate in the HRD (Fig. A.20): 03050976-3725058 (5.465 mas, 178 pc) and 21354554-4218343 (0.735 mas, 563 pc), they are located quite above the rest of sources, so we considered them as non-members. The source 22444835-6650032 might be a multiple system due to its position in the HRD. Other sources with a similar spectral type (our source spectral type is M4.8) have bolometric luminosities half of that of our source. However, Gagné et al. (2015) and Schneider & Shkolnik (2018) do not suggest anything related to possible multiple systems.

Kraus et al. (2014) quantified the location of the LDB at  $M_{\text{bol}} = 9.89 \pm 0.10$  mag,  $L_{\text{bol LDB}} = 8.710^{+0.840}_{-0.767} \cdot 10^{-3} L_{\odot}$ . They defined the LDB identifying the limit where equal numbers of lithium-depleted and lithium-bearing stars encroach onto the opposite side of the boundary. We located the LDB in the same way as we did in the rest of associations at  $L_{\text{bol LDB}} = 8.572^{+0.028}_{-0.11} \cdot 10^{-3} L_{\odot}$  and  $T_{\text{eff LDB}} = 2935 \pm 71$  K (see Fig. A.20b). If we assumed that 22444835-6650032 is a multiple system, the LDB location changes in terms of bolometric luminosity:  $L_{\text{bol LDB}} = 7.486^{+0.054}_{-0.11} \cdot 10^{-3} L_{\odot}$ , a change of 15% in terms of bolometric luminosities that produces an age increase of 2 and 6 Ma (6 and 10%) depending on the evolutionary model used (see Fig. A.20c). This last case is the one we selected.

The membership selection from Kraus et al. (2014) based on lithium measurements might introduce a bias in the location of the LDB (see Section 5 from that work). A possible solution would be to carry out a new membership assignment, as we propose for the BPMG low-mass objects.

<sup>14</sup> Also known as SCR J2033-2556 AB

### 5.12. 32 Ori moving group

To assess the LDB, we collected 33 M dwarfs from Bell et al. (2017). However, this number rises to 36 thanks to the multiplicity of three sources discovered after we cross-matched our input catalogue with *Gaia* DR2. Then, we have THOR-14Aa (3341625121978020736) and THOR-14Ab (3341625126275164032) instead of THOR 14A; THOR-17Aa (3389908598860532096) and THOR-17Ab (3389908598858685696) instead of THOR-17A; and THOR-40a (3341538436655619840) and THOR-40b (3341538436653898240) instead of THOR-40. THOR-14Aa and THOR-14Ab are two sources in *Gaia* DR2 with different astrometric parameters, unlike the rest of the photometric surveys, where they are blended. The bolometric luminosity is obtained with the total observed blended flux and calculated at both distances. All the sources have a counterpart in the *Gaia* DR2 catalogue, but THOR-17Aa, THOR-17Ab, THOR-18, THOR-35, THOR-36, THOR-40a and THOR-40b lack of parallaxes and proper motions.

Previous works (Bell et al. 2017 and Murphy et al. 2020) reported additional information that we took into account. THOR-17A (so THOR-17Aa, and THOR17Ab), THOR-18, THOR-21, THOR-26, and THOR-37 showed strong  $\text{He I } \lambda 5876\text{\AA}$  and  $6876\text{\AA}$  emission lines. There are several confirmed spectroscopic binaries: THOR-18, THOR-31 (a binary system), THOR-33 (a  $5''$  visual binary), and recently, Murphy et al. (2020) reported that THOR-42 (2MASS J05525572-0044266) is a young eclipsing binary comprising two pre-main sequence M dwarfs with combined spectral type M3.5. Some objects are suspected spectroscopic binary systems: THOR-15 and THOR-37; and others are considered fast rotators: THOR-05, THOR-07, THOR-23, and THOR-34.

32 Ori MG members are located in a bounded sky area (as we show in Figure 8), unlike other MGs (see SACY by Torres et al. 2006 or Malo et al. 2013). We performed a similar analysis to the one done with the open clusters. We discarded those sources that have parallaxes outside the interval  $\varpi \in (8.0, 11.0)$  mas: THOR-27 (a background source), along with three foreground sources, 2MASS J05053333+0044034, THOR-33, and THOR-34. We did not discard any source in the VPD because none of these sources are placed outside the area described by other members (as can be checked in Figure A.21. With regard to 2MASS J05053333+0044034 (plotted as 05053333), THOR-33, and THOR-34, they show discrepant proper motions.

Bell et al. (2017) located the LDB with the sources THOR 30 (lithium-poor object) and THOR 32 (lithium-rich object) at  $L_{\text{bol LDB}} = 31.7^{+1.6}_{-1.5} \cdot 10^{-3} L_{\odot}$ . We located the LDB at  $L_{\text{bol LDB}} = 41.3^{+2.4}_{-2.1} \cdot 10^{-3} L_{\odot}$  and  $T_{\text{eff LDB}} = 3135 \pm 71$  K, see Figure A.23b.

Stauffer et al. (2020) found that HCG 332 (HHJ 339) and HCG 509 (HHJ 430), as described in Section 2.7, share space motions that match those of 32 Ori MG. The inclusion of these objects in our analysis does not affect to the LDB loci, because HCG 509 is a binary system (Stauffer et al. 2020) and HCG 332 is fainter than the LDB. We also show these objects in the HRD, Figure A.23b. In addition, THOR-35 and THOR-36 lack parallaxes and are key objects around the LDB. So, it would be interesting to obtain parallaxes for them.

Finally, we studied the possibility that 32 Ori MG is made up of two populations, see the details in the Appendix D. Briefly, from our analysis we distinguished two populations: 32 Ori MG-Pop 1 with a LDB located at  $L_{\text{bol LDB}} = 41.2^{+2.2}_{-1.4} \cdot 10^{-3} L_{\odot}$  and  $T_{\text{eff LDB}} = 3157 \pm 71$  K (Fig. A.23c); and 32 Ori MG-Pop

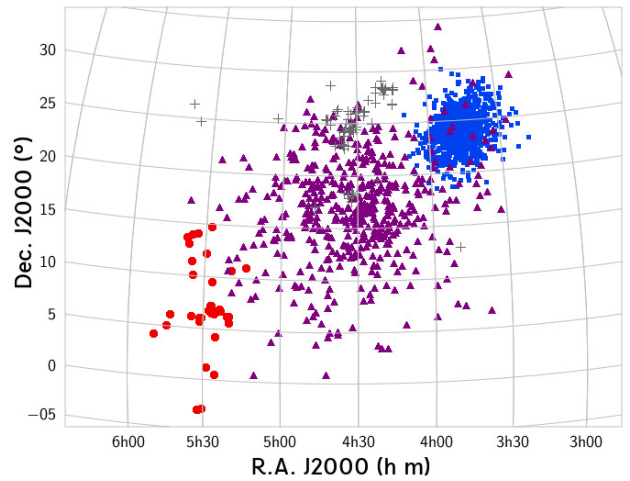


**Fig. 8.** Location of all 32 Ori MG sources (red circles from Bell et al. 2017), together with the Hyades (purple triangles), the Pleiades (blue squares), and Taurus members (grey pluses from Ducourant et al. 2005). The Hyades and the Pleiades members are taken from Gaia Collaboration et al. (2018b).

2 with a LDB located at  $L_{\text{bol LDB}} = 30.06^{+6.1}_{-0.32} \cdot 10^{-3} L_{\odot}$  and  $T_{\text{eff LDB}} = 3098 \pm 71$  K (Fig. A.23d); In addition we did an extra analysis. The 32 Ori MG sources belong to two different stellar groups from Kounkel & Covey (2019): Theia 133 and Theia 370. We located the LDB at  $L_{\text{bol LDB}} = 39.4^{+3.9}_{-1.4} \cdot 10^{-3} L_{\odot}$  and  $T_{\text{eff LDB}} = 3139 \pm 71$  K, for Theia 133 (Fig. D.3a); and  $L_{\text{bol LDB}} = 29.8^{+2.4}_{-2.7} \cdot 10^{-3} L_{\odot}$  and  $T_{\text{eff LDB}} = 3087 \pm 71$  K, for Theia 370 (Fig. D.3b).

**Table 3.** LDB loci in terms of  $L_{\text{bol}}$ ,  $T_{\text{eff}}$  and the ages derived using several evolutionary models.

Stellar Association	$L_{\text{bol}} \text{ LDB}$ $10^{-3} [L_{\odot}]$	$T_{\text{eff}} \text{ LDB}$ [K]	LDB ages based on $L_{\text{bol}}$					
			D&M [Ma]	Burrows [Ma]	Siess [Ma]	Burke [Ma]	BT-Settl [Ma]	Pisa [Ma]
Alpha Persei	$2.98^{+0.35}_{-0.19}$	2 857	$69.8^{+4.5}_{-1.6}$ (3 222)	$76.1^{+3.3}_{-5.2}$ (3 113)	> 70 (< 3 230)	$77.8^{+2.5}_{-4.9}$ (3 109)	$79.0^{+1.5}_{-2.3}$ (2 983)	$70.1^{+2.8}_{-4.2}$ (3 001)
NGC 1960	$23.6^{+12}_{-4.9}$	3 123	$26.2^{+2.3}_{-5.4}$ (3 461)	$19.8^{+4.0}_{-4.0}$ (3 462)	$27.7^{+3.5}_{-5.6}$ (3 546)	$24.4^{+3.4}_{-4.6}$ (3 368)	$31.6^{+3.9}_{-4.7}$ (3 370)	$23.4^{+3.3}_{-3.8}$ (3 344)
IC 4665	$23.6^{+2.1}_{-1.6}$	3 110	$26.1^{+0.8}_{-1.0}$ (3 461)	$19.7^{+1.2}_{-1.2}$ (3 462)	$27.7^{+0.9}_{-1.1}$ (3 546)	$24.4^{+1.1}_{-1.5}$ (3 369)	$31.6^{+1.3}_{-1.6}$ (3 370)	$23.4^{+0.6}_{-0.8}$ (3 345)
NGC 2547	$11.13^{+2.4}_{-0.89}$	3 004	$40.6^{+2.3}_{-6.1}$ (3 377)	$35.1^{+1.5}_{-4.0}$ (3 329)	$40.1^{+1.3}_{-3.1}$ (3 440)	$36.7^{+1.9}_{-4.0}$ (3 236)	$43.5^{+1.7}_{-4.0}$ (3 267)	$34.1^{+1.2}_{-3.0}$ (3 229)
IC 2602	$7.14^{+1.2}_{-0.52}$	2 926	$51.1^{+2.3}_{-3.5}$ (3 342)	$45.6^{+1.8}_{-4.3}$ (3 265)	$50.2^{+3.1}_{-6.0}$ (3 351)	$47.6^{+1.8}_{-4.1}$ (3 191)	$52.5^{+2.2}_{-3.7}$ (3 203)	$42.5^{+1.7}_{-3.1}$ (3 160)
IC 2391	$5.93^{+0.23}_{-0.13}$	2 956	$56.5^{+0.6}_{-1.0}$ (3 307)	$49.9^{+0.7}_{-0.8}$ (3 240)	$57.4^{+0.8}_{-1.4}$ (3 308)	$52.0^{+0.9}_{-1.1}$ (3 162)	$57.7^{+0.5}_{-1.0}$ (3 170)	$47.0^{+0.6}_{-1.0}$ (3 134)
The Pleiades	$1.321^{+0.19}_{-0.089}$	2 728	$155.5^{+8.4}_{-17}$ (3 057)	$134.5^{+7.4}_{-13}$ (2 922)	> 70 (< 3 230)	$134.9^{+4.7}_{-9.7}$ (2 959)	$127.4^{+6.3}_{-10}$ (2 793)	$117.6^{+5.6}_{-9.7}$ (2 834)
Blanco 1	$1.182^{+0.69}_{-0.099}$	2 746	$168.6^{+9.3}_{-65}$ (3 031)	$146^{+10}_{-42}$ (2 891)	> 70 (< 3 230)	$146^{+12}_{-40}$ (2 935)	$137.1^{+7.0}_{-33}$ (2 758)	$126.6^{+7.8}_{-33}$ (2 800)
The Hyades	$0.124^{+0.019}_{-0.016}$	2 021	> 500 (< 2 265)	> 210 (< 2 741)	> 70 (< 3 230)	> 188 (< 2 818)	$695^{+85}_{-67}$ (1 969)	> 317 (< 2 331)
BPMG	$43.61^{+0.90}_{-0.81}$	3 095	$19.4^{+0.1}_{-0.1}$ (3 559)	< 18.5 (> 3 482)	$20.0^{+0.2}_{-0.2}$ (3 641)	< 18.1 (> 3 467)	$24.3^{+0.3}_{-0.3}$ (3 432)	$17.4^{+0.2}_{-0.2}$ (3 440)
THMG	$7.486^{+0.054}_{-0.11}$	2 935	$49.7^{+0.3}_{-0.1}$ (3 350)	$44.3^{+0.4}_{-0.2}$ (3 273)	$48.1^{+0.7}_{-0.3}$ (3 363)	$46.4^{+0.4}_{-0.2}$ (3 200)	$51.0^{+0.5}_{-0.2}$ (3 212)	$41.3^{+0.4}_{-0.2}$ (3 168)
32 Ori MG	$41.3^{+2.4}_{-2.1}$	3 135	$19.6^{+0.2}_{-0.2}$ (3 553)	< 18.5 (> 3 482)	$20.6^{+0.5}_{-0.6}$ (3 631)	$18.1^{+0.5}_{-0.5}$ (3 467)	$25.0^{+0.7}_{-0.8}$ (3 426)	$17.9^{+0.6}_{-0.5}$ (3 431)
32 Ori MG-P1	$41.8^{+2.2}_{-14}$	3 157	$19.6^{+4.6}_{-0.2}$ (3 555)	< 18.5 (> 3 482)	$20.5^{+5.0}_{-0.6}$ (3 634)	$18.1^{+4.0}_{-0.6}$ (3 467)	$24.9^{+4.5}_{-0.7}$ (3 427)	$17.8^{+4}_{-0.4}$ (3 433)
32 Ori MG-P2	$30.06^{+6.1}_{-0.33}$	3 098	$23.1^{+0.2}_{-2.9}$ (3 501)	< 18.5 (> 3 482)	$24.3^{+0.2}_{-2.4}$ (3 582)	$21.4^{+0.1}_{-1.9}$ (3 409)	$28.6^{+0.1}_{-2.0}$ (3 396)	$21.2^{+0.1}_{-1.9}$ (3 380)
Theia 133	$39^{+18}_{-17}$	3 139	$19.8^{+7.0}_{-1.6}$ (3 549)	< 18.5 <sup>+2.2</sup> (> 3 482)	$21.1^{+7.3}_{-3.3}$ (3 624)	$18.5^{+6.7}_{-0.7}$ (3 460)	$25.6^{+7.0}_{-5.5}$ (3 421)	$18.4^{+5.5}_{-3.4}$ (3 423)
Theia 370	$29.8^{+8.3}_{-8.4}$	3 087	$23.3^{+3.9}_{-3.4}$ (3 499)	< 18.5 <sup>+2.9</sup> (> 3 482)	$24.4^{+4.4}_{-3.0}$ (3 580)	$21.5^{+4.4}_{-2.6}$ (3 407)	$28.7^{+4.7}_{-2.6}$ (3 396)	$21.3^{+3.2}_{-2.5}$ (3 378)

$L_{\text{bol}}$  LDB and  $T_{\text{eff}}$  LDB are the locations of the LDB in terms of bolometric luminosity and effective temperature. The rest of the columns are the ages estimated using  $L_{\text{bol}}$  LDB and the next evolutionary models: D'Antona & Mazzitelli 1997 ("D&M"), Burrows et al. 1993 and 1997 ('Burrows'), Siess et al. 2000 ('Siess'), Burke et al. 2004 ('Burke'), Allard et al. 2012 ('BT-Settl'), and Tognelli et al. 2015 ('Pisa'). We add in parenthesis, below each estimated age, the  $T_{\text{eff}}$  LDB at which the LDB would be expected to be found, see Section 6.4.

**Notes:** We added the LDB ages of the 32 Ori MG subsamples and sub-populations for completeness (see Appendix D).

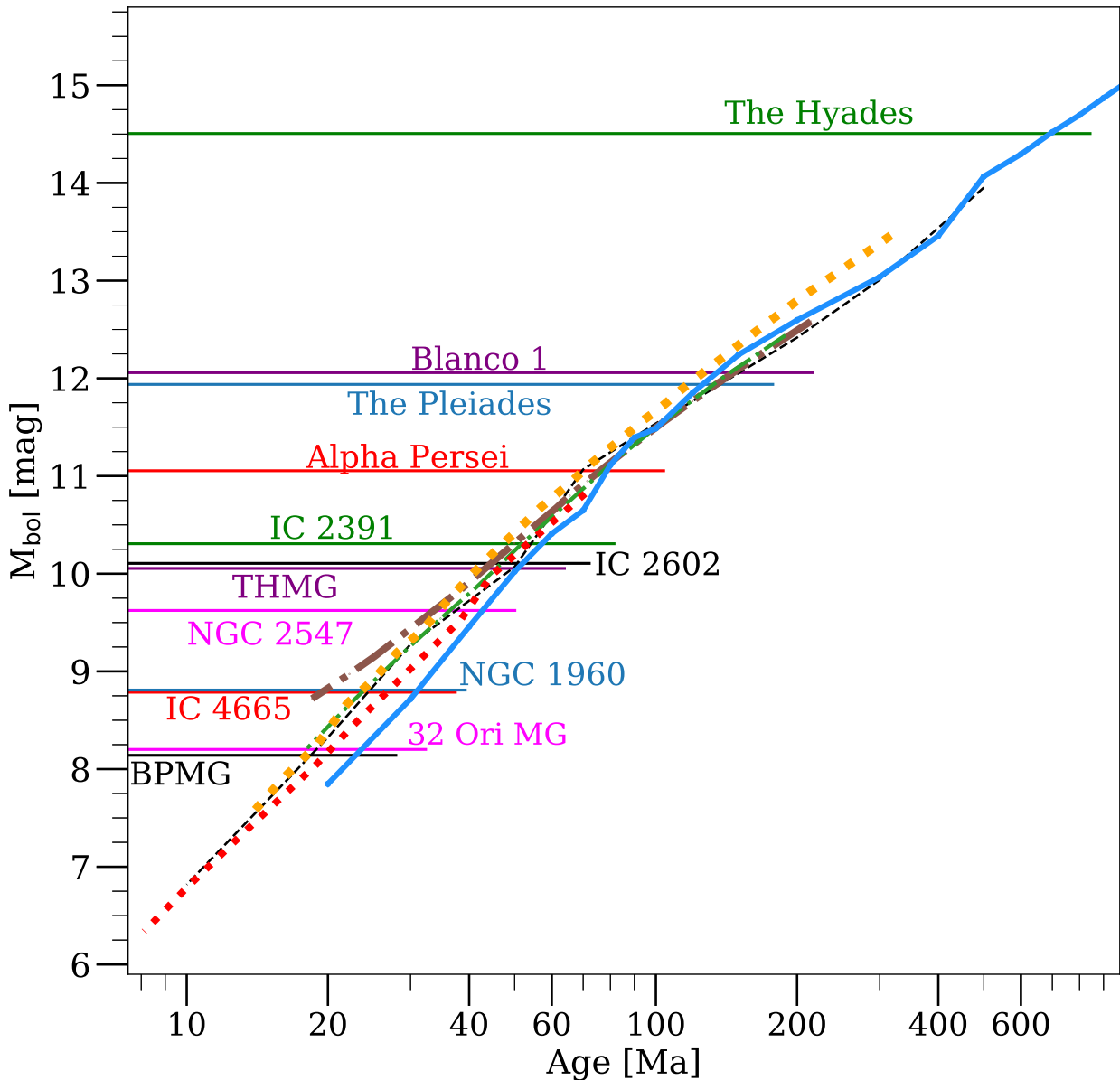


**Fig. 9.** Location of the LDB for all studied stellar associations and its relation with the age. We show bolometric magnitudes of the LDB for each stellar association as horizontal lines (several colours). Uncertainties are not shown for clarity. The lines that cross diagonally from the lower left corner to the upper right one correspond to different LDB models: the dashed black line is the D'Antona & Mazzitelli (1994) LDB, the dashed dotted brown thicker line is the Burrows et al. (1997) LDB, the dashed dotted green thinner line is the Burke et al. (2004) LDB, the dotted red line thicker corresponds to the Pisa LDB (Tognelli et al. 2015), the dotted red line thinner correspond to the Siess et al. (2000) LDB and the blue line is the BT-Settl LDB (Allard et al. 2013).

## 6. LDB error budget

In this section, we discuss the sources of error in our LDB loci and their derived ages. We study the accuracy of our derived stellar parameters, the importance of reddening in the LDB location, and we compare our LDB ages with those derived using other techniques. We also discuss some caveats in obtaining our estimations.

### 6.1. Accuracy of the stellar parameters

In order to estimate the accuracy of our stellar parameters, both assumed and calculated (metallicity, surface gravity, reddening, effective temperature, and distance), we made a comparison with the values from Anders et al. (2019)<sup>15</sup> and from Randich et al. (2018). In addition, we employed two grids of model atmospheres to study their effect on the derivation of the total flux of each object.

#### 6.1.1. Comparison with Anders et al. (2019)

Anders et al. (2019) derived stellar parameters, distances, and reddenings for  $285 \cdot 10^6$  stars down to  $G = 18$  mag, using the **StarHorse** code (Queiroz et al. 2018) and combining photometric catalogues and parallaxes from *Gaia* DR2. We calculated the difference between the **StarHorse** stellar parameters and the ones we either assumed or derived. We applied four filters to the **StarHorse** dataset: the first one with all the sources in common, the second one with a clean sub-sample that fulfils `SH_GAIFLAG="000"` and `SH_OUTFLAG="00000"` (see Anders et al. 2019 for an explanation), the third one only shows the members after our work, and the fourth one is the clean sub-sample of the previous one. We provide the results grouped into stellar associations in Table E.2. No object was found in the case of the NGC 2547 LDB sample, only two objects from Alpha Persei and the Pleiades, and only the hotter and brighter objects with  $T_{\text{eff}} > 3\,100$  K, from IC 4665 and Blanco 1. On the other hand, the least massive objects with later spectral types were found due to their proximity in the youngest (32 Ori MG and BPMG) and oldest (the Hyades) associations.

We assumed a homogeneous metallicity for all the objects in a stellar association given by the mean value (the values are shown in Table 1). Some of them are not tabulated in the models, so we have taken the closest one. Our fixed values and those calculated with **StarHorse** agree.

A comparison of the two approaches reveals that the fixed value of  $\log g = 4.5$  for all the objects is consistent. However, we discern that the **StarHorse** values in the Hyades, the oldest association, are close to  $\log g = 5.0$  dex instead of  $\log g = 4.5$  dex. We calculated the stellar parameters of the Hyades using  $\log g = 4.5$  and  $\log g = 5.0$  dex. The total flux,  $F_{\text{tot}}$ , is not affected by the change. The differences in terms of percentages are 0.7%, with a standard deviation of 3%. This fact is not reflected in the  $T_{\text{eff}}$ , as the calculated values using  $\log g = 5.0$  dex are hotter by 26 K on average (with standard deviation 115 K). So, we fixed  $\log g = 5.0$  dex for the Hyades and  $\log g = 4.5$  dex for the rest of the associations.

The comparison between our calculated distances and that in **StarHorse** must be done carefully. While Anders et al. (2019) re-calibrated the parallaxes and their uncertainties (see further

explanation in Table 1 and Section 2), we decided not to apply any corrections. The *Gaia* DR2 parallaxes show several systematic uncertainties on a small scale (depending on magnitude, colour, and position) and on a large scale (as the global parallax zero-point offset of  $-0.029$  mas, see further explanations from Arenou et al. 2018 and Lindegren et al. 2018). These last two papers suggest treating the parallax zero-point as an adjustable parameter, adding that this is not always possible for very small samples or when the distance is nearly constant in the sample, as in a stellar cluster. So, we decided not to apply this global offset in Sect. 6.3.

Concerning the distance calculations, Anders et al. (2019) adopted a Bayesian approach using elaborate priors with the aim of estimating distances for a complex variety of objects in all the Milky Way (priors include information about stellar evolutionary models and density laws for the main components of the Milky Way as the thin and thick disc, bulge, and halo, as well as the broad metallicity and age ones for those components). By contrast, our goal is to calculate the distance of an object (as well as possible) belonging to a stellar association, thus, we used a suitable Gaussian prior (see Section 4.2 for the explanation). Here, **StarHorse** gives the distance values in the 5th, 16th, 50th and 95th percentiles, where `dist50` is considered the main estimator of the distance, and the uncertainties are given by `dist16` and `dist84`. In our case, the maximum-a-posteriori is the main estimator of the distance, and the 2.5th and 97.5th percentiles give the uncertainties. However, in Figure 10, all the uncertainties were determined at 16th and 84th percentiles, showing a good agreement between both methods. The most significant discrepancies are found at distances  $d_{\text{MAP}} > 950$  pc. The poorest agreement is found in objects from NGC 1960 and IC 4665, which are the furthest associations. The NGC 1960 sample only contains four objects, two of them with low quality as it is shown by the **StarHorse** flags. The IC 4665 sample contains a large number of sources considered as non-members after this work. These objects have systematically higher **StarHorse** distances than our calculated values. As a result of the comparison, we can conclude that this effect affects non-member background objects.

Therefore, the mere fact of using the Bayesian approach is not enough to calculate reliable distance measurements. We assumed that all the objects belong to the open cluster and chose a prior accordingly. While bona fide members have accurate distances, the background objects and outliers with parallaxes higher than 20% are likely to be biased, as we see when making comparisons with **StarHorse** results. This suggests that it is necessary to discard outliers using the parallaxes instead of the calculated distances.

Another quantity, namely, interstellar reddening, affects the stellar parameters and in particular, the effective temperature. We show our results for the effective temperatures with those from **StarHorse** together with the reddening,  $A_V$  in Figure 11. We note that  $T_{\text{eff}}$  is our calculated effective temperature, and `teff50` is the **StarHorse** effective temperature at 50th percentile. As a matter of fact, we can distinguish three different zones depending on the effective temperature: (1) zone A with  $T_{\text{eff}} < 3\,200$  K, populated by the objects that are considered in the LDB location, (2) zone B with  $T_{\text{eff}} \in (3\,200, 3\,700)$  K, and (3) zone C with  $T_{\text{eff}} > 3\,700$  K. In zone A, there is no significant difference be-

<sup>15</sup> We accessed the data via the *Gaia* mirror archive at the Leibniz-Institut für Astrophysik Potsdam: <https://gaia.aip.de/>, using the *Gaia* DR2 `source_id`.

<sup>16</sup> Other works, as Meingast et al. (2021), do not apply the parallax-offset value, because it is a global average and can be significantly different on local scales.

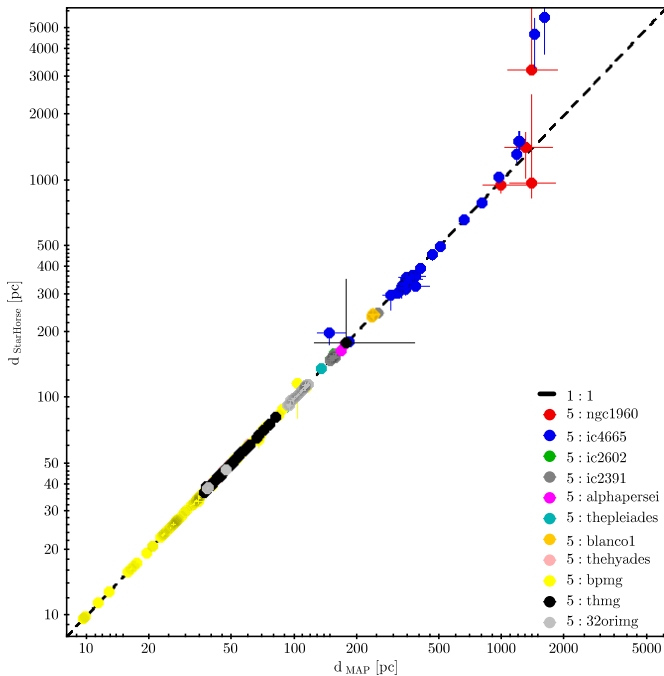


**Fig. 10.** Comparison of our calculated distances,  $d_{\text{MAP}}$  and those derived with StarHorse (Anders et al. 2019).

tween the two effective temperatures  $\Delta T_{\text{eff}} = -9$  K (standard deviation 127 K) and a  $\Delta A_V = -0.20$  mag (standard deviation 0.34 mag). There are objects from all the stellar associations included, but there is a greater presence of objects from the Hyades, BPMG, and THMG. One implication of this is the possibility that the best match corresponds to those objects with very low or null values of  $A_V$ , for instance, the Hyades, THMG, and BPMG. In zone B, we measured an offset of  $\Delta T_{\text{eff}} = -330$  K (standard deviation 468 K) and  $\Delta A_V = -0.63$  mag (standard deviation 0.76 mag), and we systematically found lower values than those from StarHorse. In zone C, in overall terms, there is an offset of  $\Delta T_{\text{eff}} = -440$ , on average (standard deviation 710 K), and  $\Delta A_V = -0.68$  mag on average (standard deviation 0.79 mag). We observed two trends: objects very close to the 1:1 line with small differences between  $T_{\text{eff}}$  and  $A_V$ , and a second group with  $\Delta T_{\text{eff}} > 500$  K. In the latter case, most of the objects are from IC 4665 and THMG.

The four NGC 1960 sources with counterparts in StarHorse are located inside the range of  $T_{\text{eff}} \in (3\,600, 4\,500)$  K and  $\text{teff50} > 4\,500$  K. In the range of  $T_{\text{eff}} \in (3\,250, 3\,600)$  K and  $\text{teff50} > 4\,500$  K, there are only sources from IC 4665, BPMG, THMG, and 32 Ori MG. In brief, sources with  $T_{\text{eff}} < \text{teff50}$  have values of the extinction  $AV50^{17}$  greater than the ones we have assumed. We distinguish three zones depending on their tendency even though there is no definitive explanation. The  $T_{\text{eff}} - A_V$  relation might be affected by the use of synthetic photometry from the Kurucz grid together with the extinction law used in StarHorse, the differential reddening in some stellar associations (e.g. the Pleiades: see Breger 1986, Stauffer & Hartmann 1987, Gibson & Nordsieck 2003a and 2003b) or both.

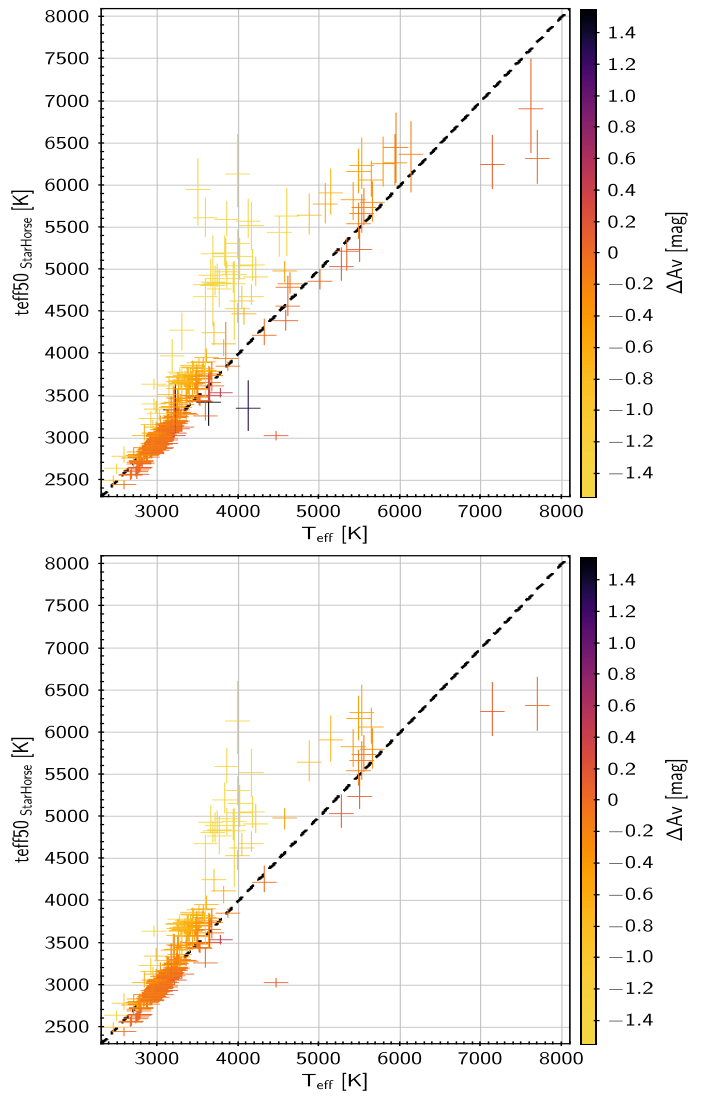


**Fig. 11.** Comparison of effective temperatures derived in Anders et al. (2019) and from VOSA. **Top:** Sources from the LDB samples. Note we did not find any NGC 2547 counterpart in StarHorse. **Bottom:** Only those sources considered as members after this work.

### 6.1.2. Comparison with Randich et al. (2018)

We compared our results with those obtained in Randich et al. (2018). In this work they employ the stellar parameters obtained from the *Gaia*-ESO Survey, GES (Gilmore et al. 2012), and derive reddening values comparing several grids of models with various colour-magnitude diagrams. We calculated the difference between their values and ours, for the four associations, we have in common: IC 4665, NGC 2547, IC 2602, and IC 2391 (see Table E.3). As with the StarHorse values, the assumed  $\log g = 4.5$  dex is consistent, although we seem to have an offset of  $-0.36 \pm 0.61$  dex.

These authors  $E(B - V)$  values are systematically higher than ours, of about 0.0477 mag, with a standard deviation of 0.0093 mag. This value is within the Gaia Collaboration et al. (2018b) uncertainties for the excess. As we will see in Section 6.2 and Appendix B, higher reddening values produced hotter effective temperatures. Figure 12 shows a temperature offset of approximately 200 K, probably caused by the values  $E(B - V)$ . Our effective temperature values were obtained from the SED after applying the assumed  $E(B - V)$  value, while values from

<sup>17</sup>  $AV50$  is the StarHorse line-of-sight extinction at  $\lambda = 5\,420$  Å,  $A_V$ , 50th percentile

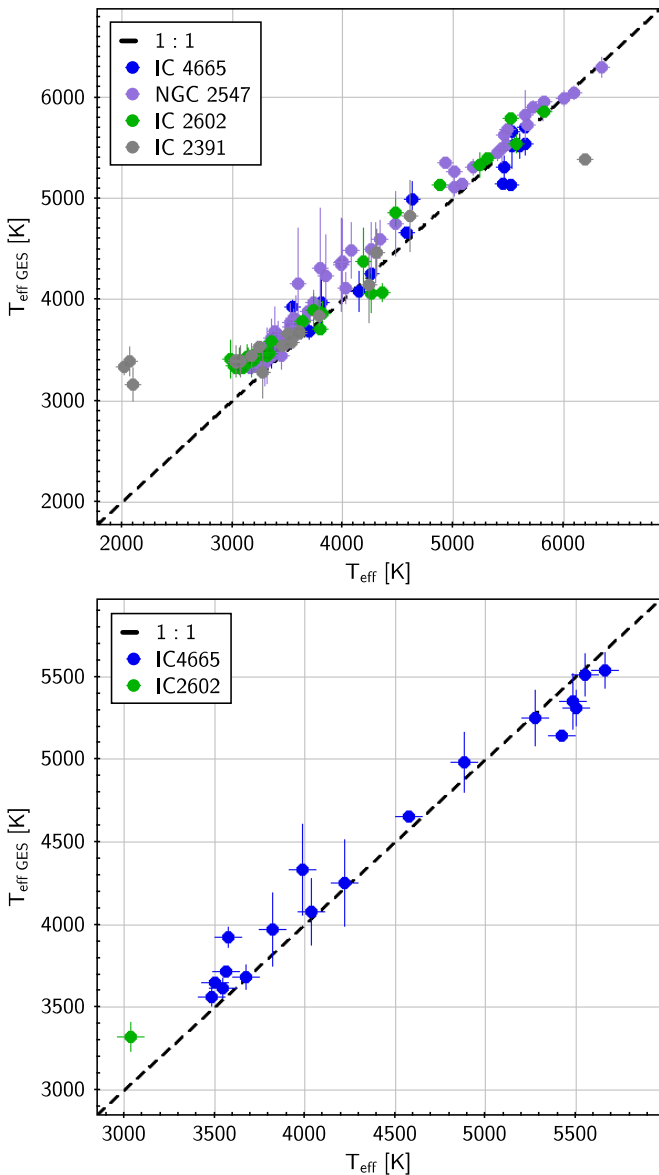


**Fig. 12.** Comparison of effective temperatures derived in Randich et al. (2018) and from VOSA. **Top:** All the sources are members from Gaia Collaboration et al. (2018b) with counterpart in Randich et al. (2018). **Bottom:** Only sources considered as members after this work from the LDB samples with counterpart in Randich et al. (2018).

Randich et al. (2018) are obtained from particular lines in the spectrum (Damiani et al. 2014).

#### 6.1.3. Impact of different model atmosphere grids on the total flux.

The amount of flux inferred from just one colour using grids of models is huge in typical bolometric corrections. In contrast, VOSA offers a panchromatic bolometric correction based on the numerous photometric bands collected and their uncertainties (included in the quantity  $F_{\text{err}}$ , see Sect. 3.3). VOSA releases the  $F_{\text{obs}}/F_{\text{tot}}$  for all adjustments. This value is higher than 0.7 in our objects, so less than 30 % of the total flux comes from model atmospheres. As such, we do not expect a large effect due to the adopted synthetic spectra. Besides the effective temperature, synthetic spectra depend also on surface gravity and

metallicity. For these parameters, we assumed constant values, namely,  $[\text{Fe}/\text{H}] = 0.0$  and  $\log g = 4.5 \text{ dex}$  ( $\log g = 5.0 \text{ dex}$  for the Hyades), consistent with what has been done in previous works (see Sects. 6.1.1 and 6.1.2). It is likely that it does not increase the uncertainty in the  $F_{\text{tot}}$  estimation. However, to check the impact of the adopted spectra in the determination of bolometric luminosity, we compared the results obtained using two different grids of model atmospheres.

Our reference grid is the BT-Settl (Allard et al. 2012, see Section 4.3). We compared it with the MARCS grid (Gustafsson et al. 2008), using the standard metallicity class ( $[\text{Fe}/\text{H}] = 0.0$ ) and  $\log g = 4.5 \text{ dex}$ <sup>18</sup>. We calculated the  $F_{\text{tot}}$  in the wavelength range common to both models: from  $1300 \text{ \AA}$  to  $20 \mu\text{m}$ . The results for models with  $T_{\text{eff}} \in [2500, 3500] \text{ K}$  are given in Table 4, where  $F_{\text{tot}}$  is the integrated flux,  $\Delta F_{\text{tot}}$  is the difference of fluxes of the MARCS and BT-Settl models, and  $\% \Delta$  is the difference in percentage terms. The maximum difference is 5%, being less than 1% in most cases. Moreover, these effects are even smaller because in most of the targets the flux between  $u$  and  $K_s$  (and up to the  $W2$  photometric band) is determined by the observations only – and not by any model. Thus, we did not find any significant difference between the two grids in the effective temperature range of the LDB.

**Table 4.** Differences in fluxes between MARCS and BT-Settl model atmosphere.

$T_{\text{eff}}$ [K]	$F_{\text{tot}}$		$\Delta F_{\text{tot}}$	$\% \Delta$
	MARCS	BT-Settl		
	$10^7 [\text{erg/cm}^2/\text{s}/\text{\AA}]$			
2500	221.53	219.26	2.26	1.03
2600	259.12	264.74	-5.61	2.12
2700	301.45	317.76	-16.31	5.13
2800	348.60	355.87	-7.27	2.04
2900	401.11	401.46	-0.35	0.08
3000	459.35	457.79	1.55	0.33
3100	523.72	527.43	-3.70	0.70
3200	594.63	595.41	-0.77	0.13
3300	672.53	670.34	2.18	0.32
3400	757.86	757.62	0.23	0.03
3500	851.03	844.93	6.09	0.72

#### 6.2. Effects of reddening in the LDB

The reddening values vary greatly from one work to another for the same stellar association. Even if the same technique is used to calculate it, the isochrone fitting, the result is quite sensitive to the set of stellar models used to derive it, (see e.g. Gaia Collaboration et al. 2018b, Randich et al. 2018, Bossini et al. 2019.) In our analysis, we used the values of the reddening computed by Gaia Collaboration et al. (2018b), whenever possible, neglecting the uncertainties<sup>19</sup>. We used these values in order to compare age values determined with the same reddening and different technique (see Section 6.4).

Different methodologies reveal different reddening values, and a kaleidoscope study from diverse perspectives would be interesting. Another effect that may be related is differential red-

<sup>18</sup> BT-Settl CIFIST:

<http://svo2.cab.inta-csic.es/svo/theory/newv2/index.php>

MARCS: <https://marcs.astro.uu.se/index.php>

<sup>19</sup> Extinction values from Gaia Collaboration et al. (2018b) have an uncertainty of  $\Delta E(B - R) = 0.04 \text{ mag}$ .

dening, as occurs in the Pleiades (see Section 6.1.1), but that is beyond the scope of this work.

In order to quantify and make a rough estimate of how different values affect the location of the LDB (see Appendix B), we studied Alpha Persei assuming two very different single reddening values:  $A_V = 0.279$  mag (Gaia Collaboration et al. 2018b) and  $A_V = 0.055$  mag (Bossini et al. 2019). We chose this open cluster because the LDB is very clearly located. All the calculations are presented in Appendix B. If we assume  $A_V = 0.055$  mag, the LDB locus is at:  $L_{\text{bol LDB}} = 2.74^{+0.40}_{-0.15} \cdot 10^{-3} L_\odot$  and  $T_{\text{eff LDB}} = 2806 \pm 71$  K, which it means a variation of  $L_{\text{bol LDB}}$  of about  $-0.24 \cdot 10^{-3} L_\odot$ . So, the LDB is located at fainter luminosities, cooler effective temperatures, and the resulting age is older:  $81.3^{+2.4}_{-3.4}$  Ma (BT-Settl model from Allard et al. (2012)). Table B.2 shows the age differences between models. If we make a comparison with the ages determined using  $A_V = 0.279$  mag, we find age differences ranging from 3 to 6 Ma (about 3 to 9 %). However a more in-depth and systematic study of this variable is needed for each stellar association.

### 6.3. Effects of the parallax zero-point offset in the LDB

We studied how the inclusion of the *Gaia* DR2 global parallax zero-point offset (see Arenou et al. 2018 and Lindegren et al. 2018) affects the the average stellar association distance and its LDB. In addition, we studied possible differences between *Gaia* DR2 and EDR3.

We tested the impact of the global parallax zero-point offset on the average stellar association distance by adding  $+0.029$  mas to all parallaxes before performing our distance estimation. For the Hyades, we obtained  $d_{\text{mode}} = 47.368$  pc and the values at the 2.5th, 25th, 75th, and 97.5th percentiles are 60.684, 50.761, 44.412, and 36.530 pc, respectively (see Table 2). In the case of more distant stellar associations such as Alpha Persei, we calculated  $d_{\text{mode}} = 173.571$  pc with 2.5th, 25th, 75th, and 97.5th percentile values of 186.653, 178.254, 170.162, and 161.682 pc; and for the Pleiades we obtained  $d_{\text{mode}} = 135.352$  pc with percentile values of 146.899, 138.571, 132.554, and 124.234 pc. In these cases, the zero-point offset carries a change of up to a maximum of 1 pc. However the effect is larger in the most distant NGC 1960, with a  $d_{\text{mode}} = 1165.908$  pc and percentile values of 1455.688, 1241.557, 1103.338, 978.990 pc, which makes it a 40 pc closer.

In addition, we tested their impact on the derived  $L_{\text{bol LDB}}$ . We found that the effect is negligible for the Hyades  $L_{\text{bol LDB}} = 0.125^{+0.018}_{-0.017} \cdot 10^{-3} L_\odot$ , and the Pleiades:  $L_{\text{bol LDB}} = 1.32^{+0.17}_{-0.10} \cdot 10^{-3} L_\odot$ , where the LDB loci changes  $\Delta L_{\text{bol LDB}} = 0.001 \cdot 10^{-3} L_\odot$ , less than 0.1 %. After we applied the offset, we located the LDB for Alpha Persei at  $L_{\text{bol LDB}} = 2.94^{+0.36}_{-0.17} \cdot 10^{-3} L_\odot$ , which implies  $\Delta L_{\text{bol LDB}} = 0.04 \cdot 10^{-3} L_\odot$  fainter, and a change of 1.4% in  $L_{\text{bol LDB}}$ . The most pronounced case is that of NGC 1960 because it is the cluster with the smaller parallax and the most distant. After adding the offset, NGC 1960 it is placed 40 pc nearest and we located the LDB at  $L_{\text{bol LDB}} = 23.4^{+12}_{-4.8} \cdot 10^{-3} L_\odot$  that implies an LDB loci  $\Delta L_{\text{bol LDB}} = 0.199 \cdot 10^{-3} L_\odot$  smaller, and account for a 0.84% change in  $L_{\text{bol LDB}}$ . We conclude that the effect produced by zero-point offset parallax on the LDB locus is more pronounced for more distant stellar associations. However, it is not the predominant source of the uncertainty.

To conclude this analysis, we studied the effect of *Gaia* EDR3 parallaxes on the Alpha Persei distance and its LDB location. We obtained a  $d_{\text{mode}} = 173.840$  pc, with the following values at the 2.5th, 25th, 75th, 97.5th percentiles: 190.660,

179.165, 169.287, 160.242 pc. In this case, the distance is 0.62 pc closer ( $\Delta d_{\text{mode}}$ ). We do not see a substantial change in the location and size of Alpha Persei using the *Gaia* EDR3 parallaxes, although the parallax uncertainties are smaller in EDR3. We also checked the effect on the LDB location. We obtained:  $L_{\text{bol LDB}} = 3.11^{+0.25}_{-0.15} \cdot 10^{-3} L_\odot$ , which implies an LDB loci  $\Delta L_{\text{bol LDB}} = 0.125 \cdot 10^{-3} L_\odot$  brighter, and account for a 4.1% change in  $L_{\text{bol LDB}}$ . Furthermore, the age decreases by 0.9 Ma:  $78.1^{+1.0}_{-1.6}$  Ma, using the BT-Settl models.

### 6.4. Comparison between ages: several models and techniques

We locate the LDB in terms of the bolometric luminosity. The choice is due to the large dynamic range over which it varies in relevant age scales. We have found that the  $L_{\text{bol LDB}}$  and  $T_{\text{eff LDB}}$  produce different age values. In Table 3, we present our calculated  $L_{\text{bol LDB}}$  and  $T_{\text{eff LDB}}$ , and the age estimated using  $L_{\text{bol LDB}}$  and several grids of evolutionary models. In addition, as a test, we have calculated the  $T_{\text{eff LDB}}$  from the previously estimated age (between parentheses in Table 3). The purpose of that is to highlight the differences between the ages estimated from the  $L_{\text{bol LDB}}$  and the  $T_{\text{eff LDB}}$  (see Song 2016). This effect is significantly larger at brighter  $L_{\text{bol LDB}}$  (younger stellar associations) and we also show an evolutionary model dependence. A possible explanation is that the radii of these objects are larger than predicted by the models (Berger 2006, López-Morales 2007, Ribas et al. 2008), of up to  $14 \pm 2\%$  for a given bolometric luminosity for a sample of fast-rotating pleiades (Jackson et al. 2018). The rotation, accretion, and magnetic fields are effects that may be involved in this fact. In summary, it is necessary to determine precisely how radii affect effective temperatures and bolometric luminosities and, hence, the LDB.

What can be clearly seen in Table 3 and Figure 13 are the differences between ages calculated with different grids of evolutionary models, so there is a clear dependence. Any grid of models starts with a different equation-of-state, opacities, nuclear reaction rates and hypothesis, such as the convection model or the model atmosphere and leads to these age differences. We find several general remarks: (a) the Pisa and Siess LDB give ages younger than BT-Settl LDB; (b) the largest differences, 12 Ma, are found at  $M_{\text{bol}} \in [8.0, 9.5]$  mag, around 20 Ma, and account for 50% of the age, as we show for the BPMG with the Burrows and BT-Settl models.

We compared the LDB age scale derived using the BT-Settl luminosity-age relation with other age values (see Table 1) in Fig. 14. In general, the LDB ages are older than those estimated using a different method. When we compare our LDB ages with previous works using the same methodology, (as first pointed out Basri et al. 1996, Stauffer et al. 1998b) there is still some discrepancy, although not so pronounced. This result is probably related to the use of (a) different grid of models to derive ages, (b) individual parallaxes and to the fact that we discarded multiple systems together with foreground and background objects, and (c) in some cases, different reddening values.

On the other hand, we noted that the Pleiades PMS isochrone age from Bell et al. (2014) fits well with our LDB age because these models were re-calculated using this fact as input; Gaia Collaboration et al. (2018b) provided two age values for Blanco 1. From the main-sequence turn-off, they obtained an age of  $200^{+40}_{-26}$  Ma. However, if they used the LDB age of  $115^{+23}_{-15}$  Ma (Juarez et al. 2014), they would reproduce the lower main se-

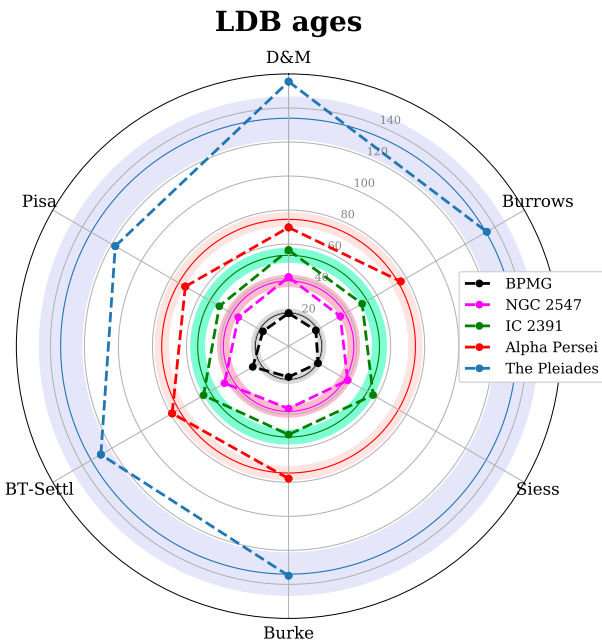


**Fig. 13.** Radar chart with LDB ages estimated using several evolutionary grid models. The age values showed as filled circles and connected with dashed lines are the same as Table 3. We also show the mean age value (thin solid line) and its standard deviation (the shadow region) for each association.

quence, with a marginal fit to the upper main sequence. We show both values in Figure 14.

A summary is presented in Table 6. Also, concerning studies on active stars, e.g. Reiners (2012), works like Malo et al. (2014b) partly resolved the age inconsistency between LDB and isochrone-fitting age for the BPMG. It would be interesting to extend this study to the rest of the associations.

In Figure 15 we plot our LDB ages together with other ages calculated with other techniques for a selection of stellar associations. Here, we also see the differences in age between the different techniques. It is worth noting that in some cases, parameters like reddening and distance are completely different from those used in our work. This fact may be the reason for the age discrepancies.

## 7. Conclusions and summary

The origin of the data and membership selection is very different for each stellar association and this fact can result in bias effects on the location of the LDB. In the case of the BPMG (**such us** Torres et al. 2006 or Shkolnik et al. 2017) and the THMG (Kraus et al. 2014), the membership selection was based on lithium measurements, so it is very likely that it might be a bias. We have tried to mitigate this possible effect by studying the membership of these objects based on the *Gaia* DR2 data: positions, parallaxes, and proper motions.

In line with our aim of creating a complete set of LDB age scale and following the example of Mermilliod (1981), we present a systematic and homogeneous study of twelve stellar associations. Our main results are as follows:

1. Twelve stellar associations with former LDB ages have been thoroughly studied conducting a careful and extensive bibliographic review to recover additional data to determine

possible outliers, as well as multiple systems and sources with unique features that can affect the LDB location.

2. We calculated individual distances for each source using a Bayesian statistic approach (*Kalkayotl*), and derived individual bolometric luminosities and effective temperatures for 500 sources, from their SEDs, using *Gaia* DR2 data including photometric data in a broad range of wavelengths, as well as the effects of metallicity and surface gravity. All the SEDs and images in several photometric bands were checked individually to determine special features.
  3. We fine-tuned previous memberships using individual parallaxes and proper motions from *Gaia* DR2, in addition to an HRD. The LDB has been determined using a jackknife method with a bootstrap re-sampling that takes into account the bolometric luminosities distributions of objects.
  4. We derived LDB ages using different theoretical evolutionary models. The discrepancies between them are due to the input physics. Also, we found a discrepancy between the ages derived using bolometric luminosities and those derived using effective temperatures. Since the ages from the bolometric luminosities are more robust to variations of  $A_v$  than the rest, we have selected them as the reference set.
  5. Our work reveals  $L_{\text{bol}}$  LDB values that are more precise than former ones in general terms, because our method is quite robust since we statistically determine them. Nevertheless, it is affected when: (a) the sequence of M-dwarfs (or L-dwarfs) objects is scarce, for instance, there are few objects with spectroscopic measurements that allow us to discern their lithium abundance; and (b) the sources that determine the LDB have larger bolometric luminosities uncertainties due to larger parallax uncertainties. In specific terms, our calculated  $L_{\text{bol}}$  LDB are in agreement with former ones for IC 4665, NGC 2547, IC 2602, IC 2391, the Pleiades, and Blanco 1. In contrast to earlier calculations, for the BPMG, the 32 Ori MG, Alpha Persei, and the Hyades, our  $L_{\text{bol}}$  LDB calculation is brighter. On the other hand, we found fainter  $L_{\text{bol}}$  LDB for NGC 1960 and THMG. All these discrepancies are mainly due to a new membership assignment, the update distance determination from individual parallaxes, or both – as in the case of the 32 Ori MG, NGC 1960, THMG, Alpha Persei, or the Hyades.
  6. We identified two peaks in the parallax distribution of the 32 Ori MG members. Besides, we checked that the 32 Ori MG members belong to two different stellar groups: Theia 133 and Theia 370, after Kounkel & Covey (2019). Finally, we located a tentative LDB and age for Theia 133 and Theia 370.
  7. The final results are summarized in Table 6, where the best age determinations are listed. Those were derived homogeneously and provide a well established relative age scale.
- Based on the theoretical calculations (Bildsten et al. 1997 and Ushomirsky et al. 1998), we would expect an abrupt transition between lithium-poor and lithium-rich objects. Nevertheless, this is not always the case, as we have found in our study of several stellar associations. One possible explanation may be the presence of unresolved multiple systems that could affect the interpretation and location of the LDB loci. Another explanation is that other phenomena or mechanisms come into play. The accretion, the rotation, and the magnetic fields (all correlated with

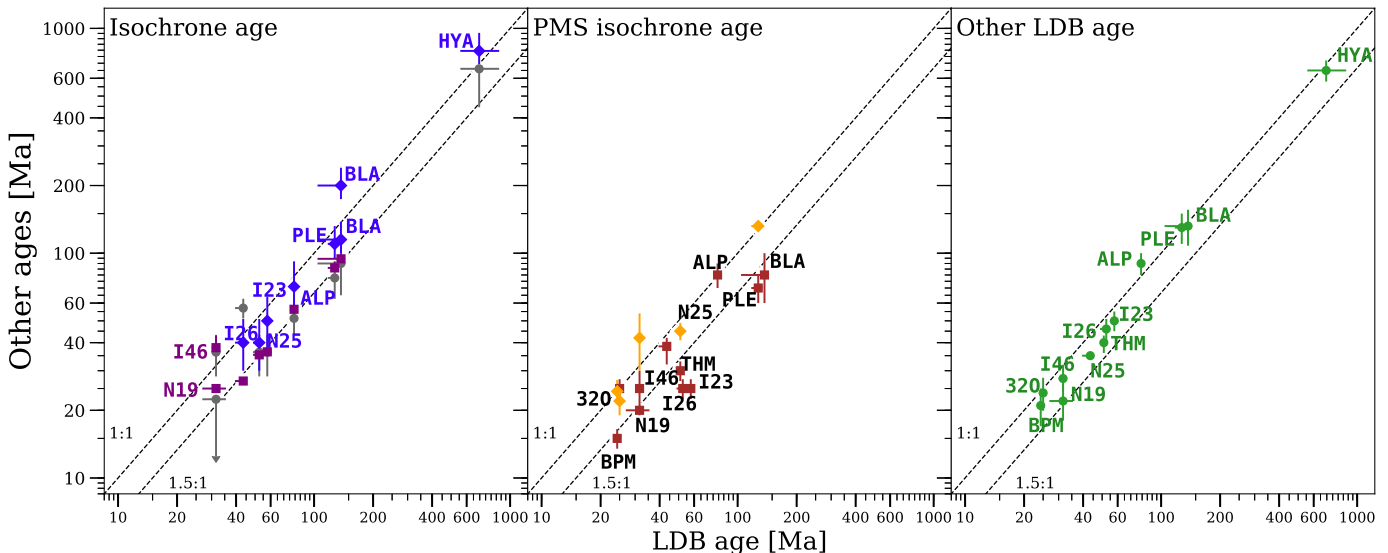


**Fig. 14.** Comparison between our LDB age and the age estimated using other techniques. **Left:** Ages derived from the isochrone fitting technique. The ages come from: Gaia Collaboration et al. 2018b (blue diamonds), Bossini et al. 2019 (purple squares), and Mermilliod 1981 (gray circles). **Middle:** Ages derived from the Pre Main-Sequence isochrone fitting technique. Orange diamonds represent PMS isochrone fitting ages: the Pleiades, BPMG, THMG and 32 Ori MG.- Bell et al. (2013, 2014, and 2015); and IC4665.- Cargile & James (2010). Brown squares are the rest of PMS isochrone fitting ages: NGC 1960.- Bell et al. (2013); IC 4665.- Manzi et al. (2008); NGC 2547.- Naylor & Jeffries (2006); IC 2602, IC 2391.- Stauffer et al. (1997); Alpha Persei.- Prosser (1992); the Pleiades.- Stauffer et al. (1995a); Blanco 1.- Cargile et al. (2009); BPMG and THMG.- Torres et al. (2006); and 32 Ori MG.- Mamajek (2007). **Right:** LDB ages derived from previous works. See the references in Table 1, its legend, and Section 2.

each other) prevent lithium depletion or generate different abundances for stars with the same mass (see Soderblom et al. 1993, Chabrier et al. 2007, Somers & Pinsonneault 2014, Jackson & Jeffries 2014a, Barrado et al. 2016, and Bouvier et al. 2018). Although only a few works have studied the LDB with some of these effects in mind (Malo et al. (2014b), Juarez et al. (2014), Messina et al. (2016)), it would be interesting to extend it to the other associations, and to carry out a study focussed on the multiplicity around the LDB. The stellar collision or the engulfment of a planetary object by a main star or brown dwarf (Abia et al. 2020 and Israeliyan et al. 2001), or the accretion of planetesimals leaving lithium abundance abnormalities in the atmosphere of the main object (Kaiser et al. 2021) might be another possible scenario. However, it remains to be seen how the change in the lithium abundance, the stellar parameters may be quantified, and how common these phenomena may be overall.

In a future work, we will analyse the LDB loci in terms of effective temperature and bolometric luminosity together, and we will incorporate data to help explain and quantify the effects of rotation and magnetic fields in the LDB age. It would be interesting to apply the Malo et al. (2014b) procedure to the rest of the associations, and check if the inconsistency is resolved between LDB and isochrone-fitting ages. It is necessary to populate some areas of the  $L_{\text{bol}}$  LDB range and study stellar associations, with ages ranging between that of the Pleiades and the Hyades, such as Praesepe or Coma Berenices (see Martín et al. 2020). There are no significant variations in our results based on the *Gaia* EDR3 data. However, we plan to update these results following the launch of *Gaia* DR3 in 2022.

**Acknowledgements.** A special thanks to Alcione Mora for his help with the *Gaia* data, Floor van Leeuwen for his help with the size of the clusters, Ana María Álvarez García, María Teresa Galindo Guil and Irene Pintos-Castro for their comments and suggestions, Agnes Monod-Gayraud for her careful reading of the manuscript and English corrections, and the anonymous referee for the comments that helped to improve the quality of this manuscript. FJGG acknowledges support from Johannes Andersen Student Programme at

the Nordic Optical Telescope. This research has been funded by the Spanish State Research Agency (AEI) Project No.PID2019-107061GB-C61 and No. MDM-2017-0737 Unidad de Excelencia “María de Maeztu”- Centro de Astrobiología (INTA-CSIC); AB acknowledges support by ANID, – Millennium Science Initiative Program – NCN19\_171 and BASAL project FB210003, and from FONDECYT Regular 1190748; VOSA, developed under the Spanish Virtual Observatory project supported from the Spanish MINECO through grant AyA2017-84089; the astronomical java software TOPCAT (Taylor 2005) and STILTS (Taylor 2006); NASA’s Astrophysics Data System Bibliographic Services; ESASky, developed by the ESAC Science Data Centre (ESDC) team and maintained alongside other ESA science mission’s archives at ESA’s European Space Astronomy Centre (ESAC, Madrid, Spain); the SVO Filter Profile Service (<http://svo2.cab.inta-csic.es/theory/fps/>) supported from the Spanish MINECO through grant AyA2014-55216; data from the European Space Agency (ESA) mission *Gaia* (<https://www.cosmos.esa.int/gaia>), processed by the *Gaia* Data Processing and Analysis Consortium (DPAC,<https://www.cosmos.esa.int/web/gaia/dpac/consortium>). Funding for the DPAC has been provided by national institutions, in particular the institutions participating in the *Gaia* Multilateral Agreement; The Pan-STARRS1 Surveys (PS1) and the PS1 public science archive have been made possible through contributions by the Institute for Astronomy, the University of Hawaii, the Pan-STARRS Project Office, the Max-Planck Society and its participating institutes, the Max Planck Institute for Astronomy, Heidelberg and the Max Planck Institute for Extraterrestrial Physics, Garching, The Johns Hopkins University, Durham University, the University of Edinburgh, the Queen’s University Belfast, the Harvard-Smithsonian Center for Astrophysics, the Las Cumbres Observatory Global Telescope Network Incorporated, the National Central University of Taiwan, the Space Telescope Science Institute, the National Aeronautics and Space Administration under Grant No. NNX08AR22G issued through the Planetary Science Division of the NASA Science Mission Directorate, the National Science Foundation Grant No. AST-1238877, the University of Maryland, Eotvos Lorand University (ELTE), the Los Alamos National Laboratory, and the Gordon and Betty Moore Foundation; the SIMBAD database, operated at CDS, Strasbourg, France; Funding for the Sloan Digital Sky Survey IV has been provided by the Alfred P. Sloan Foundation, the U.S. Department of Energy Office of Science, and the Participating Institutions. SDSS acknowledges support and resources from the Center for High-Performance Computing at the University of Utah. The SDSS web site is [www.sdss.org](http://www.sdss.org). SDSS is managed by the Astrophysical Research Consortium for the Participating Institutions of the SDSS Collaboration including the Brazilian Participation Group, the Carnegie Institution for Science, Carnegie Mellon University, the Chilean Participation Group, the French Participation Group, Harvard-Smithsonian Center for Astrophysics, Instituto de Astrofísica de Canarias, The Johns Hopkins University, Kavli Institute for the Physics and

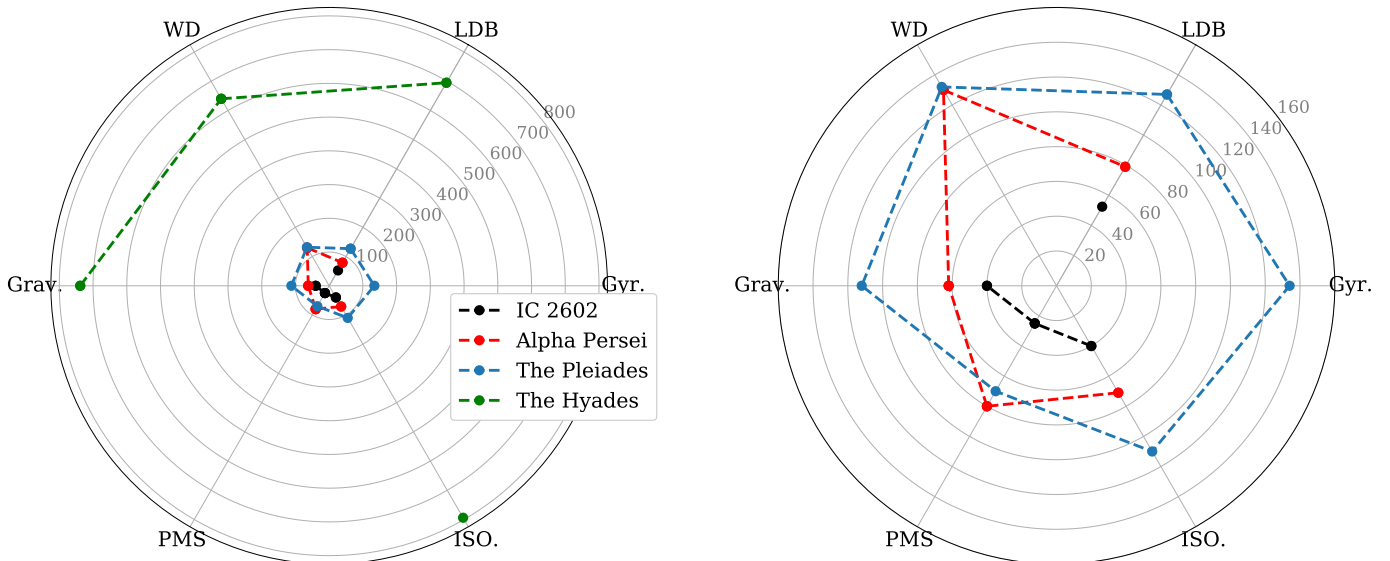


**Fig. 15.** Radar charts with ages in [Ma] calculated using different techniques: ‘LDB’ refers to our calculated ages using the BTSettl (see Table 3); ‘Gyr’ is the gyrochronology ages (Cargile et al. 2014); ‘ISO’ is isochrone fitting ages (Gaia Collaboration et al. 2018b); ‘PMS’ is PMS isochrone fitting ages from several works: IC 2602.- Stauffer et al. 1997; Alpha Persei.- Prosser 1992; the Pleiades.- Stauffer et al. 1995a. Then, ‘Grav’ is the gravity ages (David & Hillenbrand 2015); ‘WD’ is the white dwarf cooling sequence age Alpha Persei and the Pleiades.- Lodieu et al. 2019a; the Hyades.- Lodieu et al. (2019b). **Right:** Zoom onto the age range  $\in [0, 160]$  Ma.

Mathematics of the Universe (IPMU) / University of Tokyo, the Korean Participation Group, Lawrence Berkeley National Laboratory, Leibniz Institut für Astrophysik Potsdam (AIP), Max-Planck-Institut für Astronomie (MPIA Heidelberg), Max-Planck-Institut für Astrophysik (MPA Garching), Max-Planck-Institut für Extraterrestrische Physik (MPE), National Astronomical Observatories of China, New Mexico State University, New York University, University of Notre Dame, Observatório Nacional / MCTI, The Ohio State University, Pennsylvania State University, Shanghai Astronomical Observatory, United Kingdom Participation Group, Universidad Nacional Autónoma de México, University of Arizona, University of Colorado Boulder, University of Oxford, University of Portsmouth, University of Utah, University of Virginia, University of Washington, University of Wisconsin, Vanderbilt University, and Yale University; data products from the Wide-field Infrared Survey Explorer, which is a joint project of the University of California, Los Angeles, and the Jet Propulsion Laboratory/California Institute of Technology, funded by the National Aeronautics and Space Administration; data products from the Two Micron All Sky Survey, which is a joint project of the University of Massachusetts and the Infrared Processing and Analysis Center/California Institute of Technology, funded by the National Aeronautics and Space Administration and the National Science Foundation

- Anders, F., Khalatyan, A., Chiappini, C., et al. 2019, A&A, 628,  
 Arenou, F., Luri, X., Babusiaux, C., et al. 2018, A&A, 616,  
 Asplund, M., Grevesse, N., Sauval, A. J., & Scott, P. 2009, ARA&A, 47, 481  
 Bailer-Jones, C. A. L. 2015, PASP, 127, 994  
 Baines, D., Giordano, F., Racero, E., et al. 2017, PASP, 129, 028001  
 Barentsen, G., Farnhill, H. J., Drew, J. E., et al. 2014, MNRAS, 444, 3230  
 Barnes, S. A. 2007, ApJ, 669, 1167  
 Barrado, D., Bouy, H., Bouvier, J., et al. 2016, A&A, 596,  
 Barrado y Navascués, D., Bouvier, J., Stauffer, J. R., Lodieu, N., & McCaughrean, M. J. 2002, A&A, 395, 813  
 Barrado y Navascués, D., Stauffer, J. R., Briceño, C., et al. 2001, ApJS, 134, 103  
 Barrado y Navascués, D., Stauffer, J. R., & Jayawardhana, R. 2004, ApJ, 614, 386  
 Barrado y Navascués, D., Stauffer, J. R., & Patten, B. M. 1999a, ApJ, 522,  
 Barrado y Navascués, D., Stauffer, J. R., Song, I., & Caillault, J. P. 1999b, ApJ, 520,  
 Basri, G., Marcy, G. W., & Graham, J. R. 1996, Astrophysical Journal v.458, p.600, 458, 600  
 Basri, G., & Martín, E. L. 1999a, ApJ, 510, 266  
 Basri, G., & Martín, E. L. 1999b, AJ, 118, 2460  
 Bayo, A., Barrado, D., Allard, F., et al. 2017, MNRAS, 465, 760  
 Bayo, A., Barrado, D., Stauffer, J., et al. 2011, Astronomy & Astrophysics, Volume 536, id.A63, 23 pp., 536, 63  
 Bayo, A., Rodrigo, C., Barrado Y Navascués, D., et al. 2008, A&A, 492, 277  
 Bell, C. P. M., Mamajek, E. E., & Naylor, T. 2015, MNRAS, 454, 593  
 Bell, C. P. M., Murphy, S. J., & Mamajek, E. E. 2017, MNRAS, 468, 1198  
 Bell, C. P. M., Naylor, T., Mayne, N. J., Jeffries, R. D., & Littlefair, S. P. 2013, MNRAS, 434, 806  
 Bell, C. P. M., Rees, J. M., Naylor, T., et al. 2014, MNRAS, 445, 3496  
 Berger, E. 2006, ApJ, 648, 629  
 Bergfors, C., Brandner, W., Janson, M., et al. 2010, A&A, 520,  
 Beuzit, J. L., Ségransan, D., Forveille, T., et al. 2004, A&A, 425, 997  
 Bianchi, L. & Team, G. A. L. E. X. 2000, Mem. Soc. Astron. Italiana, 71, 1123  
 Bildsten, L., Brown, E. F., Matzner, C. D., & Ushomirsky, G. 1997, ApJ, 482, 442  
 Binks, A. S. & Jeffries, R. D. 2014, MNRAS, 438,  
 Binks, A. S. & Jeffries, R. D. 2016, MNRAS, 455, 3345  
 Blaauw, A. 1946, PhD thesis, -  
 Blaauw, A. 1964, ARA&A, 2, 213  
 Boesgaard, A. M. & Friel, E. D. 1990, ApJ, 351, 467

## References

- Abia, C., Cabezon, R. M., & Domínguez, I. 2020, Mem. Soc. Astron. Italiana, 91, 48  
 Alam, S., Albareti, F. D., Allende Prieto, C., et al. 2015, ApJS, 219, 12  
 Alcalá, J. M., Covino, E., Torres, G., et al. 2000, A&A, 353, 186  
 Alexander, D. R., Johnson, H. R., & Rypma, R. L. 1983, ApJ, 272, 773  
 Allard, F., Homeier, D., Freytag, B., et al. 2013, Memorie della Società Astronomica Italiana Supplementi, 24, 128  
 Allard, F., Homeier, D., Freytag, B., & Sharp, C. M. 2012, in EAS Publications Series, Vol. 57, EAS Publications Series, ed. C. Reylé, C. Charbonnel, & M. Schultheis, 3–43  
 Ambartsumian, V. A. 1947, The evolution of stars and astrophysics  
 Ambartsumian, V. A. 1949, AZh, 26, 3  
 Amelin, Y., Krot, A. N., Hutcheon, I. D., & Ulyanov, A. A. 2002, Science, 297, 1678  
 Anders, E. & Grevesse, N. 1989, Geochim. Cosmochim. Acta, 53, 197

**Table 6.** Properties of the Lithium Depletion Boundary for the 12 stellar associations.

Stellar association	Summary of the LDB data				
	$L_{\text{bol}} \text{ LDB}$ $10^{-3} [L_{\odot}]$	$T_{\text{eff}} \text{ LDB}$ [K]	$d_{\text{mode}}$ [pc]	$E(B - V)$ [mag]	LDB age [Ma]
Alpha Persei	$2.98^{+0.35}_{-0.19}$	2 857	174	0.090	$79.0^{+1.5}_{-2.3}$
NGC 1960	$23.6^{+12}_{-4.9}$	3 123	1 207	0.200	$31.6^{+3.9}_{-4.7}$
IC 4665	$23.6^{+2.1}_{-1.6}$	3 110	347	0.170	$31.6^{+1.3}_{-1.6}$
NGC 2547	$11.13^{+2.4}_{-0.89}$	3 004	397	0.040	$43.5^{+1.7}_{-4.0}$
IC 2602	$7.14^{+1.2}_{-0.52}$	2 926	152	0.031	$52.5^{+2.2}_{-3.7}$
IC 2391	$5.93^{+0.35}_{-0.19}$	2 956	152	0.030	$57.7^{+0.5}_{-1.0}$
The Pleiades	$1.321^{+0.19}_{-0.089}$	2 728	136	0.045	$127.4^{+6.3}_{-10}$
Blanco 1	$1.182^{+0.069}_{-0.099}$	2 746	239	0.010	$137.1^{+7.0}_{-33}$
The Hyades	$0.124^{+0.019}_{-0.016}$	2 021	47	0.001	$695^{+85}_{-67}$
BPMG	$43.61^{+0.90}_{-0.81}$	3 095	9 - 73	0.000	$24.3^{+0.3}_{-0.3}$
THMG	$7.486^{+0.054}_{-0.11}$	2 935	36 - 71	0.000	$51.0^{+0.5}_{-0.2}$
32 Ori MG	$41.3^{+2.4}_{-2.1}$	3 135	70 - 100	0.030	$25.0^{+0.7}_{-0.8}$
32 Ori MG-P1	$41.8^{+4.8}_{-15}$	3 106		0.030	$24.9^{+4.8}_{-1.5}$
32 Ori MG-P2	$30^{+9}_{-8}$	3 106		0.030	$28.6^{+0.3}_{-2.9}$
Theia 133	$39^{+18}_{-17}$	3 139	112	0.030	$25.6^{+7.0}_{-5.5}$
Theia 370	$29.8^{+8.3}_{-8.4}$	3 087	97	0.030	$28.7^{+4.7}_{-2.6}$

**Note:** The ‘LDB age’ was derived using the BT-Settl models, see Table 3.

- Bonnarel, F., Fernique, P., Bienaymé, O., et al. 2000, A&AS, 143, 33  
 Bossini, D., Vallenari, A., Bragaglia, A., et al. 2019, A&A, 623,  
 Boudreault, S. & Bailer-Jones, C. A. L. 2009, ApJ, 706, 1484  
 Bouvier, J., Barrado, D., Moraux, E., et al. 2018, A&A, 613,  
 Bouvier, J., Kendall, T., Meeus, G., et al. 2008, A&A, 481, 661  
 Bouvier, J., Stauffer, J. R., Martin, E. L., et al. 1998, A&A, 336, 490  
 Bouy, H., Bertin, E., Sarro, L. M., et al. 2015, A&A, 577,  
 Bouy, H., Moraux, E., Bouvier, J., et al. 2006, ApJ, 637, 1056  
 Brandt, T. D. & Huang, C. X. 2015, ApJ, 807, 24  
 Breger, M. 1986, ApJ, 309, 311  
 Brown, A. G. A., Arenou, F., van Leeuwen, F., Lindegren, L., & Luri, X. 1997a,  
     in ESA Special Publication, Vol. 402, Hipparcos - Venice '97, ed. R. M. Bon-  
     net, E. Høg, P. L. Bernacca, L. Emiliani, A. Blaauw, C. Turon, J. Kovalevsky,  
     L. Lindegren, H. Hassan, M. Bouffard, B. Strim, D. Heger, M. A. C. Perry-  
     man, & L. Woltjer, 63–68  
 Brown, A. G. A., Dekker, G., & de Zeeuw, P. T. 1997b, MNRAS, 285, 479  
 Burke, C. J., Pinsonneault, M. H., & Sills, A. 2004, ApJ, 604, 272  
 Burrows, A., Hubbard, W. B., Saumon, D., & Lunine, J. I. 1993, ApJ, 406, 158  
 Burrows, A., Marley, M., Hubbard, W. B., et al. 1997, ApJ, 491, 856  
 Cantat-Gaudin, T., Jordi, C., Vallenari, A., et al. 2018a, A&A, 618,  
 Cantat-Gaudin, T., Vallenari, A., Sordo, R., et al. 2018b, A&A, 615,  
 Canuto, V. M., & Mazzitelli, I. 1991, ApJ, 370, 295  
 Cargile, P. A. & James, D. J. 2010, AJ, 140, 677  
 Cargile, P. A., James, D. J., & Jeffries, R. D. 2010, ApJ, 725,  
 Cargile, P. A., James, D. J., Pepper, J., et al. 2014, ApJ, 782, 29  
 Cargile, P. A., James, D. J., & Platais, I. 2009, AJ, 137, 3230  
 Castelli, F., Gratton, R. G., & Kurucz, R. L. 1997, A&A, 318, 841  
 Chabrier, G., Gallardo, J., & Baraffe, I. 2007, A&A, 472,  
 Chambers, K. C. e. a. 2017, VizieR Online Data Catalog,  
 Cifuentes, C., Caballero, J. A., Cortés-Contreras, M., et al. 2020, A&A, 642,  
 Claria, J. J. 1982, A&AS, 47, 323  
 Cutri, R. M. 2013, VizieR Online Data Catalog, 2328  
 Cutri, R. M., Skrutskie, M. F., van Dyk, S., et al. 2003, VizieR Online Data  
     Catalog, 2246, 0  
 da Silva, L., Torres, C. A. O., de La Reza, R., et al. 2009, A&A, 508, 833  
 Dahm, S. E. 2015, ApJ, 813, 108  
 Damiani, F., Prisinzano, L., Micela, G., et al. 2014, A&A, 566,  
 D'Antona, F. & Mazzitelli, I. 1984, A&A, 138, 431  
 D'Antona, F. & Mazzitelli, I. 1994, ApJS, 90, 467  
 D'Antona, F. & Mazzitelli, I. 1997, Mem. Soc. Astron. Italiana, 68, 807  
 D'Antona, F., Ventura, P., & Mazzitelli, I. 2000, ApJ, 543,  
 David, T. J. & Hillenbrand, L. A. 2015, ApJ, 804, 146  
 de Bruijne, J. H. J., Hoogerwerf, R., & de Zeeuw, P. T. 2001, A&A, 367, 111  
 De Gennaro, S., von Hippel, T., Jefferys, W. H., et al. 2009, ApJ, 696, 12  
 de Wit, W. J., Bouvier, J., Palla, F., et al. 2006, A&A, 448, 189  
 Deacon, N. R. & Hambley, N. C. 2004, A&A, 416, 125  
 DENIS Consortium, 2005, VizieR Online Data Catalog, 2263, 0  
 Dias, W. S., Alessi, B. S., Moitinho, A., & Lépine, J. R. D. 2002, A&A, 389, 871  
 Dobbie, P. D., Lodieu, N., & Sharp, R. G. 2010, MNRAS, 409, 1002  
 D'Orazi, V. & Randich, S. 2009, A&A, 501, 553  
 Drew, J. E., Gonzalez-Solares, E., Greimel, R., et al. 2016, VizieR Online Data  
     Catalog, 2341  
 Ducourant, C., Teixeira, R., Périé, J. P., et al. 2005, A&A, 438, 769  
 Edvardsson, B., Pettersson, B., Kharrazi, M., & Westerlund, B. 1995, A&A, 293,  
     75  
 Eggen, O. J. 1986, AJ, 92, 1074  
 Eggen, O. J. 1998, AJ, 116, 284  
 Egret, D., Wenger, M., & Dubois, P. 1991, in Astrophysics and Space Science  
     Library, Vol. 171, Databases and On-line Data in Astronomy, ed. M. A. Al-  
     brecht & D. Egret, 79–88  
 Elliott, P., Bayo, A., Melo, C. H. F., et al. 2014, A&A, 568,  
 Evans, D. W., Irwin, M. J., & Helmi, L. 2002, A&A, 395, 347  
 Evans, D. W., Riello, M., De Angeli, F., et al. 2018, A&A, 616,  
 Ford, A., Jeffries, R. D., & Smalley, B. 2005, MNRAS, 364, 272  
 Franciosini, E., Tognelli, E., Degl'Innocenti, S., et al. 2022, A&A, 659,  
 Gagné, J., Lafrenière, D., Doyon, R., Malo, L., & Artigau, É. 2015, ApJ, 798, 73  
 Gaia Collaboration, Brown, A. G. A., Vallenari, A., Prusti, T., et al. 2018a, As-  
     tronomy & Astrophysics, Volume 616, id.A1, 22 pp., 616, A1

- Gaia Collaboration, Brown, A. G. A., Vallenari, A., Prusti, T., et al. 2021, *A&A*, 649,
- Gaia Collaboration, Babusiaux, C., van Leeuwen, F., Barstow, M. A., et al. 2018b, *A&A*, 616,
- Gaia Collaboration, Prusti, T., de Bruijne, J. H. J., Brown, A. G. A., et al. 2016, *A&A*, 595,
- Galli, P. A. B., Moraux, E., Bouy, H., et al. 2017, *A&A*, 598,
- Gebran, M. & Monier, R. 2008, *A&A*, 483, 567
- Gebran, M., Vick, M., Monier, R., & Fossati, L. 2010, *A&A*, 523,
- Giampapa, M. S., Prosser, C. F., & Fleming, T. A. 1998, *ApJ*, 501, 624
- Gibson, S. J. & Nordsieck, K. H. 2003a, *ApJ*, 589, 347
- Gibson, S. J. & Nordsieck, K. H. 2003b, *ApJ*, 589, 362
- Gilmore, G., Randich, S., Asplund, M., et al. 2012, *The Messenger*, 147, 25
- Gorlova, N., Balog, Z., Rieke, G. H., et al. 2007, *ApJ*, 670, 516
- Gustafsson, B., Edvardsson, B., Eriksson, K., et al. 2008, *A&A*, 486, 951
- Hambly, N. C., Hawkins, M. R. S., & Jameson, R. F. 1993, *A&AS*, 100, 607
- Henden, A. A., Welch, D. L., Terrell, D., & Levine, S. E. 2009, in *American Astronomical Society Meeting Abstracts*, Vol. 214, American Astronomical Society Meeting Abstracts, 214, –407
- Høg, E., Fabricius, C., Makarov, V. V., et al. 2000, *A&A*, 355,
- Hogan, E., Jameson, R. F., Casewell, S. L., Osbourne, S. L., & Hambly, N. C. 2008, *MNRAS*, 388, 495
- Indebetouw, R., Mathis, J. S., Babler, B. L., et al. 2005, *ApJ*, 619, 931
- Israelian, G., Santos, N. C., Mayor, M., & Rebolo, R. 2001, *Nature*, 411, 163
- Jackson, R. J., Deliyannis, C. P., & Jeffries, R. D. 2018, *Monthly Notices of the Royal Astronomical Society*, 476, 3245
- Jackson, R. J. & Jeffries, R. D. 2014a, *MNRAS*, 445, 4306
- Jackson, R. J. & Jeffries, R. D. 2014b, *MNRAS*, 441, 2111
- Janson, M., Durkan, S., Hippler, S., et al. 2017, *A&A*, 599,
- Janson, M., Hormuth, F., Bergfors, C., et al. 2012, *ApJ*, 754, 44
- Jeffries, R. D., Jackson, R. J., James, D. J., & Cargile, P. A. 2009, *MNRAS*, 400, 317
- Jeffries, R. D. & Naylor, T. 2001, in *Astronomical Society of the Pacific Conference Series*, Vol. 243, From Darkness to Light: Origin and Evolution of Young Stellar Clusters, ed. T. Montmerle & P. André, 633
- Jeffries, R. D., Naylor, T., Devey, C. R., & Totten, E. J. 2004, *MNRAS*, 351, 1401
- Jeffries, R. D., Naylor, T., Mayne, N. J., Bell, C. P. M., & Littlefair, S. P. 2013, *MNRAS*, 434, 2438
- Jeffries, R. D. & Oliveira, J. M. 2005, *MNRAS*, 358, 13
- Jeffries, R. D. & Tolley, A. J. 1998, *MNRAS*, 300, 331
- Juarez, A. J., Cargile, P. A., James, D. J., & Stassun, K. G. 2014, *ApJ*, 795, 143
- Kaiser, B. C., Clemens, J. C., Blouin, S., et al. 2021, *Science*, 371, 168
- Kounkel, M. & Covey, K. 2019, *AJ*, 158, 122
- Kraus, A. L., Shkolnik, E. L., Allers, K. N., & Liu, M. C. 2014, *AJ*, 147, 146
- Lawrence, A., Warren, S. J., Almaini, O., et al. 2007, *MNRAS*, 379, 1599
- Lawson, W. A., Lyo, A. R., & Bessell, M. S. 2009, *MNRAS*, 400,
- Lindgren, L., Hernández, J., Bombrun, A., et al. 2018, *A&A*, 616,
- Lindgren, L., Lammers, U., Bastian, U., et al. 2016, *A&A*, 595,
- Lodie, N., Boudreault, S., & Béjar, V. J. S. 2014, *MNRAS*, 445, 3908
- Lodie, N., Pérez-Garrido, A., Smart, R. L., & Silvotti, R. 2019a, *A&A*, 628,
- Lodie, N., Rebolo, R., & Pérez-Garrido, A. 2018, *A&A*, 615,
- Lodie, N., Smart, R. L., Pérez-Garrido, A., & Silvotti, R. 2019b, *A&A*, 623,
- López-Morales, M. 2007, *ApJ*, 660, 732
- Luri, X., Brown, A. G. A., Sarro, L. M., et al. 2018, *A&A*, 616,
- Lyra, W., Moitinho, A., van der Bliek, N. S., & Alves, J. 2006, *A&A*, 453, 101
- Macdonald, J. & Mullan, D. J. 2010, *ApJ*, 723, 1599
- Maeder, A. 1971, *A&A*, 10, 354
- Maíz Apellániz, J. 2005, in *ESA Special Publication*, Vol. 576, The Three-Dimensional Universe with Gaia, ed. C. Turon, K. S. O’Flaherty, & M. A. C. Perryman, 179
- Maíz Apellániz, J. & Weiler, M. 2018, *A&A*, 619,
- Makarov, V. V. 2006, *AJ*, 131, 2967
- Makarov, V. V. 2007, *ApJS*, 169, 105
- Malo, L., Artigau, É., Doyon, R., et al. 2014a, *ApJ*, 788, 81
- Malo, L., Doyon, R., Feiden, G. A., et al. 2014b, *ApJ*, 792, 37
- Malo, L., Doyon, R., Lafrenière, D., et al. 2013, *ApJ*, 762, 88
- Mamajek, E. E. 2007, in *IAU Symposium*, Vol. 237, Triggered Star Formation in a Turbulent ISM, ed. B. G. Elmegreen & J. Palous, 442–442
- Mamajek, E. E. & Bell, C. P. M. 2014, *MNRAS*, 445, 2169
- Manzi, S., Randich, S., de Wit, W. J., & Palla, F. 2008, *A&A*, 479, 141
- Marcy, G. W., Basri, G., & Graham, J. R. 1994, *ApJ*, 428,
- Martín, E. L., Barrado y Navascués, D., Baraffe, I., Bouy, H., & Dahm, S. 2003, *ApJ*, 594, 525
- Martín, E. L., Basri, G., Brandner, W., et al. 1998, *ApJ*, 509,
- Martín, E. L., Brandner, W., Bouvier, J., et al. 2000, *ApJ*, 543, 299
- Martín, E. L., Lodieu, N., & Béjar, V. J. S. 2020, *A&A*, 640,
- Martín, E. L., Lodieu, N., Pavlenko, Y., & Béjar, V. J. S. 2018, *ApJ*, 856, 40
- Mason, B. D., Hartkopf, W. I., Miles, K. N., et al. 2018, *AJ*, 155, 215
- Mason, B. D., Wycoff, G. L., Hartkopf, W. I., Douglass, G. G., & Worley, C. E. 2001, *AJ*, 122, 3466
- Mayne, N. J. & Naylor, T. 2008, *MNRAS*, 386, 261
- Mazzei, P. & Pigatto, L. 1989, *A&A*, 213,
- Meingast, S. & Alves, J. 2019, *A&A*, 621,
- Meingast, S., Alves, J., & Rottensteiner, A. 2021, *A&A*, 645,
- Melis, C., Reid, M. J., Mioduszewski, A. J., Stauffer, J. R., & Bower, G. C. 2014, *Science*, 345, 1029
- Mentuch, E., Brandeker, A., van Kerkwijk, M. H., Jayawardhana, R., & Hauschildt, P. H. 2008, *ApJ*, 689, 1127
- Mermilliod, J. C. 1981, *A&A*, 97, 235
- Mermilliod, J. C. 2000, in *Astronomical Society of the Pacific Conference Series*, Vol. 198, Stellar Clusters and Associations: Convection, Rotation, and Dynamos, ed. R. Pallavicini, G. Micela, & S. Sciotino, 105
- Mermilliod, J. C., Queloz, D., & Mayor, M. 2008, *A&A*, 488, 409
- Messina, S., Lanzafame, A. C., Feiden, G. A., et al. 2016, *A&A*, 596,
- Messina, S., Millward, M., Buccino, A., et al. 2017, *A&A*, 600,
- Meynet, G. & Maeder, A. 2000, *A&A*, 361, 101
- Meynet, G., Mermilliod, J. C., & Maeder, A. 1993, *A&AS*, 98, 477
- Miret-Roig, N., Antoja, T., Romero-Gómez, M., & Figueiras, F. 2018, *A&A*, 615,
- Miret-Roig, N., Galli, P. A. B., Brandner, W., et al. 2020, *A&A*, 642,
- Moraux, E. 2016, in *EAS Publications Series*, Vol. 80–81, *EAS Publications Series*, 73–114
- Moraux, E., Bouvier, J., Stauffer, J. R., Barrado y Navascués, D., & Cuillandre, J. C. 2007, *A&A*, 471, 499
- Murphy, S. J., Lawson, W. A., Onken, C. A., et al. 2020, *MNRAS*, 491, 4902, stz3198
- Murray, S. S., Brugel, E. W., Eichhorn, G., et al. 1992, in *European Southern Observatory Conference and Workshop Proceedings*, Vol. 43, European Southern Observatory Conference and Workshop Proceedings, ed. A. Heck & F. Murtagh
- Naylor, T. 2009, *MNRAS*, 399, 432
- Naylor, T. & Jeffries, R. D. 2006, *MNRAS*, 373, 1251
- Naylor, T., Totten, E. J., Jeffries, R. D., et al. 2002, *MNRAS*, 335, 291
- Netopil, M., Paunzen, E., Heiter, U., & Soubiran, C. 2016, *A&A*, 585,
- Nikiforova, V. V., Kulesh, M. V., Sleznev, A. F., & Carraro, G. 2020, *AJ*, 160, 142
- Ochsenbein, F., Bauer, P., & Marcout, J. 2000, *A&AS*, 143, 23
- Olivares, J., Sarro, L. M., Bouy, H., et al. 2020, *A&A*, 644,
- Olivares, J., Sarro, L. M., Moraux, E., et al. 2018, *A&A*, 617,
- Oliveira, J. M., Jeffries, R. D., Devey, C. R., et al. 2003, *MNRAS*, 342, 651
- Oppenheimer, B. R., Basri, G., Nakajima, T., & Kulkarni, S. R. 1997, *AJ*, 113, 296
- Ortega, V. G., de la Reza, R., Jilinski, E., & Bazzanella, B. 2002, *ApJ*, 575,
- Panagi, P. M. & O’dell, M. A. 1997, *A&AS*, 121, 213
- Patten, B. M. & Pavlovsky, C. M. 1999, *PASP*, 111, 210
- Patterson, C. 1956, *Geochimica et Cosmochimica Acta*, 10, 230
- Pedregosa, F., Varoquaux, G., Gramfort, A., et al. 2011, *Journal of Machine Learning Research*, 12, 2825
- Pérez-Garrido, A., Lodieu, N., & Rebolo, R. 2017, *A&A*, 599,
- Perryman, M. A. C., Brown, A. G. A., Lebreton, Y., et al. 1998, *A&A*, 331, 81
- Pinsonneault, M. H., Stauffer, J., Soderblom, D. R., King, J. R., & Hanson, R. B. 1998, *ApJ*, 504, 170
- Planck Collaboration, , Aghanim, N., Akrami, Y., et al. 2020, *A&A*, 641,
- Pöhl, H. & Paunzen, E. 2010, *A&A*, 514,
- Prosser, C. F. 1992, *AJ*, 103, 488
- Prosser, C. F. 1993, *AJ*, 105, 1441
- Prosser, C. F. 1994, *AJ*, 107, 1422
- Queiroz, A. B. A., Anders, F., Santiago, B. X., et al. 2018, *MNRAS*, 476, 2556
- Randich, S., Pallavicini, R., Meola, G., Stauffer, J. R., & Balachandran, S. C. 2001, *A&A*, 372, 862
- Randich, S., Tognelli, E., Jackson, R., et al. 2018, *A&A*, 612,
- Rebolo, R., Martin, E. L., Basri, G., Marcy, G. W., & Zapatero-Osorio, M. R. 1996, *ApJ*, 469,
- Rebolo, R., Martin, E. L., & Magazzù, A. 1992, *ApJ*, 389,
- Reid, I. N. & Hawley, S. L. 2005, New light on dark stars : red dwarfs, low-mass stars, brown dwarfs, 2nd edn., *Astronomy and Planetary Sciences* (Springer-Verlag Berlin Heidelberg)
- Reiners, A. 2012, *Living Reviews in Solar Physics*, 9, 1
- Ribas, I., Morales, J. C., Jordi, C., et al. 2008, *Mem. Soc. Astron. Italiana*, 79, 562
- Röser, S., Schilbach, E., & Goldman, B. 2019, *A&A*, 621,
- Sanner, J., Altmann, M., Brunzendorf, J., & Geffert, M. 2000, *A&A*, 357, 471
- Schneider, A. C. & Shkolnik, E. L. 2018, *AJ*, 155, 122
- Scholz, A., Froebrich, D., Muzic, K., & Eisloffel, J. 2020, *The Open Journal of Astrophysics*, 3, 8
- Sharma, S., Pandey, A. K., Ogura, K., et al. 2006, *AJ*, 132, 1669
- Shkolnik, E., Liu, M. C., & Reid, I. N. 2009, *ApJ*, 699, 649
- Shkolnik, E. L., Allers, K. N., Kraus, A. L., Liu, M. C., & Flagg, L. 2017, *AJ*, 154, 69

- Siess, L., Dufour, E., & Forestini, M. 2000, A&A, 358, 593  
 Skinner, J., Covey, K. R., Bender, C. F., et al. 2018, AJ, 156, 45  
 Skrutskie, M. F., Cutri, R. M., Stiening, R., et al. 2006, AJ, 131, 1163  
 Smart, R. L., Marocco, F., Sarro, L. M., et al. 2019, MNRAS, 485, 4423  
 Soderblom, D. R. 2010, ARA&A, 48, 581  
 Soderblom, D. R., Jones, B. F., Balachandran, S., et al. 1993, AJ, 106, 1059  
 Solano, E., Gálvez-Ortiz, M. C., Martín, E. L., et al. 2021, MNRAS, 501, 281  
 Solano, E., Martín, E. L., Caballero, J. A., et al. 2019, A&A, 627,  
 Somers, G. & Pinsonneault, M. H. 2014, ApJ, 790, 72  
 Song, I. 2016, in Young Stars & Planets Near the Sun, ed. J. H. Kastner,  
     B. Stelzer, & S. A. Metchev, Vol. 314, 95–98  
 Song, I., Bessell, M. S., & Zuckerman, B. 2002, ApJ, 581,  
 Song, I., Caillault, J. P., Barrado y Navascués, D., & Stauffer, J. R. 2001, ApJ,  
     546, 352  
 Song, I., Zuckerman, B., & Bessell, M. S. 2003, ApJ, 599, 342  
 Southworth, J., Maxted, P. F. L., & Smalley, B. 2005, A&A, 429, 645  
 Stahler, S. W. & Palla, F. 2005, The Formation of Stars, ed. Wiley-VCH, Physics  
     textbooks (Wiley-VCH)  
 Stauffer, J., Barrado, D., David, T., et al. 2020, AJ, 160, 30  
 Stauffer, J. R., Barrado y Navascués, D., Bouvier, J., et al. 1999, ApJ, 527, 219  
 Stauffer, J. R., Hamilton, D., & Probst, R. G. 1994, AJ, 108, 155  
 Stauffer, J. R. & Hartmann, L. W. 1987, ApJ, 318, 337  
 Stauffer, J. R., Hartmann, L. W., & Barrado y Navascués, D. 1995a, ApJ, 454,  
     910  
 Stauffer, J. R., Hartmann, L. W., Fazio, G. G., et al. 2007, ApJS, 172, 663  
 Stauffer, J. R., Hartmann, L. W., Prosser, C. F., et al. 1997, ApJ, 479, 776  
 Stauffer, J. R., Jones, B. F., Backman, D., et al. 2003, AJ, 126, 833  
 Stauffer, J. R., Liebert, J., & Giampapa, M. 1995b, AJ, 109, 298  
 Stauffer, J. R., Schild, R., Barrado y Navascués, D., et al. 1998a, ApJ, 504, 805  
 Stauffer, J. R., Schultz, G., & Kirkpatrick, J. D. 1998b, ApJ, 499,  
 Steele, I. A., Jameson, R. F., & Hambley, N. C. 1993, MNRAS, 263, 647  
 Stelzer, B. & Neuhäuser, R. 2000, A&A, 361, 581  
 Taylor, M. B. 2005, in Astronomical Society of the Pacific Conference Se-  
     ries, Vol. 347, Astronomical Data Analysis Software and Systems XIV, ed.  
     P. Shopbell, M. Britton, & R. Ebert, 29  
 Taylor, M. B. 2006, in Astronomical Society of the Pacific Conference Se-  
     ries, Vol. 351, Astronomical Data Analysis Software and Systems XV, ed.  
     C. Gabriel, C. Arviset, D. Ponz, & S. Enrique, 666  
 Tognelli, E., Prada Moroni, P. G., & Degl'Innocenti, S. 2011, A&A, 533,  
 Tognelli, E., Prada Moroni, P. G., & Degl'Innocenti, S. 2015, MNRAS, 449,  
     3741  
 Torres, C. A. O., da Silva, L., Quast, G. R., de la Reza, R., & Jilinski, E. 2000,  
     AJ, 120, 1410  
 Torres, C. A. O., Quast, G. R., da Silva, L., et al. 2006, A&A, 460, 695  
 Torres, C. A. O., Quast, G. R., Melo, C. H. F., & Sterzik, M. F. 2008, Mono-  
     graph Publications, Vol. 5, Handbook of Star Forming Regions: Volume II,  
     The Southern Sky, ed. B. Reipurth (Astronomical Society of the Pacific Pub-  
     lications), 757  
 Ushomirsky, G., Matzner, C. D., Brown, E. F., et al. 1998, ApJ, 497, 253  
 van Leeuwen, F. 2009, A&A, 497, 209  
 van Leeuwen, F. & Hansen Ruiz, C. S. 1997, in ESA Special Publication, Vol.  
     402, Hipparcos - Venice '97, ed. R. M. Bonnet, E. Høg, P. L. Bernacca,  
     L. Emiliani, A. Blaauw, C. Turon, J. Kovalevsky, L. Lindegren, H. Hassan,  
     M. Bouffard, B. Strim, D. Heger, M. A. C. Perryman, & L. Woltjer, 689–692  
 Viana Almeida, P., Santos, N. C., Melo, C., et al. 2009, A&A, 501, 965  
 Westerlund, B. E., Garnier, R., Lundgren, K., Pettersson, B., & Breysacher, J.  
     1988, A&AS, 76, 101  
 Yee, J. C. & Jensen, E. L. N. 2010, ApJ, 711, 303  
 Zapatero Osorio, M. R., Rebolo, R., Martin, E. L., & Garcia Lopez, R. J. 1996,  
     A&A, 305, 519  
 Zapatero Osorio, M. R., Rebolo, R., Martín, E. L., et al. 1999, A&AS, 134, 537  
 Zuckerman, B. & Song, I. 2004, ARA&A, 42, 685  
 Zuckerman, B., Song, I., Bessell, M. S., & Webb, R. A. 2001, ApJ, 562,  
 Zuckerman, B. & Webb, R. A. 2000, ApJ, 535, 959

## **Appendix A: Parallaxes distributions, VPDs, and HRDs for all the stellar associations**

In this appendix, we present the parallax distributions the VPDs and the HRDs for all the stellar associations. In some cases, we studied different possibilities of locating the LDB and for these, we present different HRDs, that is, a different one for each location.

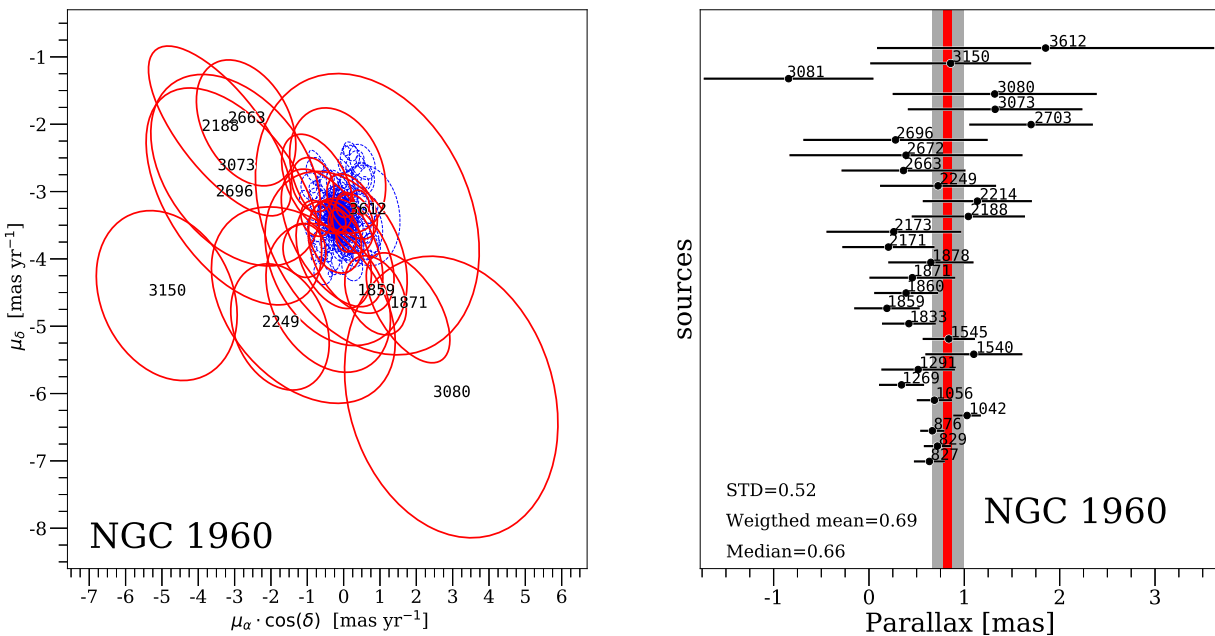


**Fig. A.1.** VPD and parallaxes for NGC 1960. **Left:** VPD, for NGC 1960. Blue dashed ellipses are the members taken from Cantat-Gaudin et al. 2018a; red ellipses are our LDB sample. The rest is the same as in Fig. 2 but for NGC 1960. **Right:** Same as in Fig. 3 but for NGC 1960.

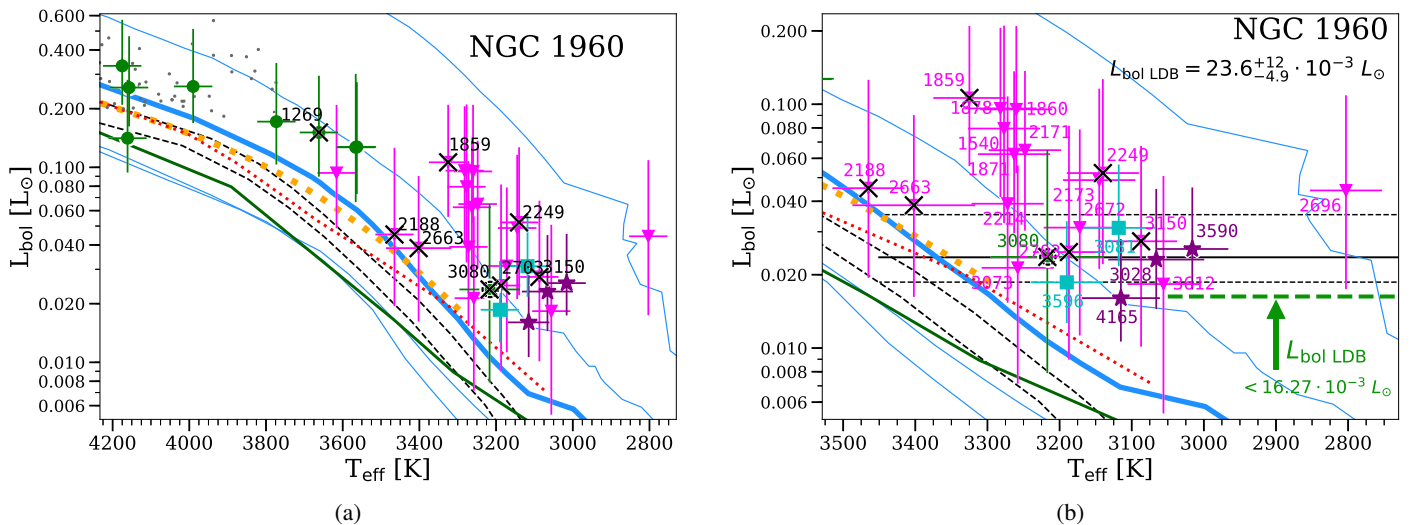


**Fig. A.2.** HRDs and the LDB for NGC 1960. **Left:** Same as Fig. 5. Cyan squares are lithium-rich sources without *Gaia* DR2 parallaxes and purple stars are lithium upper limits or lithium-poor sources without *Gaia* DR2 parallaxes, both from our LDB sample (see Section 4.2); empty large black circles are confirmed multiple systems and broken lines are suspected multiple systems; over-imposed big black crosses are sources discarded as members after this work. Moreover, grey points are known members from Cantat-Gaudin et al. (2018a). Thin blue lines correspond to isochrones of 1, 10, 100 Ma, and 1 Ga from the BT-Settl models (Allard et al. 2013), while the thick blue one corresponds to 30 Ma. The figure includes: a 20 Ma and a 30 Ma isochrone from D'Antona & Mazzitelli 1994 (black dashed line), a 25 Ma isochrone from Tognelli et al. 2011 (orange dashed dot line), a 30 Ma isochrone from Siess et al. 2000 (red dotted line) and a Zero Age Main Sequence from Stahler & Palla 2005 (green solid line). **Right:** Zoom on the left plot. A black horizontal line marks the  $L_{\text{bol LDB}}$ , together with the 16th and 84th percentiles (dotted lines). NGC 1960 is  $31.6^{+3.9}_{-4.7}$  Ma old using the BT-Settl bolometric luminosity-age relationship (Allard et al. 2012). An extensive dashed horizontal green line indicates a possible LDB upper limit (see Section 5.2).

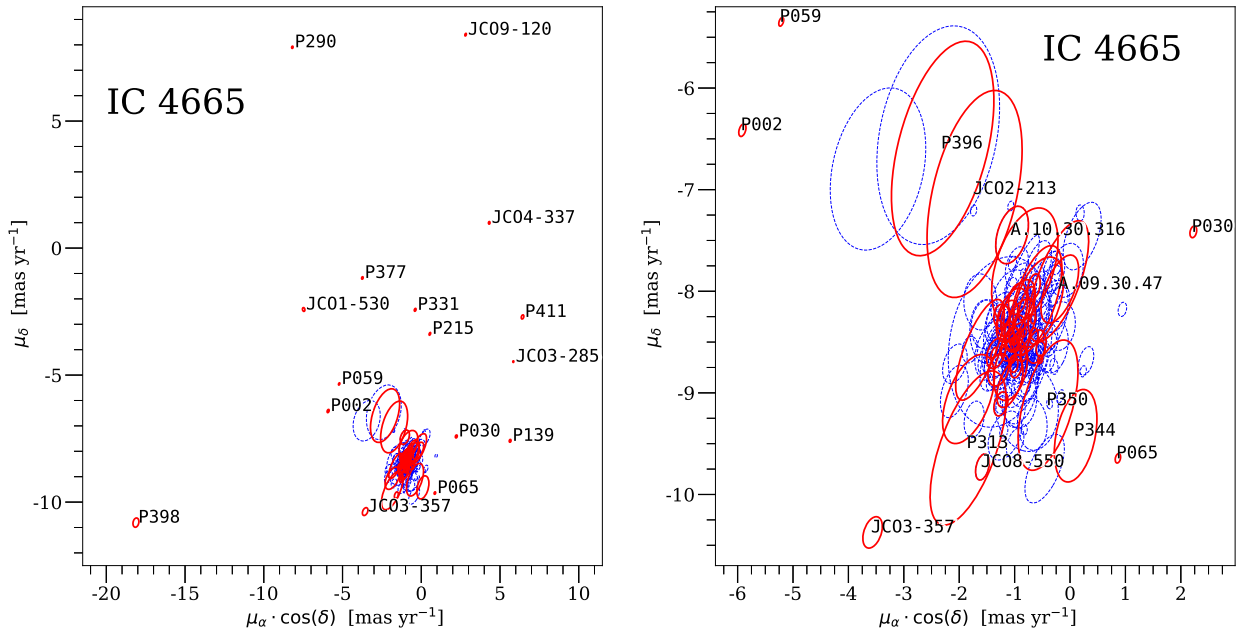


**Fig. A.3.** VPD for IC 4665. **Left:** Details are the same as in Fig. 2 but for IC 4665. **Right:** Zoom on the left figure.

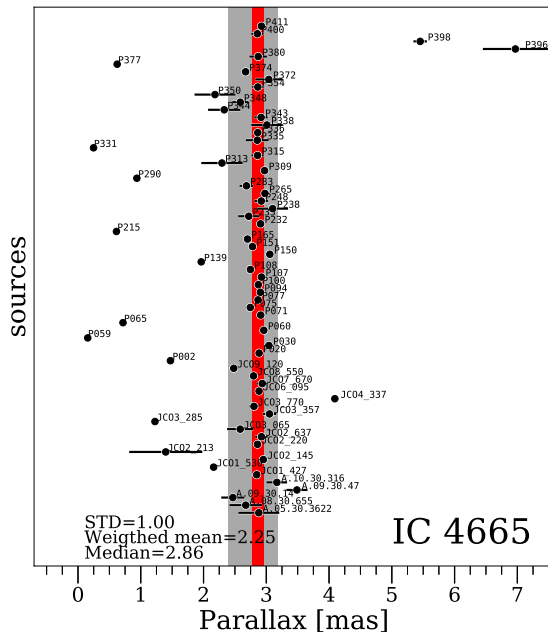


**Fig. A.4.** Parallaxes for IC 4665 members close to the LDB. Details are the same as in Fig. 3 but for IC 4665.

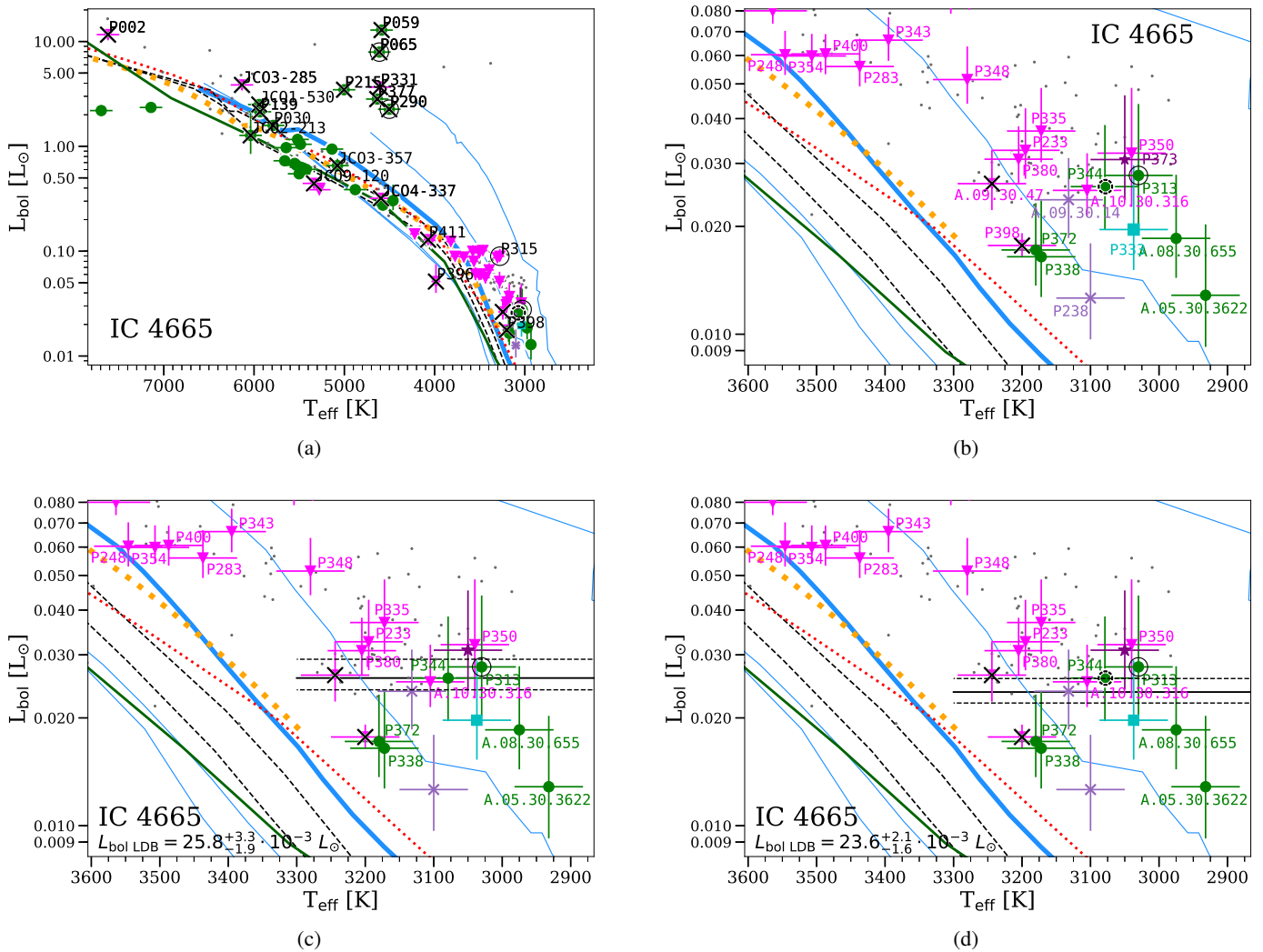


**Fig. A.5.** HRDs and the LDB for IC 4665. (a) the same as in Figs. 5 and A.2 but for IC 4665. The violet crosses are sources with undetected or dubious lithium detections due to their low resolution spectrum or other technical disabilities. Thin blue lines correspond to isochrones of 1, 10, 100 Ma, and 1 Ga from the BT-Settl models (Allard et al. 2013), while the thick blue one to 30 Ma. The figure includes: a 20 Ma and a 30 Ma isochrone from D'Antona & Mazzitelli 1994 (black dashed lines), a 25 Ma isochrone from Tognelli et al. 2011 (orange dashed dot line), a 30 Ma isochrone from Siess et al. 2000 (red dotted line). (b) Zoom on the previous plot around the LDB with all the source names. (c) A black horizontal line marks the  $L_{\text{bol}} \text{ LDB}$ , together with the 16th and 84th percentiles (dashed lines), following the first scenario, see Section 2.3. (d) Same as (b), but the the  $L_{\text{bol}} \text{ LDB}$  is located following the second scenario, see Section 2.3. It is  $31.6^{+1.3}_{-1.6}$  Ma old using the BT-Settl bolometric luminosity-age relationship (Allard et al. 2012).

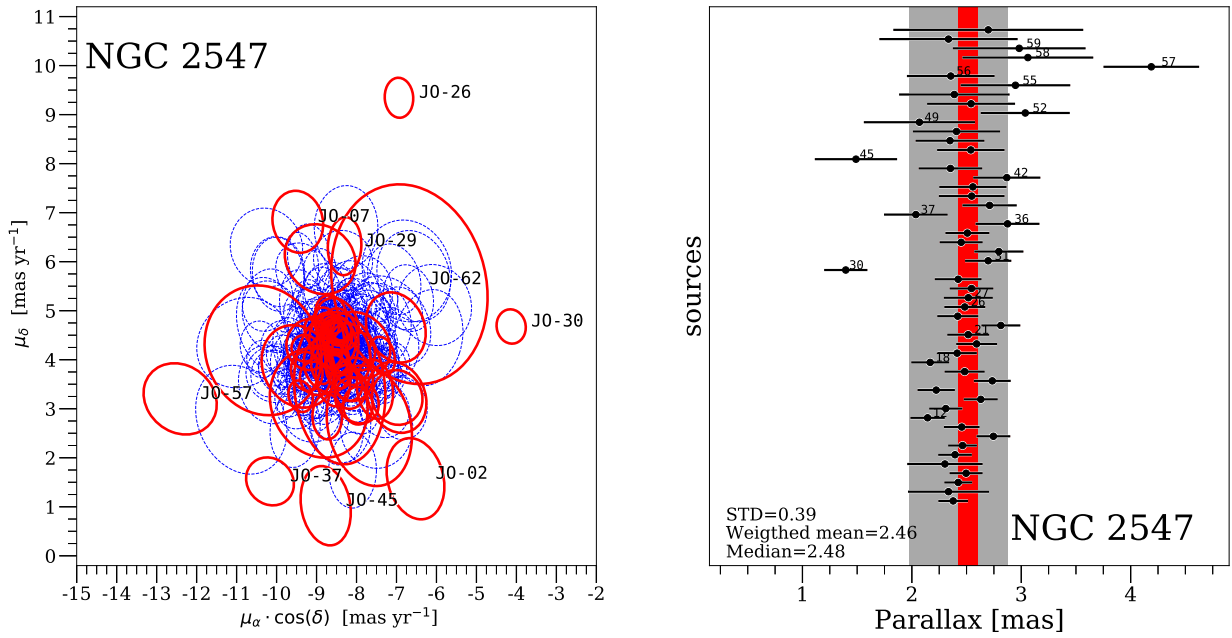


**Fig. A.6.** VPD and parallaxes for NGC 2547. **Left:** Same details as in Fig. 2 but for NGC 2547. **Right:** Same as in Fig. 3 but for NGC 2547.

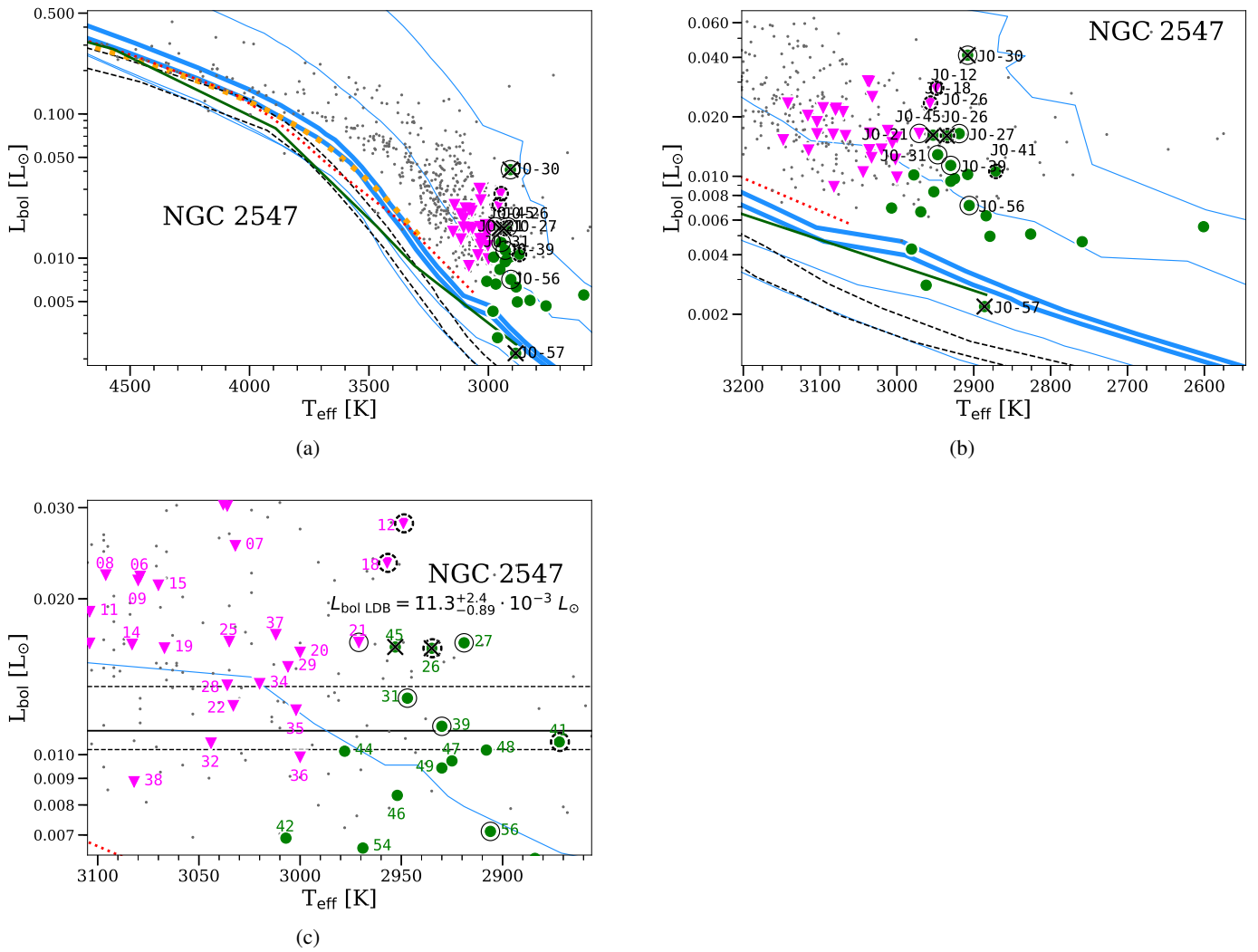


**Fig. A.7.** HRDs and the LDB for NGC 2547. (a) the same as in Fig. 5 and A.2 but for NGC 2547. Thin blue lines correspond to isochrones of 1, 10, 100 Ma, and 1 Ga from the BT-Settl models (Allard et al. 2013), while the thick blue lines to 40 and 50 Ma. The figure includes: a 30 Ma and a 50 Ma isochrone from D'Antona & Mazzitelli 1994 (black dashed lines), a 35 Ma isochrone from Tognelli et al. 2011 (orange dashed dot line), a 40 Ma isochrone from Siess et al. 2000 (red dotted line). (b) Zoom on the (a) plot around the 52 radial velocity members from Jeffries et al. (2004) sample. (c) Zoom around the LDB. NGC 2547 is  $43.5^{+1.7}_{-4.0}$  Ma old using the BT-Settl bolometric luminosity-age relationship (Allard et al. 2012). We show the names of all the objects but not the uncertainties (for the purposes of clarity).

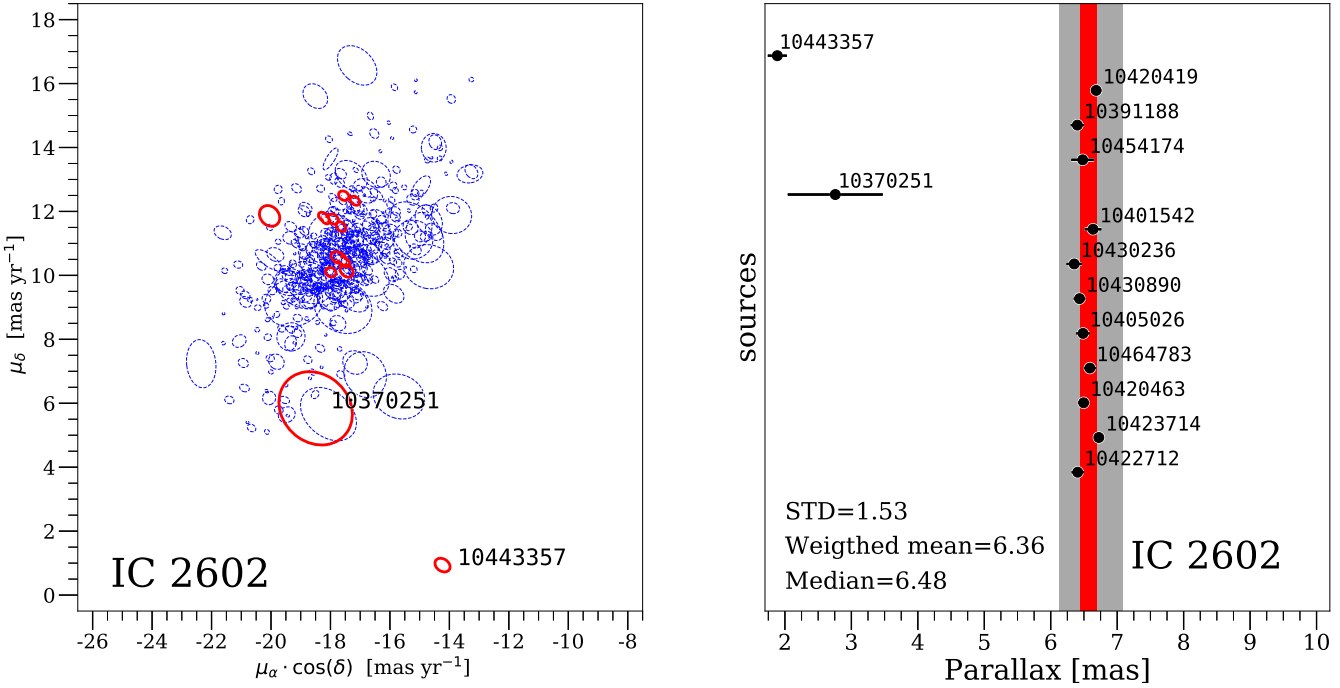


**Fig. A.8.** VPD and parallaxes for IC 2602. **Left:** Same details as in Fig. 2 but for IC 2602. Source 10443357 possesses a proper motion far different than the rest of members. **Right:** Same as in Fig. 3 but for IC 2602.

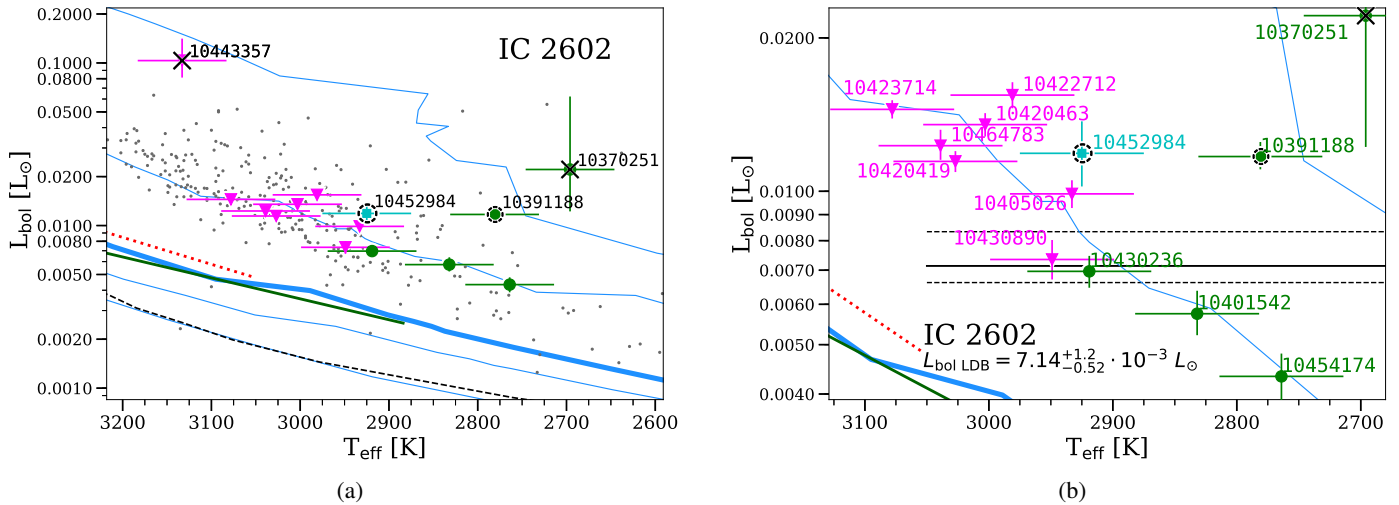


**Fig. A.9.** HRDs and the LDB for IC 2602. **(a):** The same as in Fig. 5 but for IC 2602. Thin blue lines correspond to isochrones of 1, 10, 100 Ma, and 1 Ga from the BT-Settl models (Allard et al. 2013), while the thick blue one to 50 Ma. The figure includes 50 Ma isochrones from: Siess et al. 2000 (red dotted line), D'Antona & Mazzitelli 1994 (black dashed line). **(b):** Zoom on the (a) plot with the LDB. IC 2602 is  $52.5^{+2.2}_{-3.7}$  Ma old using the BT-Settl bolometric luminosity-age relationship (Allard et al. 2012).

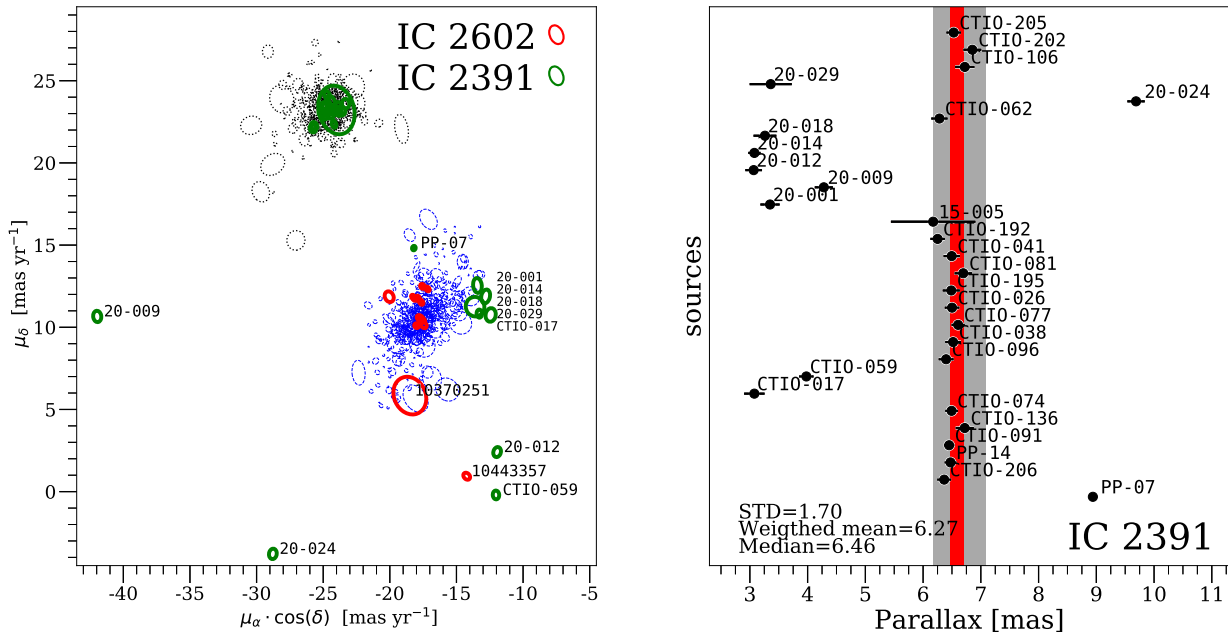


**Fig. A.10.** VPD for IC 2391 and IC 2602 members and parallaxes for IC 2391. **Left:** Same details as in Fig. 2 but for IC 2391 and IC 2602. Some objects have uncertainties smaller than the size of the markers. Black dotted ellipses are the IC 2391 members and blue dashed ellipses are the IC 2602 members, green solid ellipses are the IC 2391 LDB sample objects, and red solid ellipses are the IC 2602 LDB sample objects. **Right:** The same as in Fig. 3 but for IC 2391.

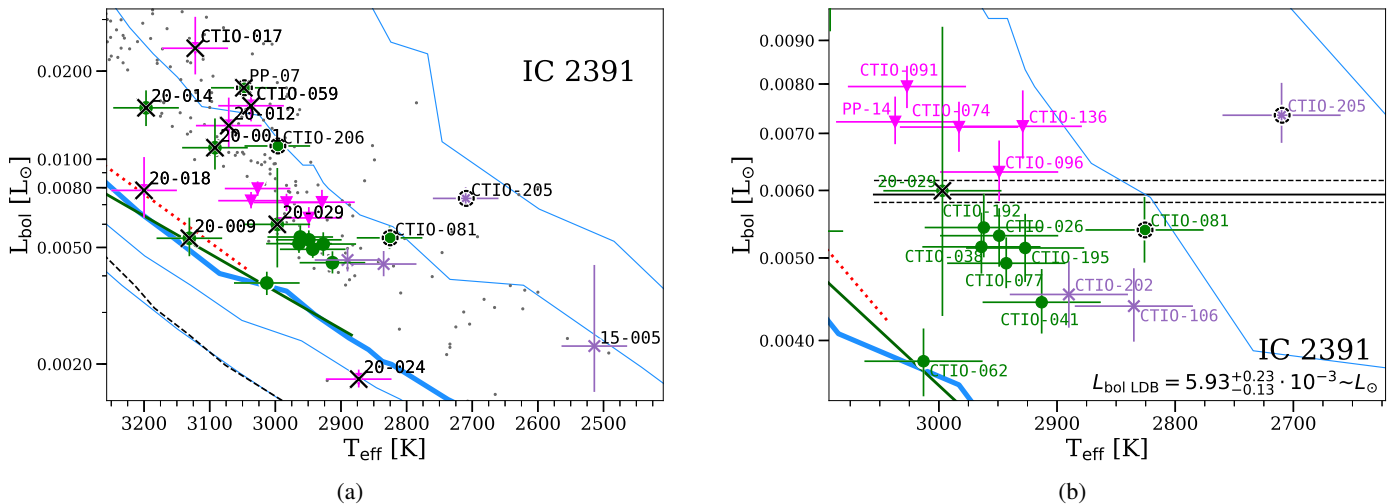


**Fig. A.11.** HRDs and the the LDB for IC 2391. **(a)** The same as in Fig. 5 but for IC 2391. Thin blue lines correspond to isochrones of 1, 10, 100 Ma, and 1 Ga from the BT-Settl models (Allard et al. 2013), while the thick blue one to 60 Ma. The figure includes: a 50 Ma isochrone from D'Antona & Mazzitelli 1994 (black dashed line), a 60 Ma isochrone from Siess et al. 2000 (red dotted line). **(b)** Zoom on the left plot with the location of the LDB. IC 2391 is  $57.7^{+0.5}_{-1.0}$  Ma old using the BT-Settl bolometric luminosity-age relationship (Allard et al. 2012).

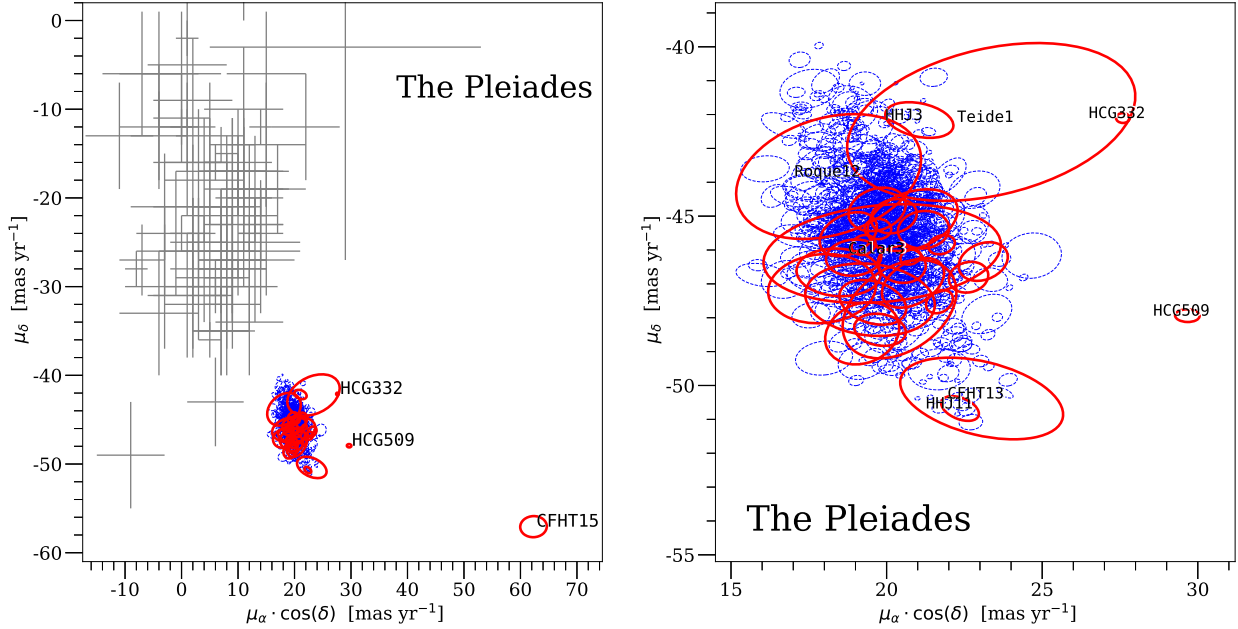


**Fig. A.12.** VPD for the Pleiades. **Left:** Same details as in Fig. 2 but for the Pleiades. Light grey plus symbols are the Taurus-Auriga members taken from the Ducourant et al. (2005) proper motions catalogue. **Right:** Zoom on the left figure.

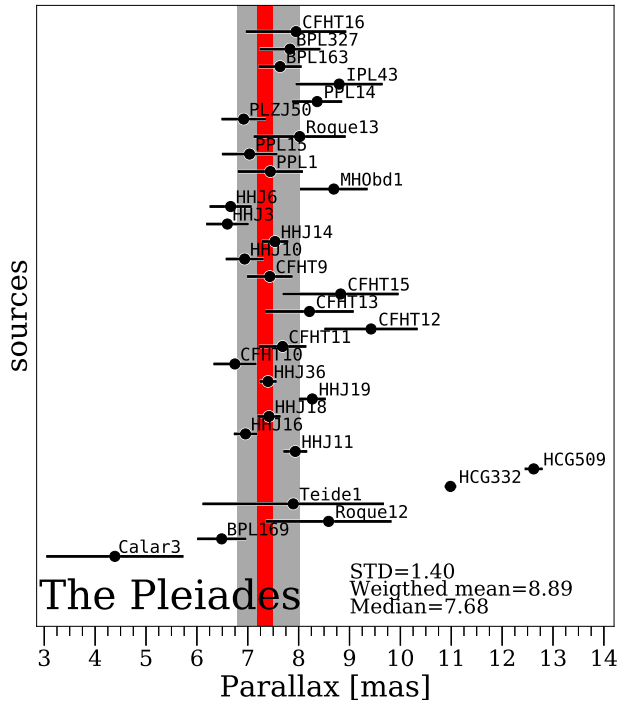


**Fig. A.13.** Parallaxes for the Pleiades members close to the LDB. Same details as in Fig. 3 but for the Pleiades.

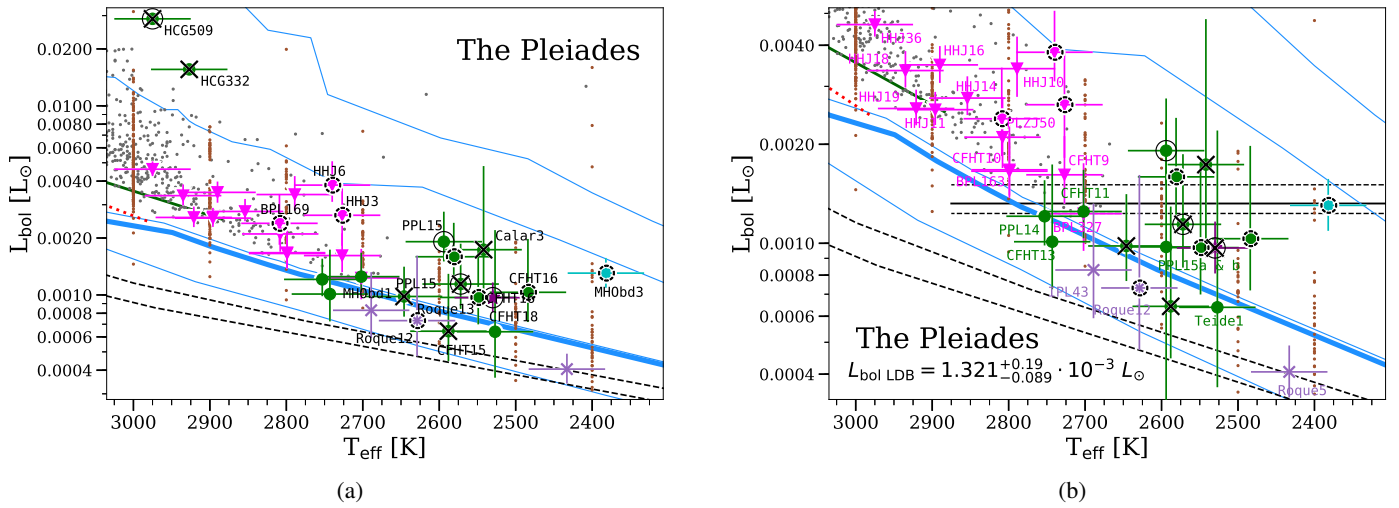


**Fig. A.14.** HRDs and the LDB for the Pleiades. **(a)** The same as in Fig. 5 but for the Pleiades. In addition, grey points are known members from Gaia Collaboration et al. (2018b), and sienna points from Bouy et al. (2015). Thin blue lines correspond to isochrones of 1, 10, 100 Ma, and 1 Ga from the BT-Settl models (Allard et al. 2013), while the thick blue one to 120 Ma. The figure includes: a 100 and 200 Ma isochrones from D'Antona & Mazzitelli 1994 (black dashed lines), and a 120 Ma isochrone from Siess et al. 2000 (red dotted line). **(b)** Zoom on the previous plot with the location of the LDB. The Pleiades is  $127.4^{+6.3}_{-10}$  Ma old using the BT-Settl bolometric luminosity-age relationship (Allard et al. 2012).

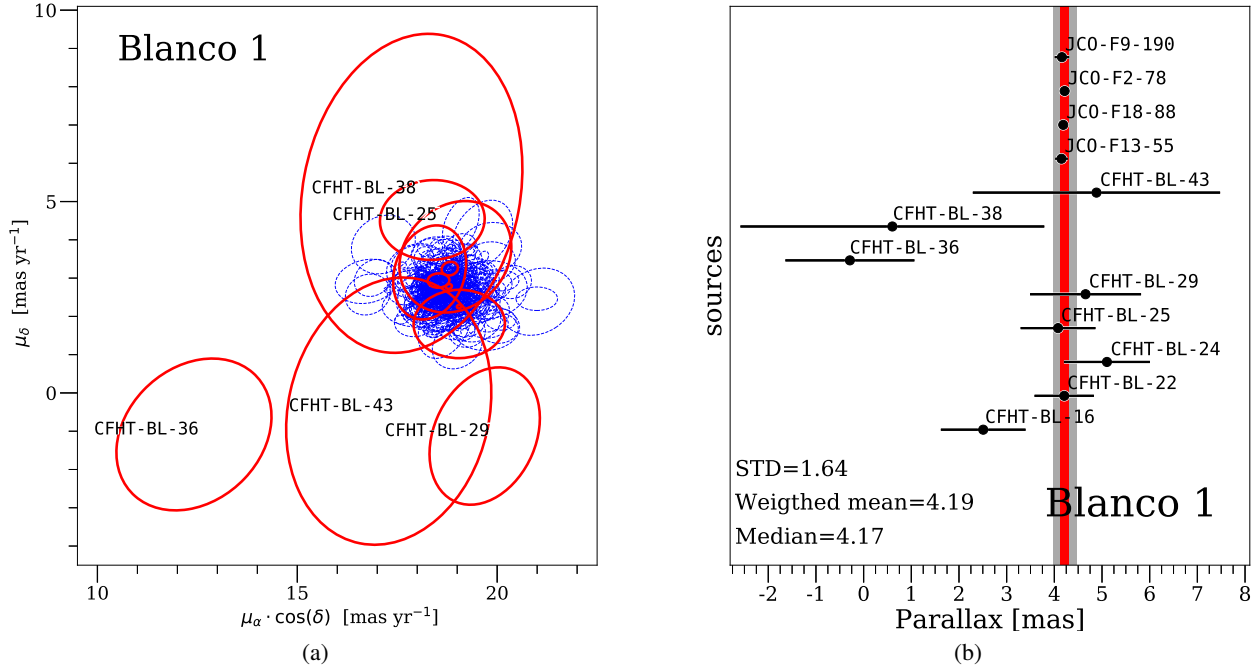


**Fig. A.15.** VPD and parallaxes for Blanco 1. **Left:** Same details as in Fig. 2 but for Blanco 1. **Right:** Same as in Fig. 3 but for Blanco 1. We note that CFHT-BL-36 has got negative parallax.

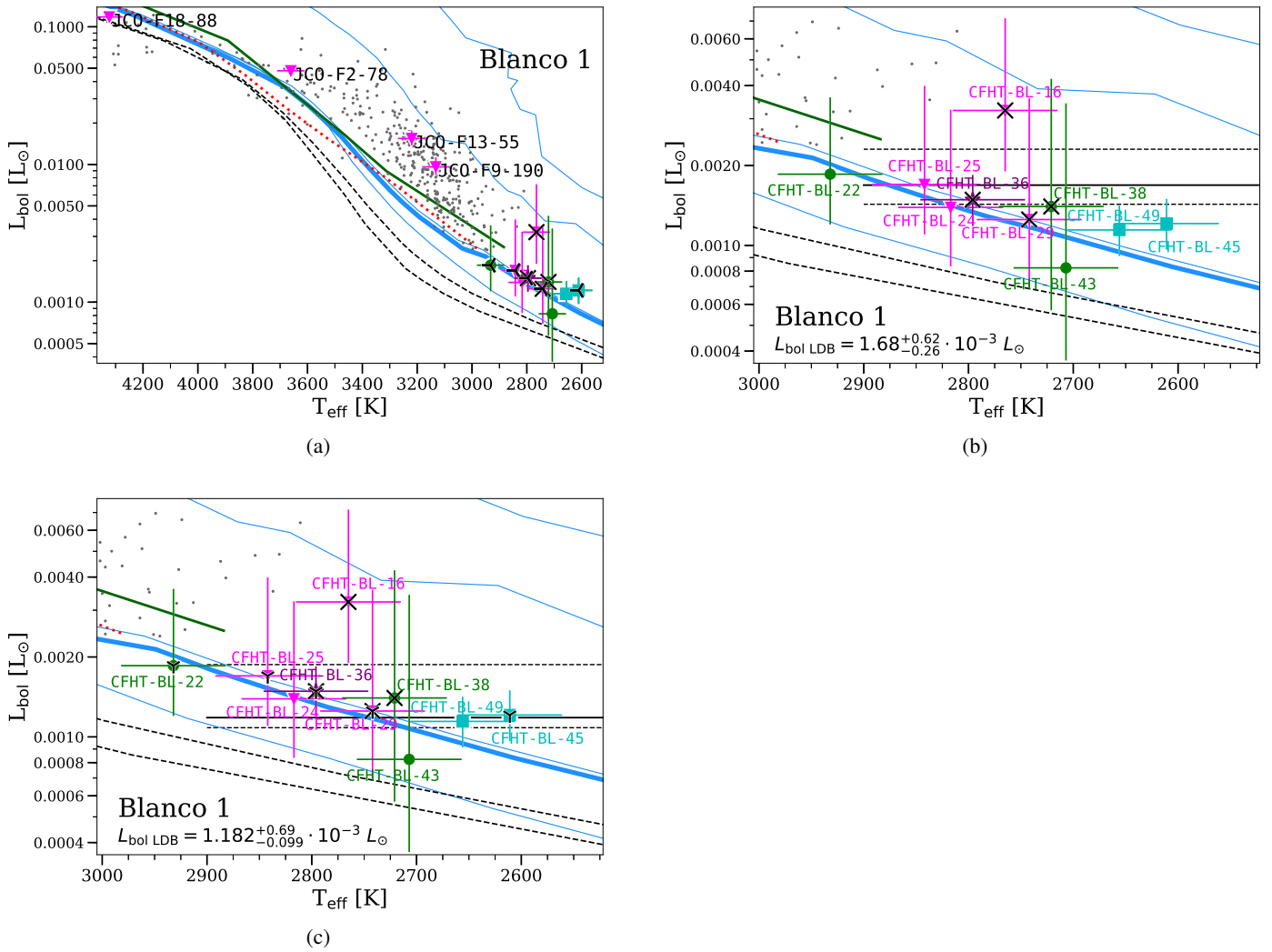


**Fig. A.16.** HRDs and the LDB for Blanco 1. (a) Same as in Fig. 5 but for Blanco 1. Thin blue lines correspond to isochrones of 1, 10, 100 Ma, and 1 Ga from the BT-Settl models (Allard et al. 2013), while the thick blue one to 120 Ma. The figure includes: a 120 Ma isochrone from Siess et al. 2000 (red dotted line), a 100 and a 200 Ma from D'Antona & Mazzitelli 1994 (black dashed lines). The rest of the symbols follow the same convention as previous HRDs. (b) Zoom on the left plot close to the LDB. The Blanco 1 age is  $110.9^{+9.0}_{-23}$  Ma old using the BT-Settl bolometric luminosity-age relationship (Allard et al. 2012). (c) Same as (b), but the LDB is located after discarding sources whose radial velocities are not within the  $1\sigma$  radial velocity criterion, see Section 2.8. The tri-down symbols are over-imposed in the non-members following this criterion. The Blanco 1 age is  $137.1^{+7.0}_{-33}$  Ma (BT-Settl models from Allard et al. 2012).

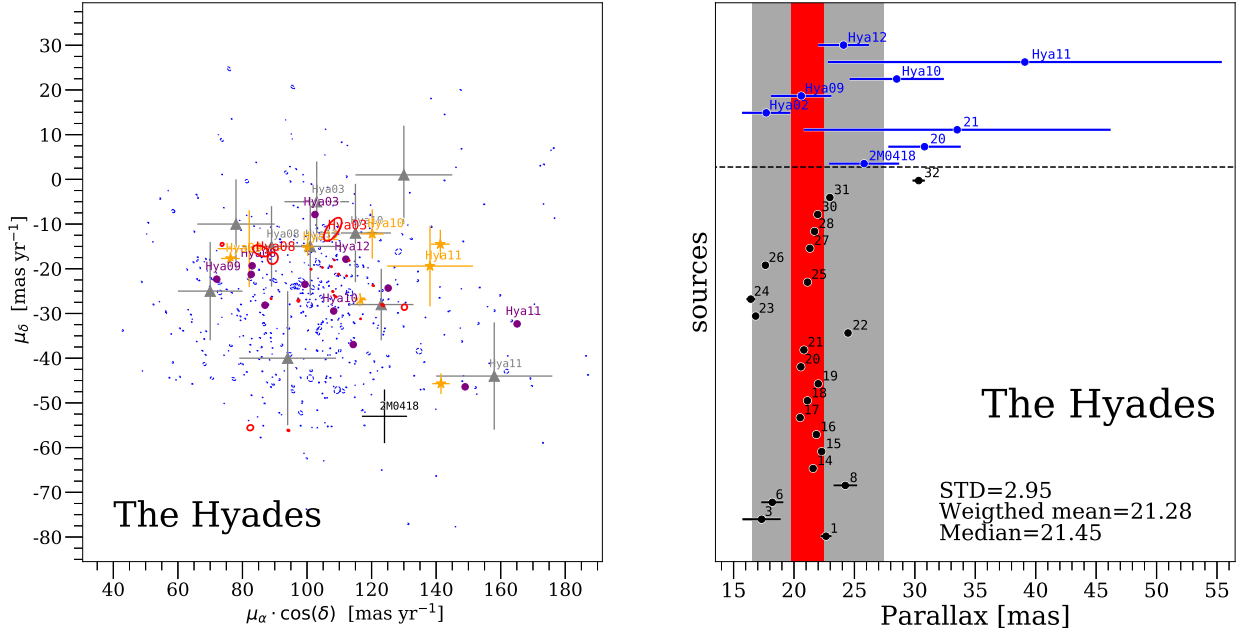
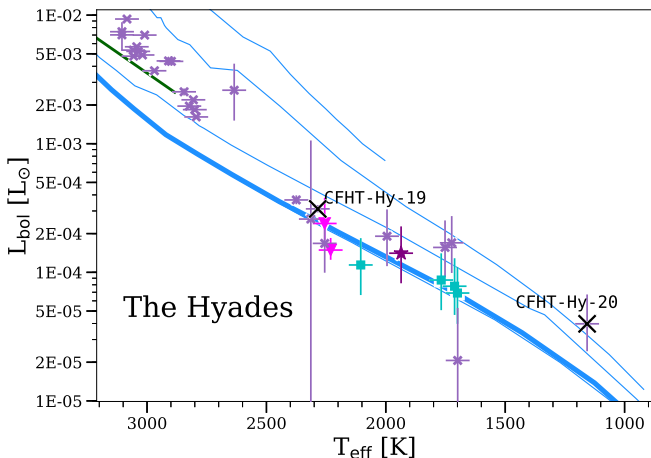
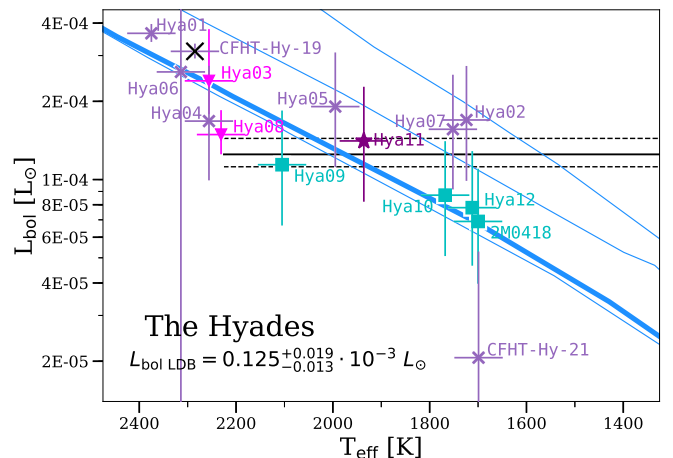


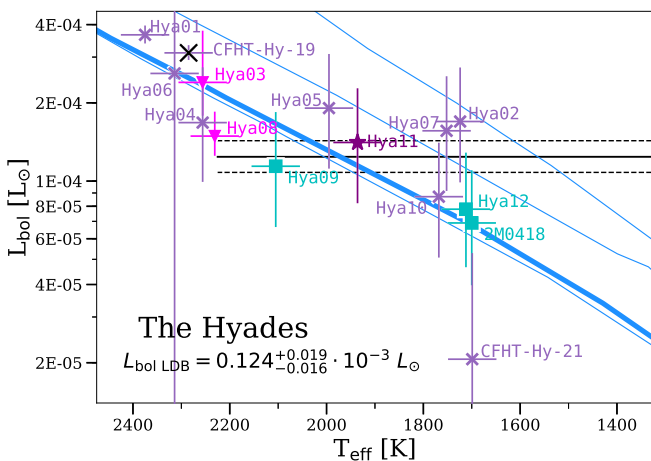
**Fig. A.17.** VPD and parallaxes for the Hyades. **Left:** Same as in Fig. 2 but for the Hyades. We have added proper motions for the LDB sample sources from: Hogan et al. 2008 (purple filled circles); Lodieu et al. 2014 (grey triangles with their uncertainties); Pérez-Garrido et al. 2017 (the 2M0418, the black plus symbol); Lodieu et al. 2019b (orange stars with their uncertainties). **Right:** Same as in Fig. 3 but for the Hyades. We have added parallax values from Lodieu et al. (2019b) in blue, (above the black dashed line).



(a)



(b)



(c)

**Fig. A.18.** HRDs and the LDB for the Hyades. (a) The same as in Fig. 5 but for the Hyades. Thin blue lines correspond to isochrones of 1, 10, 100 Ma, and 1 Ga from the BT-Settl models (Allard et al. 2013), while the thick blue one to 700 Ma. (b) Zoom on the previous plot close to the LDB. (c) Same as the previous plot but, we considered that Hya10 has an unclear lithium detection. The Hyades is  $695^{+85}_{-67}$  Ma old using the BT-Settl bolometric luminosity-age relationship (Allard et al. 2012).

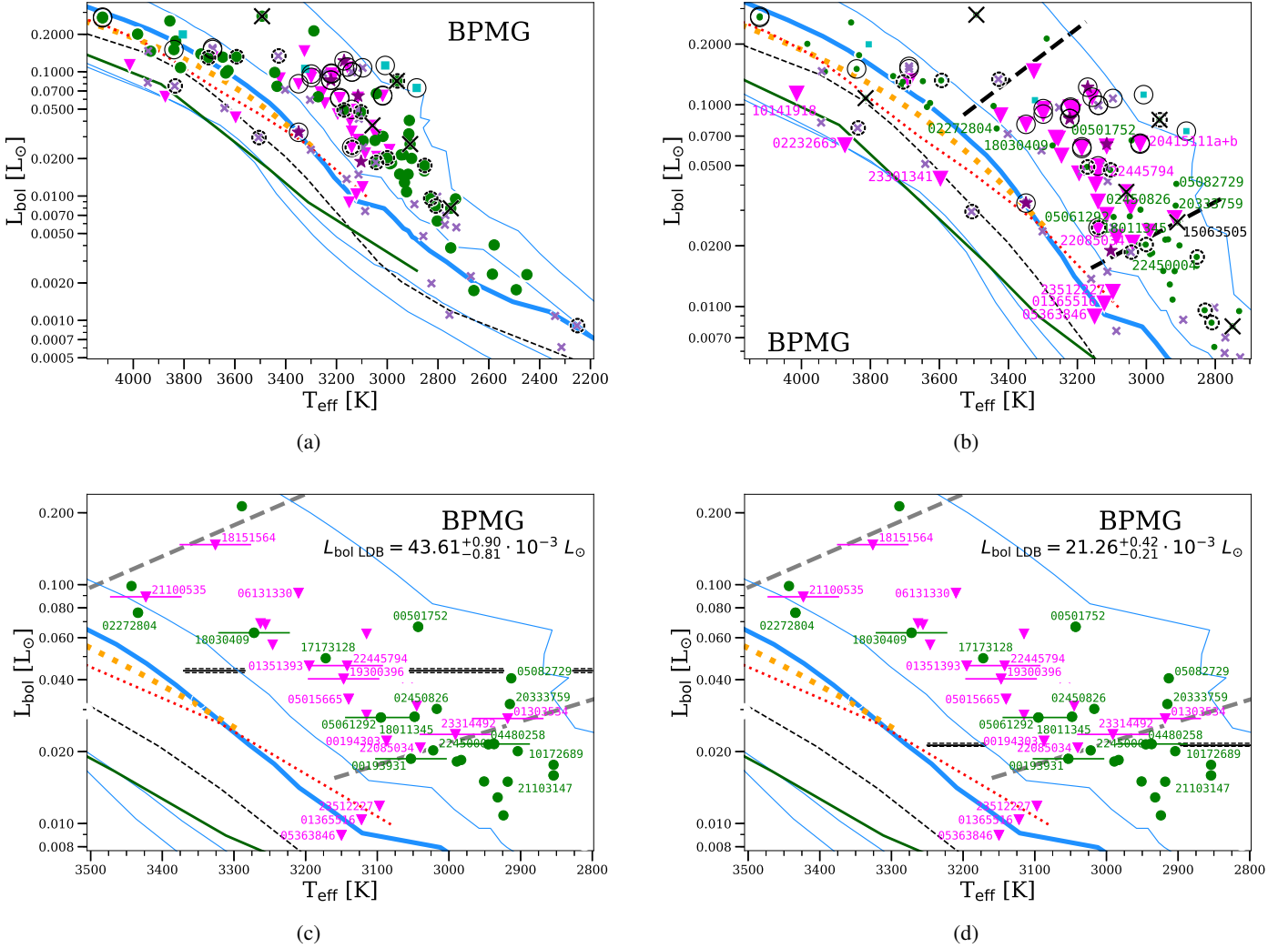


**Fig. A.19.** HRDs and the LDB for the BPMG. (a) The same as in Fig. 5 but for the BPMG. Empty large black broken line circles are suspected multiple systems or sources with associated background objects and photometric data blended in some bands. Thin blue lines correspond to isochrones of 1, 10, 100 Ma, and 1 Ga from the BT-Settl models (Allard et al. 2013), while the thick blue one to 20 Ma. Uncertainties are not shown in order to gain clarity, although in the bolometric luminosities are usually smaller than the symbols, with the exception of some sources without parallaxes. The figure includes 20 Ma isochrones from: D'Antona & Mazzitelli 1994 (black dashed line), Siess et al. 2000 (red dotted line), and a 17 Ma from Tognelli et al. 2011 (orange dashed dot line). (b) Zoom on the (a) plot around the LDB. The size of lithium-poor sources has been increased to locate the LDB. The area delimited by them is marked with gray thick dashed lines. Some remarkable sources are labelled. (c) Same as the previous plot with the LDB locus determined following the first scenario. Since we focus on the sole aim of locating the LDB, we do not show: sources that are confirmed or suspected multiple systems; sources with two or several associated objects (third configuration) with photometric data blended in some bands; non-members; sources with undetected lithium feature; and objects without parallaxes. Effective temperatures uncertainties are shown in some lithium poor objects in order to gain clarity. Bolometric luminosities uncertainties are smaller than the size of the symbols. The BPMG is  $24.3^{+0.3}_{-0.3}$  Ma old using the BT-Settl bolometric luminosity-age relationship (Allard et al. 2012). (d) Same as the previous plot with the LDB locus determined following the second scenario.

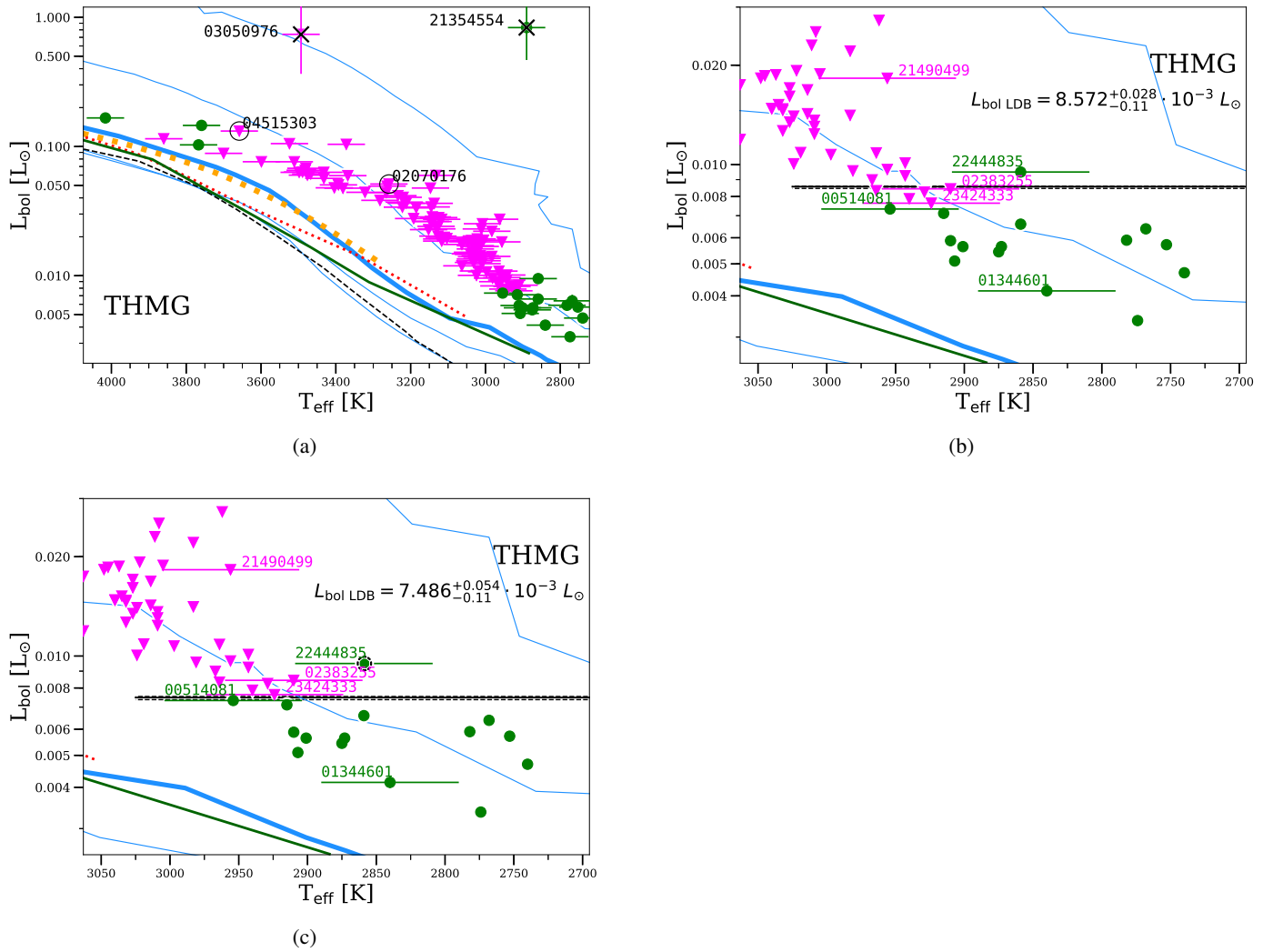


**Fig. A.20.** HRDs and the LDB for the THMG. (a) Same as in Fig. 5 but for THMG. Thin blue lines correspond to isochrones of 1, 10, 100 Ma, and 1 Ga from the BT-Settl models (Allard et al. 2013), while the thick blue one to 50 Ma. The figure includes 50 Ma isochrones from: D'Antona & Mazzitelli 1994 (black dashed line), and Siess et al. 2000 (red dotted line). It also includes a 40 Ma isochrone from Tognelli et al. 2011 (orange dashed dot line). (b) Zoom on the (a) plot around the LDB following the first scenario. To retain clarity, we have only drawn the effective temperature uncertainties and the names for the sources that defined the LDB and two additional sources. The uncertainties in the bolometric luminosities are usually smaller than the size of the symbols. (c) Same as (b), but the LDB is located following the second scenario (Section 2.11). The THMG is  $51.0^{+0.5}_{-0.2}$  Ma old using the BT-Settl bolometric luminosity-age relationship (Allard et al. 2012).

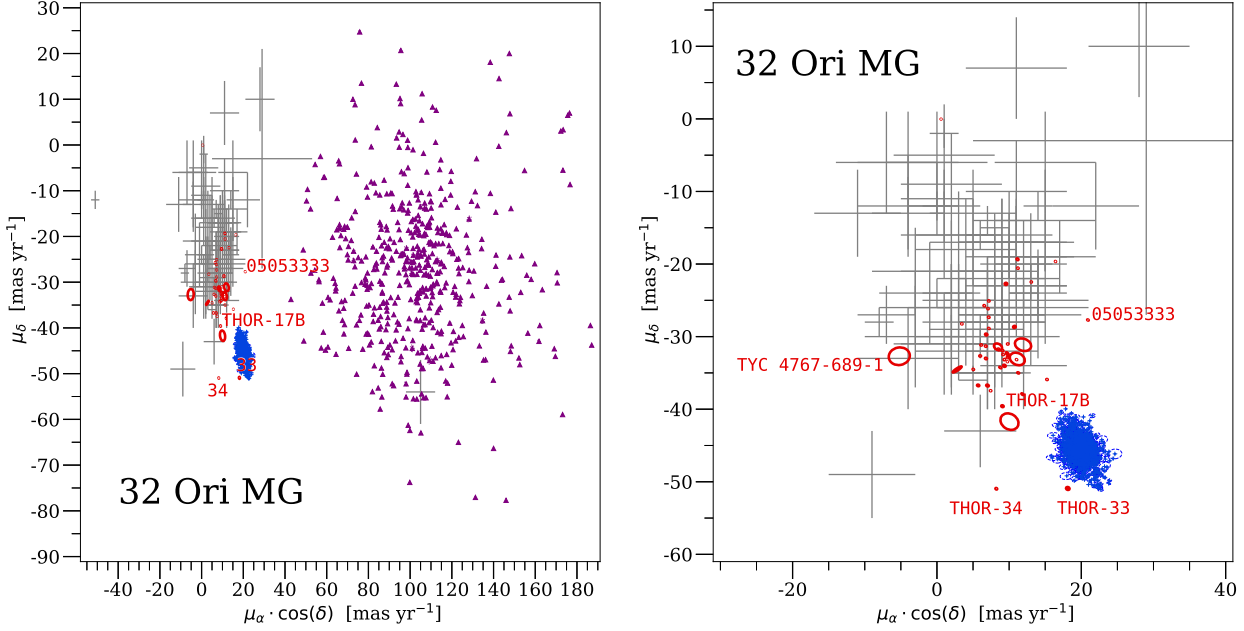


**Fig. A.21.** VPDs for the 32 Ori MG. **Left:** The red ellipses are all 32 Ori MG members (Bell et al. 2017); the black filled triangles are Hyades members and the blue squares are Pleiades members, (both from Gaia Collaboration et al. 2018b); and the light grey plus symbols are the Taurus-Auriga members taken from Ducourant et al. (2005). The size of the symbols is greater than the size of the uncertainties (shown as ellipses). **Right:** Zoom on the previous plot.

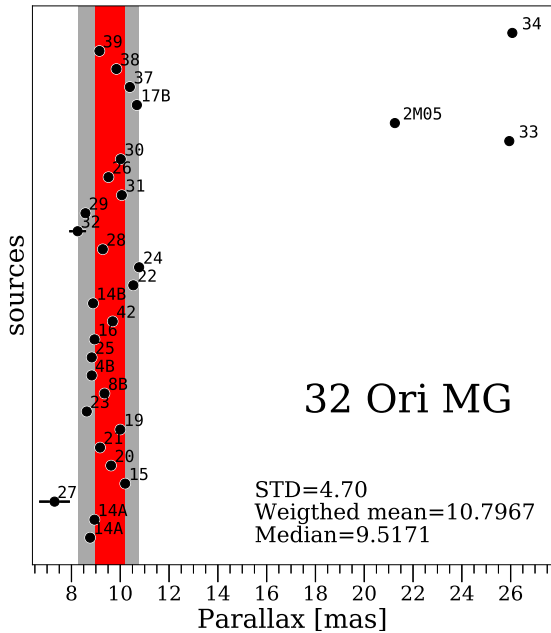


**Fig. A.22.** Parallaxes for the 32 Ori MG members close to the LDB. Same as in Fig. 3 but for the 32 Ori MG. We removed the 'THOR-' prefix of each object from the name.

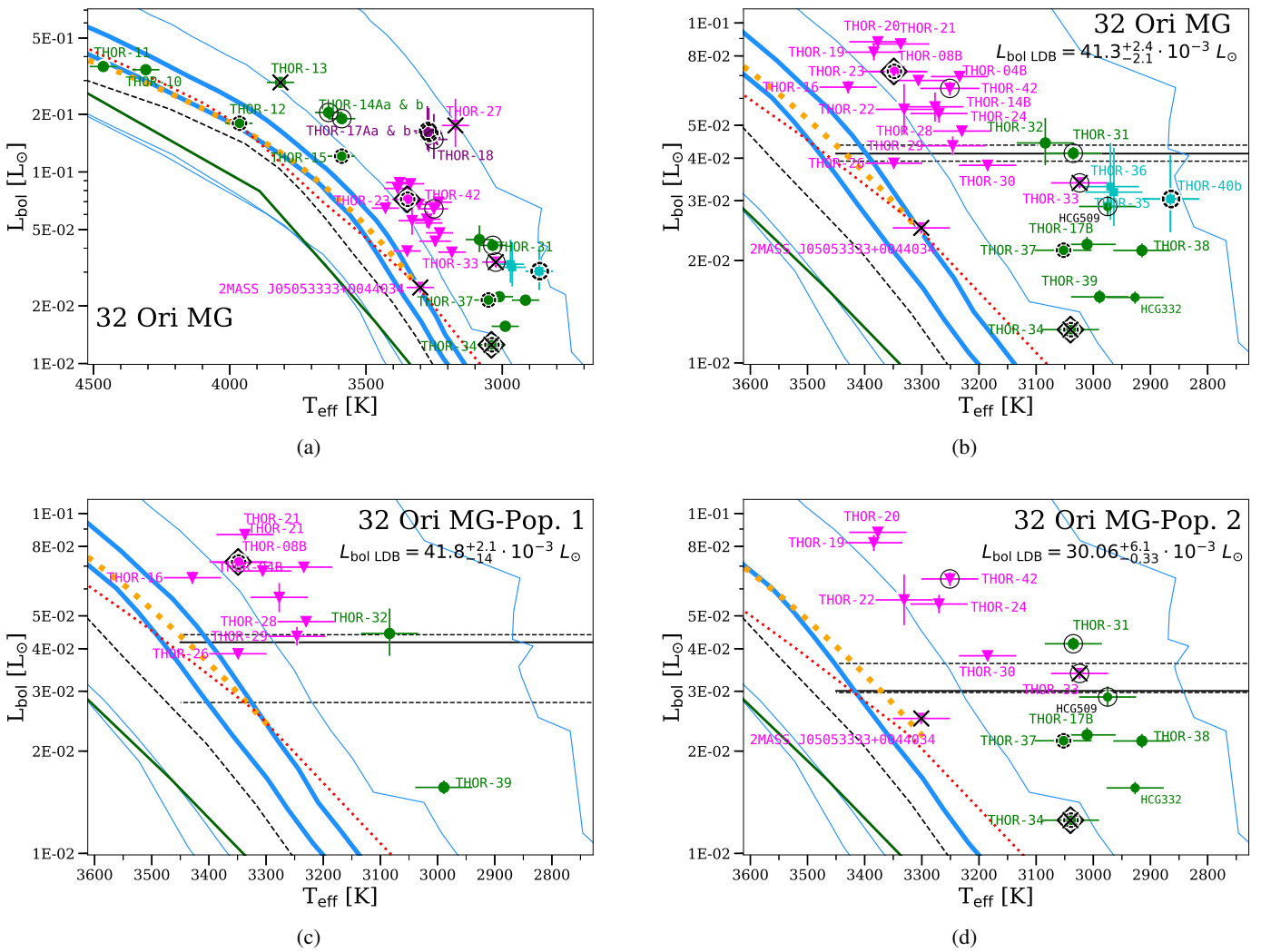


**Fig. A.23.** HRDs and the LDB for the 32 Ori MG. (a) The same as in Fig. 5 but for 32 Ori MG. Empty black diamonds correspond to fast rotators. Thin blue lines correspond to isochrones of 1, 10, 100 Ma, and 1 Ga from the BT-Settl models (Allard et al. 2013), while the thick blue lines to a 20 and 30 Ma. The figure includes 20 Ma isochrones from Siess et al. 2000 (red dotted line), and D’Antona & Mazzitelli 1994 (black dashed line). It also includes a 18 Ma isochrone from Tognelli et al. 2011 (orange dashed dot line). (b) Zoom on the previous plot around the LDB. We added the sources HCG 332 and HCG 509 (see Section 2.12). The 32 Ori MG is  $25.0^{+0.7}_{-0.82}$  Ma old using the BT-Settl bolometric luminosity-age relationship (Allard et al. 2012). (c) Zoom on the LDB for 32 Ori MG population 1, see Appendix D. The 32 Ori MG population 1 is  $24.9^{+4.5}_{-0.7}$  Ma (BT-Settl models from Allard et al. 2012). (d) Zoom on the LDB for 32 Ori MG population 2, see Appendix D. Thin blue lines correspond to isochrones of 1, 10, 100 Ma, and 1 Ga from the BT-Settl models (Allard et al. 2013), while the thick blue one to 30 Ma. The figure includes: a 25 Ma isochrone from Siess et al. 2000 (red dotted line), a 20 Ma isochrone from D’Antona & Mazzitelli 1994 (black dashed line), and a 20 Ma isochrone from Tognelli et al. 2011 (orange dashed dot line). The 32 Ori MG population 2 is  $28.6^{+0.1}_{-2.0}$  Ma (BT-Settl models from Allard et al. 2012).

## Appendix B: Variation of the LDB with the reddening

We adopted two very different reddening values for Alpha Persei:  $A_V = 0.279$  mag from Gaia Collaboration et al. (2018b), and  $A_V = 0.055^{+0.018}_{-0.017}$  mag from Bossini et al. (2019) with  $(m - M)_0 = 5.824$  mag, 146 pc.

We studied the variation of the stellar parameters,  $L_{\text{bol}}$  and  $T_{\text{eff}}$ , with both reddening values. We proceeded in the same way as in the whole article: we created two input files for VOSA, one with  $A_V = 0.279$  mag and other with  $A_V = 0.055$  mag. We show the results in Figure B.1 and in Table B.1.

A reddening of  $A_V = 0.279$  mag produced brighter luminosities and hotter effective temperatures than  $A_V = 0.055$  mag: a median offset of  $0.21 \cdot 10^{-3} L_\odot$  with standard deviation of  $\pm 0.53 \cdot 10^{-3} L_\odot$ , and a systematic median offset of 79 K with standard deviation of  $\pm 28$  K. In terms of percentages these changes were: 6.3% in bolometric luminosities (reaching a maximum of 8.3%) and 2.2 % in  $T_{\text{eff}}$ . This change also affects the location of the LDB: using  $A_V = 0.279$  mag we found  $L_{\text{bol}} \text{ LDB} = 2.98^{+0.35}_{-0.19} \cdot 10^{-3} L_\odot$  and  $T_{\text{eff}} \text{ LDB} = 2857 \pm 74$  K; using  $A_V = 0.055$  mag we found  $L_{\text{bol}} \text{ LDB} = 2.74^{+0.40}_{-0.15} \cdot 10^{-3} L_\odot$  and  $T_{\text{eff}} \text{ LDB} = 2806 \pm 71$  K (Table B.2). The HRD show the changes (Figure B.2).

We conclude that a higher level of reddening produces an LDB at brighter bolometric luminosities and hotter effective temperatures and, therefore, younger ages. Ages obtained using the two reddening values with different evolutionary models for Alpha Persei are shown in Table B.2. We estimated that a decrease of 80% in  $A_V$  produces an increase in age between 3 and 6 Ma depending on the model. These variations may not be the same in stellar associations such as the Hyades (older and closer) or NGC 1960 (younger and further).

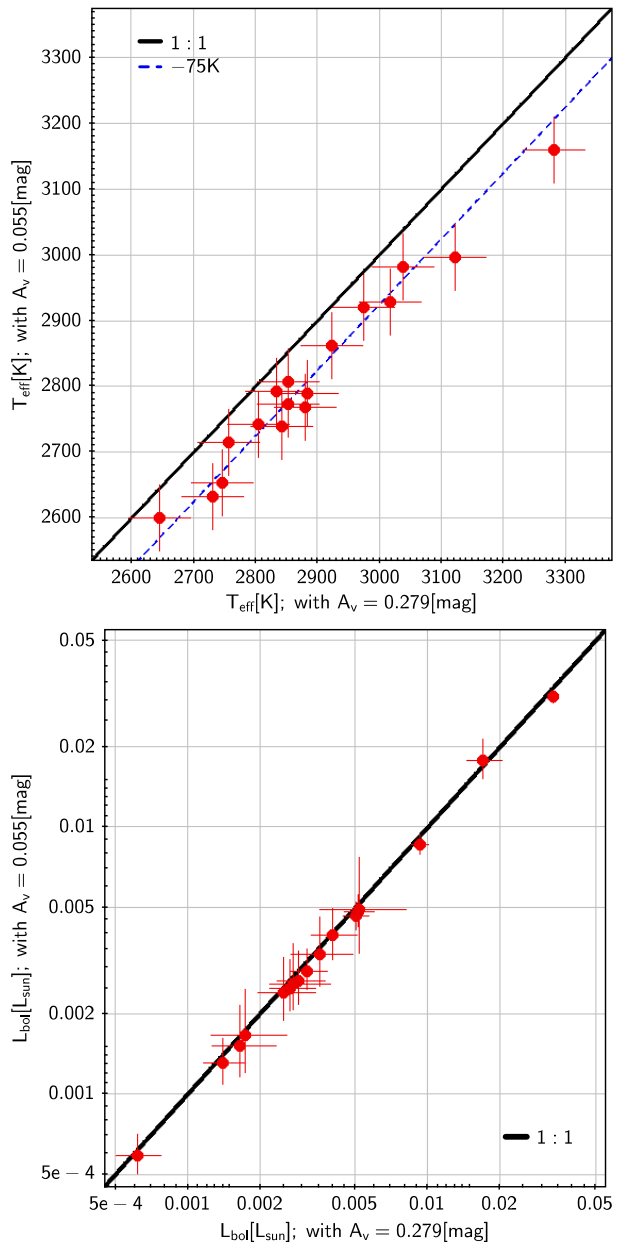


**Fig. B.1.** Comparison between stellar parameters for Alpha Persei LDB sample using two different reddening values for the objects  $A_V = 0.259$  mag and  $A_V = 0.055$  mag. **Top:** Comparative analysis between **effective temperatures** shown as a 1:1 line and a dashed one shifted 75 K. **Bottom:** Comparison between bolometric luminosities.

**Table B.1.** Stellar properties for the Alpha Persei LDB sample derived using two different reddening values.

Object	$A_V = 0.279$ mag				$A_V = 0.055$ mag				diff $T_{\text{eff}}$ [K]	diff $T_{\text{eff}}$ %	diff $L_{\text{bol}}$ $10^{-3} [L_{\odot}]$	diff $L_{\text{bol}} \%$
	$T_{\text{eff}}$ [K]	$L_{\text{bol}}$ $10^{-3} [L_{\odot}]$	$L_{\text{bol}} 97.5\text{th}$ $10^{-3} [L_{\odot}]$	$L_{\text{bol}} 2.5\text{th}$ $10^{-3} [L_{\odot}]$	$T_{\text{eff}}$ [K]	$L_{\text{bol}}$ $10^{-3} [L_{\odot}]$	$L_{\text{bol}} 97.5\text{th}$ $10^{-3} [L_{\odot}]$	$L_{\text{bol}} 2.5\text{th}$ $10^{-3} [L_{\odot}]$				
AP165	3 282	33.025	31.378	34.814	3 159	30.652	29.124	32.312	123	3.74	2.372	7.18
AP296	3 122	16.978	14.557	20.346	2 997	17.648	15.127	21.156	125	4.00	0.670	3.94
AP284	3 038	9.288	8.568	10.117	2 981	8.588	7.922	9.354	57	1.87	0.700	7.54
AP322	2 974	5.182	3.569	8.082	2 921	4.894	3.351	7.678	53	1.78	0.287	5.54
AP268	3 018	5.155	4.525	5.991	2 928	4.831	4.241	5.614	90	2.98	0.323	6.28
AP272	2 923	5.030	4.463	5.662	2 862	4.658	4.135	5.240	61	2.08	0.371	7.38
AP275	2 853	4.004	3.252	5.044	2 808	3.930	3.192	4.951	45	1.57	0.073	1.84
AP325	2 646	3.541	2.686	4.873	2 601	3.332	2.528	4.586	45	1.70	0.208	5.88
AP318	2 834	3.143	2.683	3.809	2 793	2.873	2.452	3.481	41	1.44	0.270	8.60
AP323	2 805	2.911	2.385	3.762	2 742	2.662	2.181	3.440	63	2.24	0.249	8.56
AP313	2 883	2.758	2.204	3.924	2 789	2.581	2.063	3.672	94	3.26	0.176	6.41
AP270	2 881	2.677	2.200	3.432	2 768	2.500	2.055	3.204	113	3.92	0.176	6.60
AP300	2 842	2.521	1.966	3.440	2 740	2.394	1.881	3.241	102	3.58	0.127	5.03
AP324	2 757	1.746	1.266	2.598	2 715	1.668	1.211	2.478	42	1.52	0.078	4.48
AP315	2 747	1.653	1.264	2.339	2 653	1.520	1.160	2.155	94	3.42	0.133	8.05
AP310	2 853	1.399	1.164	1.737	2 774	1.313	1.097	1.624	79	2.76	0.085	6.13
AP317	2 731	0.622	0.509	0.780	2 632	0.587	0.504	0.704	99	3.62	0.035	5.62

**Table B.2.** Alpha Persei LDB loci in terms of  $L_{\text{bol}}$ ,  $T_{\text{eff}}$  and the ages derived using several evolutionary models.

Stellar Association	$L_{\text{bol}}$ LDB $10^{-3} [L_{\odot}]$	$T_{\text{eff}}$ LDB [K]	LDB ages based on $L_{\text{bol}}$					
			D&M [Ma]	Burrows [Ma]	Siess [Ma]	Burke [Ma]	BT-Settl [Ma]	Pisa [Ma]
Alpha Persei $A_V = 0.279$ mag	$2.98^{+0.35}_{-0.19}$	2 857	$69.8^{+4.5}_{-1.6}$ (3 222)	$76.1^{+3.3}_{-5.2}$ (3 113)	$> 70$ (< 230)	$77.8^{+2.5}_{-4.9}$ (3 109)	$79.0^{+1.5}_{-2.3}$ (2 983)	$70.1^{+2.8}_{-4.2}$ (3 001)
Alpha Persei $A_V = 0.055$ mag	$2.74^{+0.40}_{-0.15}$	2 806	$75.9^{+4.4}_{-6.8}$ (3 210)	$80.4^{+3.1}_{-6.8}$ (3 096)	$> 70$ (< 230)	$81.2^{+3.8}_{-5.6}$ (3 089)	$81.3^{+2.4}_{-3.4}$ (2 961)	$73.8^{+2.6}_{-5.6}$ (2 985)

**Notes:** The columns and explanations are the same as in Table 3.

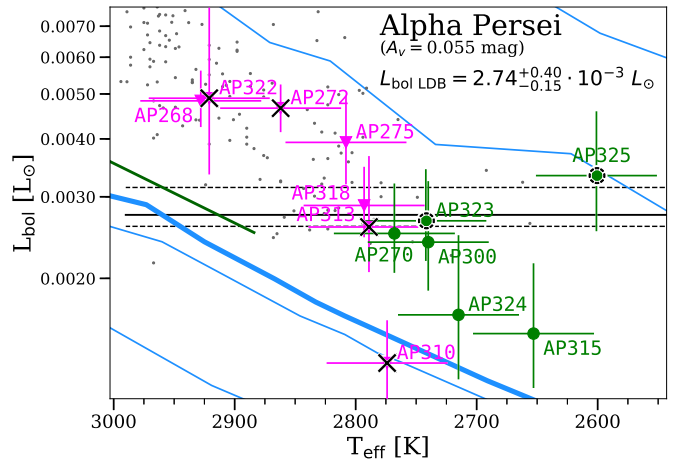
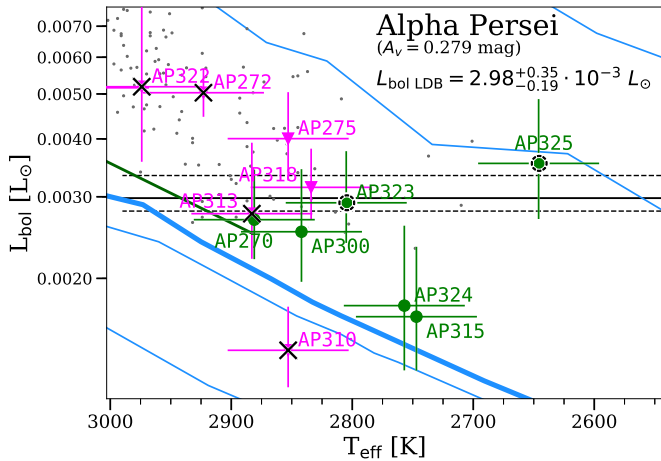


**Fig. B.2.** HRDs around the Alpha Persei LDB sample using two different reddening values. the blue isochrones correspond to BT-Settl models (Allard et al. 2013), with ages of 1, 10, 80, 100 Ma, and 1 Ga, where the thick one corresponds to a 80 Ma. We also show the Zero Age Main Sequence (Stahler & Palla 2005) as the green solid line. We have used the same symbols and standards than previous HRDs. **Left:** Reddening used is  $A_V = 0.279$  mag. It is  $79.0^{+1.5}_{-2.3}$  Ma old using the BT-Settl bolometric luminosity-age relationship (Allard et al. 2012). **Right:** Reddening used is  $A_V = 0.055$  mag. It is  $81.3^{+2.4}_{-3.4}$  Ma old using the BT-Settl bolometric luminosity-age relationship (Allard et al. 2012).

## Appendix C: Discussion of individual objects from BPMG

In this appendix, we provide information and remarks about some objects of the BPMG LDB sample. Some of them are visual binaries or multiple systems only resolved in *Gaia* DR2 and their bolometric luminosities are a combination of two or several sources in all photometric bands (except for *Gaia*). In these cases, we calculated the bolometric luminosities with the photometric bands as are given in the catalogues using the parallax of each of the components.

**00164976** has a counterpart in *Gaia* DR2, 386050700157461760, without an astrometric solution.

**00275023** (2MASS J 00275023-3233060, GJ 2006 A) and **00275035** (2MASS J 00275035-3233238, GJ 2006 B) form a wide binary system.

**01071194** has a counterpart in *Gaia* DR2, 2353128266975662080, without an astrometric solution.

**01112542** is a lithium-rich binary system (GJ 3076 AB, LP 467-16) with a separation between the two main components of  $0.41''$  (Beuzit et al. 2004) or  $0.293 \pm 0.002''$  (Janson et al. 2012). The system lacks a counterpart in *Gaia* DR2.

**01132817** is a binary system that is only resolved in *Gaia* DR2, composed of 4988735051246293504 (01132817a with  $\varpi = 19.95$  mas) and 4988735051245195008 (01132817b with  $\varpi = 19.67$  mas), both components with similar proper motions and are separated by  $1.549''$ .

**01535076** is a binary system resolved in *Gaia* DR2: 5143033331902438656 (01535076a  $\varpi = 29.54$  mas) and 5143033331901973888 (01535076b  $\varpi = 29.53$  mas) with a separation of  $2.792''$ .

**02335984** is a binary system resolved in *Gaia* DR2: 5132219016567875200 (02335984a,  $G = 13.53$  mag and  $\varpi = 12.41$  mas) and 5132219012272775808 (02335984b,  $G = 13.54$  mag without parallax and proper motions). It was previously identified by Bergfors et al. (2010).

**02365171** (GSC 08056-00482 with  $25.742$  mas) was considered as a possible outlier (Shkolnik et al. 2017) but we have discarded this possibility.

**02485260** is classified as a single line binary (Malo et al. 2014a and Shkolnik et al. 2017).

**03323578** lacks counterpart in *Gaia* DR2.

**03363144** has a  $\varpi = 22.04$  mas and was considered as a possible outlier (Shkolnik et al. 2017), but we have discarded this possibility

**03393700** has associated three sources in *Gaia* DR2: 244734761312058240, with  $0.38$  mas, 244734765606605824 without parallax and the right counterpart 244734765608363136 with  $\varpi = 24.8$  mas, a spectroscopic binary (Skinner et al. 2018).

**04593483** (V1005 Ori) is a spectroscopic binary (Elliott et al. 2014).

**05015881** is a double system (Song et al. 2003) or a quadruple system (HIP 23418 ABCD, see Malo et al. 2013). Mason et al. (2018) calculated a separation between the two main components of  $1.234''$ . Two components are resolved in the *Gaia* DR2: GJ 3322A (3291643148740384128, LP 476-207 A, 05015881a) and GJ 3322B (3291643148741783296, LP 476-207 B, 05015881b). Song et al. (2003) found that the combined system HIP 23418 shows prominent emission lines of Na D  $\lambda\lambda 5890$  Å and  $\lambda 5896$  Å, He I  $\lambda 5876$  Å and  $\lambda 6876$  Å, and H $\alpha$ .

**05241914** lacks counterpart in *Gaia* DR2, 2MASS J 05241914-1601153 probably because it is a binary system, M4.5+M5.0, with a separation of  $0.639 \pm 0.001''$  (Bergfors et al. 2010). Lithium has been detected in the binary

system (unresolved spectra from Malo et al. 2013 and Binks & Jeffries 2014).

**05320450** (2MASS J 05320450-0305291, V1311 Ori) has a counterpart in *Gaia* DR2: 3216729573251961856 ( $\varpi = 28.94$  mas) and it is identified as a lithium rich member in da Silva et al. (2009) just like Malo et al. (2013). Binks & Jeffries (2016) also detected lithium but they did not consider it as a member. Finally, Janson et al. (2012) reported this object as a binary system, M2V+M3.5V, with a separation of  $0.216 \pm 0.003''$ .

**10172689** (5355751581627180288 with  $\varpi = 51.00$  mas) could be contaminated by other background sources (5355751585943066880 with  $\varpi = 0.08 \pm 0.26$  mas and 5355751585947981568 with  $\varpi = 1.13 \pm 1.20$  mas) and other source detected in 2MASS: 10172697-5354200 (5355751585943068416 with  $\varpi = 0.58 \pm 0.13$  mas).

**13545390** (5845972349875278720  $\varpi = 43.76$  mas) has associated the background object *Gaia* DR2 source 5845972349858754688 ( $\varpi = 0.09$  mas).

**15385679** is located in a very crowded region. It has associated two *Gaia* DR2 sources: the right one 5882581895192805632 ( $\varpi = 25.471$  mas) and a background source 5882581929553337216 ( $\varpi = 0.896$  mas).

**16572029**. There are three sources related that can contaminate the main one 5935776714456619008 ( $\varpi = 19.75$  mas): 5935776714456617984 ( $\varpi = 0.41$  mas) and 5935776714412775552 ( $\varpi = -0.35$  mas).

**17150219** is located in a very crowded region and three sources can contaminate the main object 597898555851221760 ( $\varpi = 38.59$  mas): 5978985562916750976 ( $\varpi = 0.05$  mas) 5978985562873939456 ( $\varpi = 1.63$  mas).

**17173128** (HD 155555C, 5811866358170877184 with  $\varpi = 32.95$  mas) the photometry might be contaminated with the ghosts from HD 155555, by a near background source (5811867835635129728 with  $\varpi = -0.14$  mas located at  $4.48''$ ) or both. 17173128 together with 2MASS J 17172550-6657039 (V824 Ara, HIP 84586) take part in a multiple system.

**17292067** is a source without parallax and proper motions, perhaps it is due to two sources detected in 2MASS very near: 17292067-5014529 and 17292064-5014574.

**18142207** the main source, 4045698737270604288 ( $\varpi = 13.99$  mas) could be contaminated by a background source 4045698737270604288 ( $\varpi = 1.57$  mas).

**18420483** the main source 6649786646225001984 ( $\varpi = 19.33$  mas) could be contaminated by a background source 6649786646219487744 ( $\varpi = 0.01$  mas).

**18435838** is a lithium-rich object that has associated four counterparts in *Gaia* DR2: 6730618549223057664 (7.07 mas) the bright and main one, 6730618549223057920 (0.12 mas), 6730618549211759104 (-1.03 mas), and 6730618549211759232 (0.58 mas). Its parallax indicates that it is a background object, and it is very likely that the bolometric luminosity is a combination of the four sources. This object must be treated with caution. We considered it as a non-member and as a multiple system.

**18465255**. 18465255 (6631685008336771072,  $\varpi = 19.78$  mas) could be contaminated by a background source, 6631685008335769728 ( $\varpi = 1.26$  mas).

**18471351**. 18471351 (4071532308311834496,  $\varpi = 16.8$  mas) could be contaminated by a background source, 4071532312630649344 ( $\varpi = -0.29$  mas).

**19082195**. 19082195 (4088823159447848064,  $\varpi = 14.4$  mas) could be contaminated by a background source, 4088823163758008192 ( $\varpi = 1.46$  mas).

**19102820** is a binary system formed by two sources separated by  $0.424''$  (Janson et al. 2017), both sources are resolved in *Gaia* DR2 and both without parallaxes: 4080460377082576128 (19102820a, the closest source 19102820a with  $G = 12.07$  mag) 4080460381377496832 (19102820b with  $G = 19.42$  mag).

**19260075.** 19260075 (6643851448094862592,  $\varpi = 20.82$  mas) could be contaminated by a background source, 6643851448094200320 ( $\varpi = -0.33$  mas).

**19560294** (1RXS J195602.8-320720, 6747467431032539008 with  $\varpi = 18.02$  mas) is a spectroscopic binary (Elliott et al. 2014).

**20004841.** 20004841 (6366726276822544768,  $\varpi = 33.96$  mas) could be contaminated by a background source, 6366726276820119040 ( $\varpi = 0.23$  mas).

**20085368** is a multiple system with two sources associated, a possible binary resolved with *Gaia* DR2 separated  $1.426''$ : 20085368a (6697858840776095616 with  $\varpi = 22.22$  mas) and 20085368b (6697858840773435776 with  $\varpi = 22.43$  mas).

**20100002** (SCR J2010-2801) is a source without parallax and proper motions, this is probably because it is a double line binary (Malo et al. 2014a).

**20434114** is a visual binary (Shkolnik et al. 2009) as we can confirm using *Gaia* DR2 data: 20434114a (6806301370519190912 with  $\varpi = 22.81$  mas) and 20434114b (6806301370521783552 with  $\varpi = 23.51$  mas).

**20415111** (AT Mic, HD 196982) is a binary system formed by two sources (Torres et al. 2006): 20415111a (6792436799475128960, TYC-7460-137-1) and 20415111b (6792436799477051904, TYC-7460-137-2) both resolved in *Gaia* DR2 and Tycho-2, but not resolved in other surveys as 2MASS or WISE.

**20560274** (AZ Cap, HD 358623) is a binary system formed by two sources separated by  $2.181''$  (Janson et al. 2017) and also it is resolved in *Gaia* DR2: 20560274a (6882838031331951488 with  $\varpi = 21.77$  mas) and 20560274b (6882838031330569856 with  $\varpi = 21.62$  mas). Also there is a very close background object: it is only detected in *Gaia* DR2: 6882838031330568960, with  $\varpi = 0.64$  mas.

**21374019** (WDS J21376+0137AB, RX J2137.6+0137) is a binary system (Mason et al. 2001) and perhaps due to that lacks of parallax and proper motions in *Gaia* DR2.

**23353085** has counterpart in *Gaia* DR2, 2392233119572232064, but lacks parallax and proper motions.

## Appendix D: 32 Ori MG as one or two associations

In this appendix, we report on a significant aspect of 32 Ori MG. In contrast to other stellar associations, the moving group appears to be composed of two sub-samples. First, we calculated the parallax PDF of the known members as it is explained in Section 4.1. We realized that some of them are non-members due to the parallax: 2MASS J05572121+0502158 ( $\varpi = 0.325$  mas) and TYC 4767-689-1 ( $\varpi = 1.759$  mas) are background sources; 2MASS J05053333+0044034 ( $\varpi = 21.255$  mas), THOR-33 ( $\varpi = 25.944$  mas) and THOR-34 ( $\varpi = 26.069$  mas) are foreground sources. We removed them and re-did the parallax PDF.

We carried out this process twice and the results are shown Figure D.1. After the first and the second iteration, we can see two maximums in the parallax PDF: around 8.93 mas and 10.21 mas and after the second iteration in 8.95 mas and 10.19 mas. It appears that the population of 32 Ori MG is composed of two populations. This fact is also remarkable with the distances released by Bell et al. (2017). We divided the two populations based on parallaxes: population 1 with  $\varpi < 9.52$  mas and population 2 with  $\varpi > 9.52$  mas.

We do not see any trend across both figures in terms of the sky distribution and the VPD of the two populations in Fig. D.2. We calculated the parallax PDF using a width validated with cross-validation, but this value may produce these two maximums in the parallax PDF and we must be cautious with our results.

In any case, we located the LDB for each sub-sample. We located the LDB at  $L_{\text{bol}} \text{LDB} = 41.8_{-14}^{+2.2} \cdot 10^{-3} L_{\odot}$  and  $T_{\text{eff}} \text{LDB} = 3157 \pm 71$  K for population 1 (Figure A.23c). The large uncertainties are due to the scarcity number of sources. For population 2, we located the LDB at  $L_{\text{bol}} \text{LDB} = 30.1_{-0.3}^{+6.1} \cdot 10^{-3} L_{\odot}$  and  $T_{\text{eff}} \text{LDB} = 3098 \pm 71$  K (Figure A.23d). However, the LDB might be located at fainter bolometric luminosities due to the scarcity of sources. The  $L_{\text{bol}} \text{LDB}$  may be able to reach  $23.418 \cdot 10^{-3} L_{\odot}$ , which would result in an age increase of about 2 Ma.

We carried out an extra analysis to analyse the 32 Ori MG population. We crossmatched the 32 Ori MG sources with the stellar groups identified in Kounkel & Covey (2019) work. The sources from Bell et al. (2017) belong to two different stellar groups: Theia 133, with log age = 7.74419 (55 Ma) and  $\varpi = 6.376$  mas, and Theia 370, with log age = 8.16773, (147 Ma) and  $\varpi = 6.552$  mas. This outcome is contrary to our previous naive population division based on parallaxes. Following the Kounkel & Covey (2019) membership criterion, we determined the LDB for these stellar associations. For Theia 133, we located the LDB at  $L_{\text{bol}} \text{LDB} = 39.4_{-1.4}^{+3.9} \cdot 10^{-3} L_{\odot}$  and  $T_{\text{eff}} \text{LDB} = 3139 \pm 71$  K. However, the uncertainties are underestimated due to the source scarcity between the faintest lithium-poor source, THOR-14B and the lithium-rich one, THOR-17B, so, the LDB would be located at  $L_{\text{bol}} \text{LDB} = 39_{-17}^{+18} \cdot 10^{-3} L_{\odot}$ , see Figure D.3a. In the same way, for Theia 370 we located the LDB at  $L_{\text{bol}} \text{LDB} = 29.8_{-2.7}^{+2.4} \cdot 10^{-3} L_{\odot}$  and  $T_{\text{eff}} \text{LDB} = 3087 \pm 71$  K, (Figure D.3b). The  $L_{\text{bol}} \text{LDB}$  uncertainties are underestimated, as is also the case with Theia 133, and the updated LDB would be  $L_{\text{bol}} \text{LDB} = 29.7_{-8.4}^{+8.3} \cdot 10^{-3} L_{\odot}$ .

There are still many unanswered questions about the real existence of this moving group: the two peaked parallax distribution together with the evidence of two stellar groups as Kounkel & Covey (2019) released. To develop a full picture of the 32 Ori MG, we need additional membership kinematic studies.

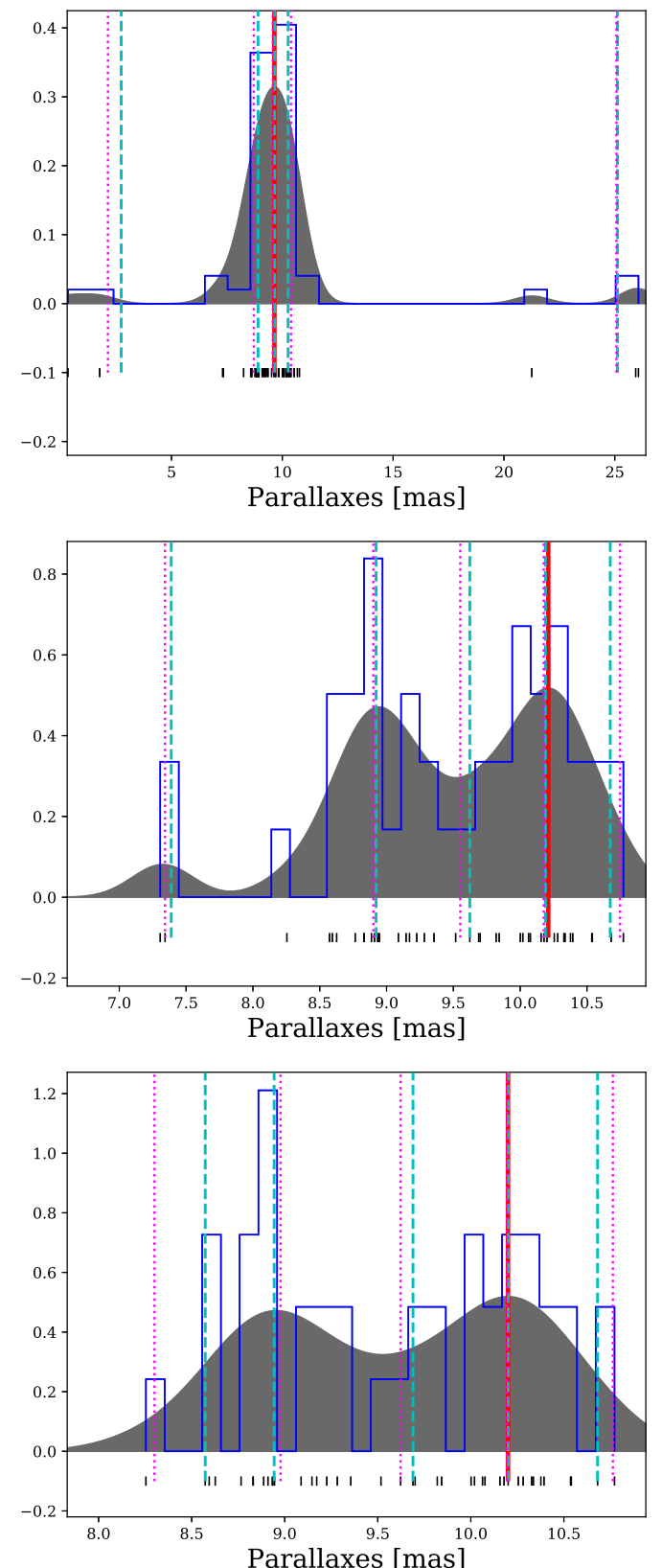


**Fig. D.1.** Parallax PDF for the 32 Ori MG known members (taken from Bell et al. 2017). The modelled PDF is shown in gray and a superimposed histogram in blue. The cyan vertical dashed lines point the percentiles of the raw data at the 2.5th, 25th, 50th, 75th, and 97.5th. The magenta vertical dotted lines point the same percentiles as before but calculated from the modelled KDE. The red vertical line shows the mode of the PDF. The small vertical black lines below the horizontal axis (below  $y = 0.0$ ) shows the parallaxes of each source. **Top:** All the previous known members from Bell et al. (2017). **Middle:** First iteration. **Bottom:** Second iteration.

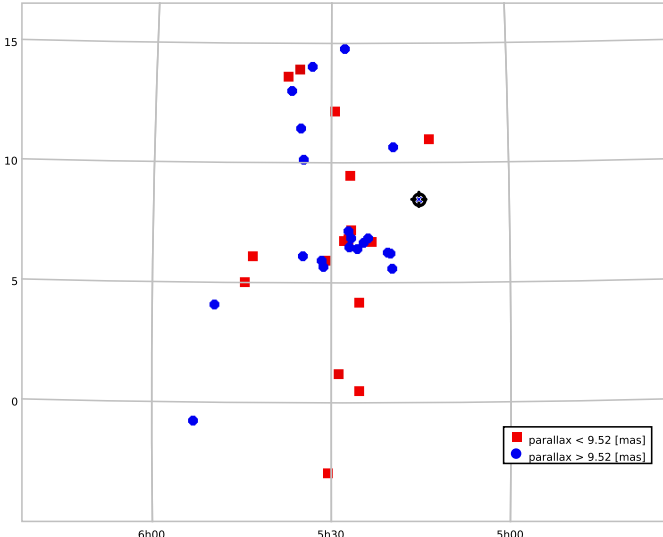


**Fig. D.2.** Spatial distribution and VPD for the 32 Ori MG members. **Top:** Spatial distribution of the known members from Bell et al. (2017), after removing some outliers. The two populations based on parallaxes are shown. **Bottom:** VPD of the 32 Ori MG, sub-sample red squares are population 1 ( $\varpi < 9.52$  mas) and blue circles population 2 ( $\varpi > 9.52$  mas). Black dashed ellipses are the Pleiades members taken from Gaia Collaboration et al. 2018b and the light grey plus symbols are the Taurus-Auriga members taken from Ducourant et al. (2005). The proper motion data have been taken from the *Gaia* DR2 catalogue, with the exception of the Taurus sample that comes from Ducourant et al. (2005).

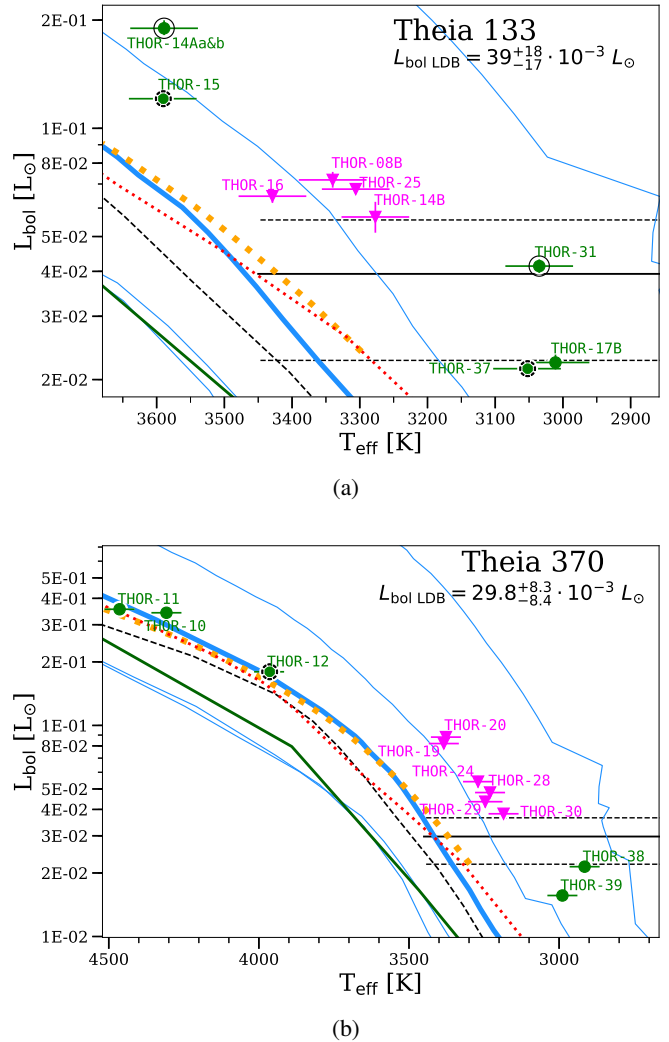


**Fig. D.3.** HRDs and the LDB for Theia 130 and Theia 370. All the symbols and lines follow the same convention as Figure A.23. The blue lines correspond to isochrones of 1, 10, 30, 100 Ma, and 1 Ga from the BT-Settl models (Allard et al. 2013), where the thick one corresponds to a 30 Ma. The figure includes a 20 Ma isochrone from D'Antona & Mazzitelli 1994 (black dashed line). **(a):** Theia 133. The figure includes a 20 Ma isochrone from Siess et al. 2000 (red dotted line) and a 18 Ma isochrone from Tognelli et al. 2011 (orange dashed dot line). Theia 133 is  $25.6^{+7.0}_{-5.5}$  Ma old using the BT-Settl bolometric luminosity-age relationship (Allard et al. 2012). **(b):** Theia 370. The figure includes a 25 Ma isochrone from Siess et al. 2000 (red dotted line) and a 20 Ma isochrone from Tognelli et al. 2011 (orange dashed dot line). Theia 370 is  $28.7^{+4.7}_{-2.6}$  Ma old using the BT-Settl bolometric luminosity-age relationship (Allard et al. 2012).

## Appendix E: Additional tables

**Table E.1.** Priors used in the distance calculation with *Kalkayotl*.

Stellar Association	prior_loc [pc]	prior_scale [pc]
Alpha Persei	175	120
NGC 1960	1 197	300
IC 4665	346	70
NGC 2547	394	135
IC 2602	152	190
IC 2391	152	115
The Pleiades	136	85
Blanco 1	237	85
The Hyades	48	90
BPMG	41	200
THMG	53	200
32 Ori MG	100	25

Table E, available at the CDS, includes calculated and collected stellar parameters for each object from each LDB sample. Parallaxes and proper motions were taken from *Gaia* DR2. Here, ‘ $\rho_{\mu_a * \mu_\delta}$ ’ is the correlation between proper motion in right ascension and proper motion in declination; ‘EW Li’ is the equivalent width of Li I at 6 707.8 Å, with its reference ‘Ref.’. Equivalent width of a lithium-poor object is given by an upper limit or without any measure; if this is the case, then it is shown as ‘-’. There are some objects that have undetermined lithium content because the data retrieved from the literature have low resolving power, low signal-to-noise ratio, or bad quality or they do not cover this part of the spectrum. These objects are marked with ‘...’. The label ‘Li rich’ indicates whether it is a lithium-rich or lithium-poor object based on ‘EW Li’: ‘Y’ indicates a lithium-rich object, ‘N’ indicates a lithium-poor object and ‘?’ indicates an object with undetermined lithium content. ‘Other’ means other remarks of the source: ‘EL’ means strong emission line object, ‘F’ is a flaring object, ‘FR’ is a fast rotator, ‘NM’ is no member (based on this work), ‘SuB’ suspected binary or multiple system, ‘CMS’ is a confirmed binary or multiple system. Then, ‘ $d_{MAP}$ ’, ‘ $d_{min}$ ’, and ‘ $d_{max}$ ’ are the distances for each object. If a source lacks a parallax, proper motions, or both in *Gaia* DR2 or it has a negative parallax, we indicated the distances with ‘-’.

We complete this appendix with tables that gather photometric bands for each stellar association, with the exception of THMG and 32 Ori MG, where all the photometric bands were recovered using VOSA. The values in parentheses have not been taken into account in the SED fitting.

**Table E.2.** Comparison between stellar parameters derived with VOSA and StarHorse.

Stellar association	$\Delta$ [M/H] [dex]	$\Delta \log g$ [dex]	$\Delta A_V$ [mag]	$\Delta T_{\text{eff}}$ [K]	$\Delta d$ [pc]	#
<i>All sources with StarHorse counterpart</i>						
Alpha Persei	$-0.19 \pm 0.19$	$-0.159 \pm 0.040$	$-0.26 \pm 0.28$	$-43 \pm 142$	$1.7 \pm 1.8$	2
NGC 1960	$0.05 \pm 0.16$	$-0.051 \pm 0.064$	$-1.67 \pm 0.48$	$-1223 \pm 608$	$-358 \pm 855$	4
IC 4665	$0.06 \pm 0.27$	$0.18 \pm 0.52$	$-0.28 \pm 0.40$	$-143 \pm 481$	$-141 \pm 683$	53
NGC 2547	—	—	—	—	—	—
IC 2602	$-0.13 \pm 0.11$	$-0.23 \pm 0.18$	$-0.43 \pm 0.34$	$-97 \pm 140$	$0.2 \pm 1.3$	10
IC 2391	$-0.17 \pm 0.26$	$-0.31 \pm 0.17$	$-0.43 \pm 0.33$	$-42 \pm 145$	$1.5 \pm 2.1$	11
The Pleiades	$-0.04 \pm 0.44$	$-0.050 \pm 0.069$	$-0.055 \pm 0.059$	$87 \pm 10$	$0.09 \pm 0.76$	2
Blanco 1	$-0.09 \pm 0.15$	$-0.268 \pm 0.097$	$-0.02 \pm 0.12$	$30 \pm 64$	$1.5 \pm 1.3$	4
The Hyades	$-0.15 \pm 0.17$	$-0.449 \pm 0.098$	$-0.15 \pm 0.11$	$38 \pm 47$	$0.07 \pm 0.36$	17
BPMG	$-0.19 \pm 0.23$	$-0.03 \pm 0.18$	$-0.53 \pm 0.77$	$-220 \pm 475$	$0.1 \pm 1.3$	101
THMG	$-0.10 \pm 0.18$	$-0.03 \pm 0.10$	$-0.29 \pm 0.51$	$-105 \pm 358$	$0.12 \pm 0.22$	108
32 Ori MG	$-0.22 \pm 0.18$	$-0.00 \pm 0.12$	$-0.49 \pm 0.77$	$-232 \pm 467$	$0.73 \pm 0.75$	24
All	$-0.11 \pm 0.23$	$-0.03 \pm 0.28$	$-0.39 \pm 0.61$	$-155 \pm 432$	$-26 \pm 293$	336
<i>Subsample with SH_GAIFLAG=="000" &amp; SH_OUTFLAG=="00000"</i>						
Alpha Persei	$-0.0011$	$-0.1198$	$0.021$	99	3.47	1
NGC 1960	$-0.1020 \pm 0.0086$	$-0.050 \pm 0.064$	$-1.44 \pm 0.33$	$-939 \pm 425$	$-30 \pm 72$	2
IC 4665	$0.13 \pm 0.26$	$0.30 \pm 0.615$	$-0.26 \pm 0.38$	$-151 \pm 476$	$-220 \pm 830$	35
NGC 2547	—	—	—	—	—	—
IC 2602	$-0.165 \pm 0.096$	$-0.23 \pm 0.17$	$-0.38 \pm 0.26$	$-91 \pm 124$	$0.3 \pm 1.3$	8
IC 2391	$-0.21 \pm 0.18$	$-0.23 \pm 0.17$	$-0.35 \pm 0.14$	$-11 \pm 72$	$1.8 \pm 2.3$	7
The Pleiades	$-0.4915$	$0.0186$	$0.003$	96	0.85	1
Blanco 1	$-0.08 \pm 0.11$	$-0.27 \pm 0.12$	$0.072 \pm 0.081$	$71 \pm 30$	$0.9 \pm 1.6$	2
The Hyades	$-0.16 \pm 0.16$	$-0.4061 \pm 0.0097$	$-0.054 \pm 0.023$	$87 \pm 29$	$-0.08 \pm 0.18$	3
BPMG	$-0.23 \pm 0.15$	$-0.03 \pm 0.18$	$-0.57 \pm 0.60$	$-216 \pm 400$	$0.16 \pm 0.29$	50
THMG	$-0.10 \pm 0.14$	$-0.047 \pm 0.078$	$-0.25 \pm 0.41$	$-82 \pm 254$	$0.13 \pm 0.14$	52
32 Ori MG	$-0.23 \pm 0.14$	$0.008 \pm 0.049$	$-0.58 \pm 0.43$	$-249 \pm 306$	$1.08 \pm 0.60$	13
All	$-0.11 \pm 0.22$	$0.00 \pm 0.34$	$-0.38 \pm 0.49$	$-147 \pm 367$	$-44 \pm 382$	174
<i>Subsample with sources considered as members after this work</i>						
Alpha Persei	$-0.19 \pm 0.19$	$-0.159 \pm 0.040$	$-0.26 \pm 0.28$	$-42 \pm 142$	$1.6 \pm 1.7$	2
NGC 1960	$0.05 \pm 0.16$	$-0.01 \pm 0.11$	$-1.67 \pm 0.49$	$-1224 \pm 608$	$-358 \pm 855$	4
IC 4665	$0.03 \pm 0.262$	$-0.01 \pm 0.11$	$-0.32 \pm 0.37$	$-115 \pm 499$	$10 \pm 15$	36
NGC 2547	—	—	—	—	—	—
IC 2602	$-0.13 \pm 0.12$	$-0.23 \pm 0.18$	$-0.43 \pm 0.34$	$-98 \pm 139$	$0.2 \pm 1.3$	10
IC 2391	$-0.26 \pm 0.16$	$-0.32 \pm 0.15$	$-0.34 \pm 0.13$	$-3 \pm 65$	$1.3 \pm 1.3$	9
The Pleiades	0.39	-0.119	-0.11	77	-0.67	1
Blanco 1	$-0.09 \pm 0.15$	$-0.268 \pm 0.097$	$-0.02 \pm 0.13$	$30 \pm 64$	$1.4 \pm 1.2$	4
The Hyades	$-0.15 \pm 0.17$	$-0.449 \pm 0.098$	$-0.15 \pm 0.11$	$38 \pm 46$	$0.07 \pm 0.36$	17
BPMG	$-0.21 \pm 0.21$	$-0.04 \pm 0.19$	$-0.45 \pm 0.61$	$-169 \pm 426$	$0.1 \pm 1.4$	75
THMG	$-0.10 \pm 0.19$	$-0.03 \pm 0.10$	$-0.26 \pm 0.42$	$-82 \pm 279$	$0.12 \pm 0.20$	107
32 Ori MG	$-0.26 \pm 0.14$	$0.021 \pm 0.068$	$-0.52 \pm 0.43$	$-201 \pm 291$	$0.89 \pm 0.76$	19
All	$-0.13 \pm 0.22$	$-0.074 \pm 0.179$	$-0.35 \pm 0.49$	$-121 \pm 377$	$-4 \pm 110$	284
<i>Members with SH_GAIFLAG=="000" &amp; SH_OUTFLAG=="00000"</i>						
Alpha Persei	$-0.0011$	-0.119	0.021	99	3.4	1
NGC 1960	$-0.1020 \pm 0.0086$	$-0.050 \pm 0.064$	$-1.44 \pm 0.34$	$-939 \pm 424$	$-31 \pm 72$	2
IC 4665	$0.11 \pm 0.22$	$0.00 \pm 0.10$	$-0.30 \pm 0.37$	$-147 \pm 519$	$6.8 \pm 4.3$	22
NGC 2547	—	—	—	—	—	—
IC 2602	$-0.165 \pm 0.095$	$-0.230 \pm 0.17$	$-0.38 \pm 0.26$	$-91 \pm 124$	$0.3 \pm 1.2$	8
IC 2391	$-0.22 \pm 0.19$	$-0.26 \pm 0.16$	$-0.37 \pm 0.14$	$-17 \pm 76$	$1.0 \pm 1.5$	6
The Pleiades	—	—	—	—	—	—
Blanco 1	$-0.08 \pm 0.10$	$-0.27 \pm 0.12$	$0.072 \pm 0.081$	$71 \pm 30$	$0.9 \pm 1.6$	2
The Hyades	$-0.16 \pm 0.16$	$-0.406 \pm 0.009$	$-0.054 \pm 0.023$	$87 \pm 29$	$-0.08 \pm 0.18$	3
BPMG	$-0.22 \pm 0.15$	$-0.04 \pm 0.19$	$-0.53 \pm 0.60$	$201 \pm 408$	$0.19 \pm 0.32$	40
THMG	$-0.10 \pm 0.14$	$-0.047 \pm 0.078$	$-0.25 \pm 0.41$	$-82 \pm 254$	$0.13 \pm 0.14$	52
32 Ori MG	$-0.23 \pm 0.14$	$0.0081 \pm 0.0490$	$-0.58 \pm 0.43$	$-249 \pm 306$	$1.08 \pm 0.60$	13
All	$-0.12 \pm 0.19$	$-0.06 \pm 0.15$	$-0.38 \pm 0.48$	$-141 \pm 365$	$0.8 \pm 9.6$	149

**Notes.** ‘#’ is the number of sources.

**Table E.3.** Comparison between stellar parameters derived with VOSA and from GES (Randich et al. 2018).

Stellar association	$\Delta \log g$ [dex]	$\Delta E(B - V)$ [mag]	$\Delta T_{\text{eff}}$ [K]	#
<i>All Gaia Collaboration et al. (2018b) sources with counterpart in Randich et al. (2018)</i>				
IC 4665	$-0.44 \pm 0.60$	0.056	$51 \pm 175$	24
NGC 2547	$-0.48 \pm 0.61$	0.040	$362 \pm 814$	87
IC 2602	$-0.22 \pm 0.64$	0.037	$329 \pm 634$	40
IC 2391	$-0.047 \pm 0.44$	0.058	$-433 \pm 4401$	23
All	$-0.36 \pm 0.61$	$0.0477 \pm 0.0093$	$206 \pm 1750$	174
<i>Sub-sample with sources considered as members after this work.</i>				
IC 4665	$-0.33 \pm 0.44$	0.056	$43 \pm 160$	18
NGC 2547	—	0.040	—	—
IC 2602	0.26	0.037	280	1
IC 2391	—	0.058	—	—
All	$-0.303 \pm 0.45$	$0.0477 \pm 0.0093$	$55 \pm 164$	19

**Notes.** ‘#’ is the number of sources. ‘ $\Delta E(B - V)$ ’ is the difference between the excess derived in Randich et al. (2018) and the one used by us.





















THOR-30	32Ori MG	82.88711	5.94994	10.01 $\pm$ 0.090	8.51 $\pm$ 0.117	-31.744 $\pm$ 0.099	-0.118	< 8 $\pm$ 37)	N	P2 99.8298.0501.573	185	38.13	36.68	39.59		
THOR-33	32Ori MG	82.99111	-3.06023	25.94 $\pm$ 0.137	18.12 $\pm$ 0.239	-50.923 $\pm$ 0.200	-0.155	< 15 $\pm$ 37)	N	CMS, NM, P2	38.5338.1438.963	024	33.83	33.03	34.73	
THOR-36	32Ori MG	80.98190	11.01744	-	-	-	-	68 $\pm$ 37)	Y	-	-	-2 970	32.99	26.35	44.37	
THOR-35	32Ori MG	79.45675	9.97281	-	-	-	-	53 $\pm$ 37)	Y	-	-	-2 964	31.79	25.26	42.97	
THOR-40b	32Ori MG	84.37503	13.49289	-	-	-	-	63 $\pm$ 37)	Y	SuB	-	-2 865	30.34	24.23	40.82	
THOR-40a	32Ori MG	84.37503	13.49289	-	-	-	-	63 $\pm$ 37)	Y	SuB	-	-2 865	30.34	24.23	40.82	
J05053333 <sup>(5)</sup>	32Ori MG	76.38901	0.7341721.25 $\pm$ 0.056	20.91 $\pm$ 0.10 $\pm$ 27.710 $\pm$ 0.075	-0.421 < 0.0	(37)	NEL, NM, P2	47.0546.8047.293	30124.94	24.67	25.20					
THOR-17B	32Ori MG	81.93353	14.76624	10.68 $\pm$ 0.122	9.07 $\pm$ 0.164	-39.587 $\pm$ 0.128	-0.191	58 $\pm$ 37)	Y	P2 93.5791.6395.833	011	22.31	21.33	23.47		
THOR-37	32Ori MG	83.75384	11.42841	10.39 $\pm$ 0.113	7.00 $\pm$ 0.174	-36.744 $\pm$ 0.128	-0.248	70 $\pm$ 37)	Y	EL, SuB, P2	96.2194.2498.353	053	21.44	20.32	22.67	
THOR-38	32Ori MG	81.12540	6.67638	9.84 $\pm$ 0.110	9.34 $\pm$ 0.182	-34.018 $\pm$ 0.147	-0.197	75 $\pm$ 37)	Y	P2 01.6499.4503.902	915	21.41	20.43	22.45		
THOR-39	32Ori MG	81.77644	6.84383	9.14 $\pm$ 0.094	6.82 $\pm$ 0.157	-29.712 $\pm$ 0.128	-0.208	65 $\pm$ 37)	Y	P1 09.3907.2611.642	989	15.63	14.95	16.38		
THOR-34	32Ori MG	83.02484	-3.02113	26.06 $\pm$ 0.071	8.22 $\pm$ 0.120	-50.961 $\pm$ 0.105	-0.248	65 $\pm$ 37)	Y	FR/SuB, NM, P2	38.3638.1538.563	040	12.52	12.18	12.86	

**References for “EW Li”:** (1) Stauffer et al. 1999; (2) Basri & Martín 1999a; (3) Zapatero Osorio et al. 1996; (4) Jeffries et al. 2013; (5) Manzi et al. 2008; (6) Jeffries et al. 2009; (7) Jeffries & Oliveira 2005; (8) Dobbie et al. 2010; (9) Barrado y Navascués et al. 2004; (10) Boudreault & Bailer-Jones 2009; (11) Marcy et al. 1994; (12) Basri et al. 1996; (13) Rebolo et al. 1996; (14) Oppenheimer et al. 1997; (15) Stauffer et al. 1998b; (16) Stauffer et al. 1998a; (17) ?; (18) Martín et al. 2000; (19) Dahm 2015; (20) Cargile et al. 2010; (21) Juarez et al. 2014; (22) Martín et al. 2018; (23) Lodieu et al. 2018; (24) ?; (25) Song et al. 2003; (26) Torres et al. 2006; (27) da Silva et al. 2009; (28) ?; (29) ?; (30) Binks & Jeffries 2014; (31) Kraus et al. 2014; (32) Malo et al. 2014b; (33) ?; (34) Binks & Jeffries 2016; (35) Shkolnik et al. 2017; (36) Malo et al. 2013; (37) Bell et al. 2017.

**Notes:** <sup>(1)</sup> Undetermined lithium detection (see Section 2.9). <sup>(2)</sup> Negative  $L_{\text{bol}}$  2.5th value, because  $\Delta F_{\text{tot}}$  is bigger than  $F_{\text{tot}}$ . <sup>(3)</sup> 01132817a and 01132817a, 01535076a and 01535076b, and 02335984a and 02335984b are binary systems only resolved in *Gaia* DR2. <sup>(4)</sup> THOR-14Aa and THOR-14Ab are two sources resolved in *Gaia* DR2 but in the rest of photometric surveys considered are blended. <sup>(5)</sup> J05053333 is the short name of 2MASS J05053333+0044034. <sup>\*</sup> Peculiar objects described in Appendix C.

“Other” column means other remarks: EL, strong emission lines in He I  $\lambda\lambda$  876 Å and  $\lambda\lambda$  876 Å; FR, fast rotator; NM, no member based in this work; CMS, confirmed multiple system; CP, contaminated photometry; SuB, suspected binary or multiple system; P1, subsample with  $\varpi < 9.52$  mas only for the 32 Ori MG; P2, subsample with  $\varpi > 9.52$  mas only for the 32 Ori MG.

**Table E.5.** Photometry for the Alpha Persei members retrieved from the literature.

Object	<i>V</i> [mag]	Ref.	<i>R<sub>c</sub></i> [mag]	Ref.	<i>I<sub>c</sub></i> [mag]	Ref.	<i>g</i> [mag]	<i>r</i> [mag]	<i>i</i> [mag]	<i>z</i> [mag]	Ref.	<i>J</i> [mag]	Ref.	<i>K'</i> [mag]	Ref.	
AP165	17.24	0.08	(1)	16.135	0.20	(5)	14.66	0.08	(1)	—	—	—	—	—	—	
					14.665	0.20	(5)	15.35	0.10	(4)	19.694	0.014	18.042	0.007	16.367	0.004
AP296	18.57	0.10	(4)	—	—	—	—	—	—	—	—	—	—	—	—	
AP284	19.44	0.10	(4)	17.810	0.20	(5)	15.60	0.10	(4)	—	—	—	—	—	—	
				19.74	0.10	(3)	17.60	0.10	(3)	—	—	20.00	0.09	17.71	0.02	
AP322	20.50	0.10	(4)	—	—	—	—	—	—	—	—	—	—	—	14.57	
AP268	20.42	0.02	(7)	—	—	—	—	—	—	—	—	—	—	—	0.055	
AP272	—	—	—	16.65	0.017	(7)	—	—	—	—	—	—	—	—	(3)	
AP275	—	—	—	19.45	0.10	(3)	17.25	0.10	(3)	—	—	—	—	—	—	
	21.10	0.10	(4)	—	—	—	17.15	0.10	(4)	—	—	—	—	—	—	
AP325	—	—	—	19.94	0.10	(3)	17.65	0.10	(3)	—	—	—	—	—	14.14	
AP318	—	—	—	19.61	0.10	(3)	17.45	0.10	(3)	—	—	—	—	—	0.05	
AP323	—	—	—	19.63	0.10	(3)	17.50	0.10	(3)	—	—	—	—	—	(3)	
AP313	—	—	—	19.68	0.10	(3)	17.55	0.10	(3)	—	—	—	—	—	14.33	
AP270	21.87	0.10	(4)	19.534	0.014	(6)	17.518	0.007	(6)	—	—	—	—	—	0.05	
				—	—	—	17.80	0.10	(4)	—	—	—	—	—	(3)	
AP300	—	—	—	20.03	0.10	(3)	17.85	0.10	(3)	—	—	—	—	14.62	0.05	
AP324	—	—	—	20.46	0.10	(3)	18.10	0.10	(3)	—	—	—	—	—	—	
AP315	—	—	—	20.54	0.10	(3)	18.20	0.10	(3)	—	—	—	—	14.80	0.05	
				20.247	0.012	(6)	18.049	0.009	(6)	—	—	—	—	15.899	0.022	
AP310	—	—	—	20.13	0.10	(3)	17.80	0.10	(3)	—	—	—	—	14.55	0.05	
AP317	—	—	—	20.14	0.10	(3)	17.85	0.10	(3)	—	—	—	—	—	14.982	
				—	—	—	—	—	—	—	—	—	—	15.00	0.03	
															(7)	

**References:** (1) Prosser 1992; (2) IPHAS DR2 (Barentsen et al. 2014); (3) Stauffer et al. 1999; (4) Prosser 1994; (5) Deacon & Hambly 2004; (6) Barrado y Navascués et al. 2002; (7) Zapatero Osorio et al. 1996; (8) SDSS DR12 (Alam et al. 2015).



**Table E.7.** Photometry for the IC 4665 members retrieved from the literature.

Object	ID JCO	<i>V</i> [mag]	<i>I<sub>c</sub></i> [mag]	<i>I</i> CFHT12 [mag]	<i>z</i> CFHT12 [mag]
P059		- -	- -	12.614	0.090
P002	JCO6-240	11.658	0.30	12.249	0.30
P065		- -	- -	12.440	0.090
JCO3-285		13.336	0.30	14.156	0.30
P331	JCO5-191	15.163	0.30	16.520	0.30
P215		- -	- -	13.705	0.090
P377	JCO7-066	14.976	0.30	16.236	0.30
JCO1-530		12.518	0.30	13.305	0.30
P020	JCO5-282	12.146	0.30	12.881	0.30
P290		- -	- -	-	-
JCO2-145		12.272	0.30	13.040	0.30
P139	JCO7-079	13.088	0.30	13.935	0.30
P030	JCO2-373	12.456	0.30	13.339	0.30
JCO2-213	JCO2-213	13.218	0.30	14.151	0.30
P107	JCO8-257	12.921	0.30	13.972	0.30
JCO1-427		13.069	0.30	14.066	0.30
P150	JCO7-021	13.126	0.30	14.145	0.30
P165	JCO4-053	13.528	0.30	14.692	0.30
JCO6-095		13.511	0.30	14.524	0.30
P060		- -	- -	12.623	0.090
P151	JCO4-226	13.781	0.30	14.781	0.30
JCO3-357		13.517	0.30	14.619	0.30
P075		- -	- -	12.697	0.090
P108	JCO5-296	13.940	0.30	15.021	0.30
P071		- -	- -	12.718	0.090
JCO9-120		14.405	0.30	15.506	0.30
P100	JCO5-179	14.407	0.30	15.647	0.30
P094	JCO5-280	14.243	0.30	15.337	0.30
JCO3-065		15.045	0.30	16.594	0.30
JCO4-337		13.913	0.30	15.296	0.30
P077	JCO9-281	14.956	0.30	16.377	0.30
P232	JCO6-111	15.993	0.30	17.773	0.30
P411	JCO4-591	16.236	0.30	18.113	0.30
JCO2-220	JCO2-220	16.420	0.30	18.443	0.30
P374	JCO4-437	16.716	0.30	18.795	0.30
JCO7-670		17.349	0.30	19.925	0.30
JCO2-637		17.200	0.30	19.945	0.30
JCO3-770		17.561	0.30	20.260	0.30
P315		- -	- -	14.876	0.090
P309	JCO5-472	16.910	0.30	19.075	0.30
P265	JCO5-521	17.062	0.30	19.356	0.30
JCO8-550	JCO8-550	17.872	0.30	20.711	0.30
P336	JCO8-364	17.530	0.30	20.152	0.30
P343	JCO5-515	17.851	0.30	20.592	0.30
P400	JCO4-459	17.893	0.30	20.470	0.30
P248	JCO8-395	17.651	0.30	20.167	0.30
P354		- -	- -	15.278	0.090
P283		- -	- -	15.474	0.090
P396	JCO7-088	15.411	0.30	17.293	0.30
P348		- -	- -	13.844	0.090
P335		- -	- -	15.741	0.090
P233		- -	- -	15.902	0.090
P350		- -	- -	16.074	0.090
P380		- -	- -	16.475	0.090
P373		- -	- -	16.116	0.090
P313		- -	- -	16.169	0.090
P344		- -	- -	16.736	0.090
A.09.30.47		- -	- -	16.650	0.090
A.10.30.316		- -	- -	15.940	0.090
A.09.30.14		- -	- -	16.236	0.090
A.08.30.655		- -	- -	16.840	0.090
P333		- -	- -	16.940	0.090
P398		- -	- -	16.706	0.090
P372		- -	- -	15.373	0.090
P338		- -	- -	16.608	0.090
A.05.30.3622		- -	- -	17.248	0.090
P238		- -	- -	16.685	0.090
		- -	- -	16.928	0.090
		- -	- -	16.314	0.070

**Notes:** “ID JCO” means the identification used in Jeffries et al. (2009).

**References:**  $V$ ,  $I_c$  are taken from Jeffries et al. (2009);  $I$ , CFHT12,  $z$ , CFHT12 from de Wit et al. (2006).



**Table E.9.** Photometry for the IC 2602 members retrieved from Dobbie et al. (2010).

Object	$I_c/I_{wp}$ ESO 845 [mag]
10443357	(15.36)
10370251	(16.35)
10422712	(14.79)
10423714	(14.85)
10420463	(14.92)
10464783	(15.00)
10452984	(15.11)
10391188	(15.36)
10420419	(15.10)
10405026	(15.33)
10430890	(15.56)
10430236	(15.80)
10401542	(15.98)
10454174	(16.36)

**Note:** photometric values in brackets correspond to cases where we encountered problems in the SED reconstruction procedure.

**References:**  $I_c/I_{wp}$  ESO 845 is taken from Dobbie et al. (2010).

**Table E.10.** Photometry for the IC 2391 members retrieved from the literature.

Object	$V$ [mag]	$R_c$ [mag]	$I_c$ [mag]	Ref.	$Z$ [mag]				
CTIO-017	19.30	0.15	17.741	0.060	15.989	0.040	(1)	- -	
PP-07	17.31	0.15	15.880	0.060	14.110	0.040	(1)	- -	
	17.21	0.34	15.890	0.310	14.110	0.280	(2)	- -	
CTIO-059	19.47	0.15	17.869	0.060	16.050	0.040	(1)	15.420	0.020
20-014	-	-	-	-	-	-	-	- -	
20-012	-	-	-	-	-	-	-	- -	
CTIO-206	-	-	17.388	0.060	15.658	0.040	(1)	- -	
20-001	-	-	-	-	-	-	-	- -	
CTIO-091	-	-	17.607	0.060	15.842	0.040	(1)	- -	
20-018	-	-	-	-	-	-	-	- -	
CTIO-205	20.21	0.15	18.276	0.060	16.211	0.040	(1)	- -	
PP-14	19.22	0.15	-	-	-	-	(1)	- -	
	19.14	0.77	17.700	0.710	15.830	0.040	(2)	- -	
CTIO-136	19.72	0.15	17.846	0.060	15.868	0.040	(1)	15.158	0.020
CTIO-074	-	-	17.662	0.060	15.876	0.040	(1)	- -	
CTIO-096	-	-	18.056	0.060	16.144	0.040	(1)	- -	
20-029	-	-	-	-	-	-	-	- -	
CTIO-192	-	-	18.256	0.060	16.286	0.040	(1)	- -	
CTIO-081	20.38	0.15	18.544	0.060	16.465	0.040	(1)	- -	
20-009	-	-	-	-	-	-	-	- -	
CTIO-026	-	-	18.353	0.060	16.352	0.040	(1)	- -	
CTIO-038	19.90	0.15	18.201	0.060	16.291	0.040	(1)	15.581	0.020
CTIO-195	-	-	18.222	0.060	16.353	0.040	(1)	- -	
CTIO-077	20.04	0.15	18.237	0.060	16.308	0.040	(1)	- -	
CTIO-202	-	-	18.448	0.060	16.391	0.040	(1)	- -	
CTIO-041	20.46	0.15	18.477	0.060	16.554	0.040	(1)	15.764	0.020
CTIO-106	-	-	18.437	0.060	16.454	0.040	(1)	- -	
CTIO-062	20.84	0.15	18.765	0.060	16.765	0.040	(1)	- -	
15-005	-	-	-	-	-	-	-	- -	
20-024	-	-	-	-	-	-	-	- -	

**References:**  $VR_cI_c$  are taken from (1) Barrado y Navascués et al. 2001 or (2) Patten & Pavlovsky 1999;  $Z$  is taken from Barrado y Navascués et al. (2001).

**Table E.11.** Photometry for the Pleiades members retrieved from the literature, part I.

Object	<i>u</i>	<i>g</i>	<i>r</i>	<i>i</i>	<i>z</i>	<i>Y</i>	<i>J</i>	<i>H</i>	<i>K</i>
	[mag]	[mag]	[mag]	[mag]	[mag]	[mag]	[mag]	[mag]	[mag]
HCG 509	(19.143 0.006)	16.846 0.002	15.575 0.001	- -	- -	- -	11.160 0.022	10.587 0.021	10.289 0.018
HCG 332	(20.278 0.005)	18.093 0.001	16.793 0.001	- -	13.797 0.050	- -	12.149 0.040	11.632 0.027	11.282 0.060
HHJ 36	(22.328 0.037)	20.153 0.005	18.773 0.003	17.012 0.001	15.950 0.051	14.919 0.050	14.290 0.050	13.736 0.050	13.436 0.050
HHJ 6	- -	21.703 0.027	20.199 0.016	17.928 0.002	16.661 0.052	15.464 0.050	14.709 0.050	14.124 0.050	13.686 0.050
HHJ 16	(23.628 0.114)	21.029 0.012	19.641 0.008	17.632 0.001	16.523 0.051	15.408 0.050	14.750 0.050	14.157 0.050	13.818 0.050
HHJ 10	- -	21.440 0.014	19.999 0.006	17.819 0.003	16.666 0.052	15.452 0.050	14.745 0.050	14.185 0.050	13.770 0.050
HHJ 18	(23.290 0.109)	20.814 0.009	19.309 0.006	17.424 0.002	16.386 0.051	15.301 0.050	14.649 0.050	14.103 0.050	13.726 0.050
HHJ 14	- -	21.426 0.012	19.772 0.004	17.700 0.002	16.583 0.051	15.445 0.050	14.776 0.050	14.220 0.050	13.845 0.050
HHJ 3	- -	- -	21.714 0.051	- -	17.140 0.071	15.943 0.031	15.144 0.041	14.514 0.041	14.110 0.060
HHJ 19	(23.422 0.112)	20.782 0.018	19.435 0.006	17.503 0.003	16.474 0.051	15.323 0.050	14.670 0.050	14.169 0.050	13.787 0.050
HHJ 11	- -	21.128 0.012	19.664 0.005	17.622 0.001	16.513 0.052	15.409 0.050	14.742 0.050	14.256 0.050	13.858 0.050
BPL 169	- -	21.228 0.011	20.213 0.005	18.395 0.001	17.127 0.053	15.926 0.050	15.218 0.050	14.677 0.050	14.267 0.050
PLZ J50	- -	22.092 0.023	20.665 0.010	18.332 0.001	17.208 0.053	15.979 0.051	15.290 0.051	14.710 0.050	14.319 0.050
PPL 15	- -	23.083 0.040	21.643 0.021	18.871 0.003	17.504 0.055	16.054 0.051	15.283 0.050	14.704 0.050	14.256 0.050
Calar 3	- -	- -	23.125 0.064	19.965 0.003	18.390 0.063	16.927 0.051	16.083 0.051	15.478 0.051	15.009 0.051
CFHT-Pl-10	- -	- -	21.015 0.017	18.685 0.001	17.484 0.054	16.209 0.051	15.450 0.051	14.883 0.050	14.476 0.050
BPL 163	- -	22.055 0.029	20.691 0.012	18.399 0.001	17.198 0.054	15.993 0.051	15.283 0.051	14.742 0.050	14.331 0.051
CFHT-Pl-9	- -	22.549 0.023	21.034 0.010	18.619 0.001	17.337 0.054	16.059 0.050	15.371 0.050	14.890 0.050	14.433 0.050
PPL 1	- -	23.046 0.075	21.845 0.031	19.098 0.002	17.656 0.056	16.189 0.051	15.360 0.050	14.782 0.050	14.305 0.050
MHObd 3	- -	24.455 0.184	22.418 0.046	19.417 0.003	17.839 0.058	16.376 0.051	15.522 0.051	14.975 0.051	14.415 0.051
CFHT-Pl-11	- -	23.068 0.027	21.529 0.011	18.909 0.001	17.602 0.055	16.271 0.051	15.548 0.050	14.992 0.050	14.570 0.051
BPL 327	- -	22.776 0.041	21.380 0.018	18.908 0.008	17.577 0.056	16.311 0.051	15.528 0.051	15.013 0.051	14.595 0.051
PPL 14	- -	22.499 0.024	21.061 0.011	18.579 0.001	17.404 0.054	16.150 0.051	15.428 0.050	14.866 0.050	14.472 0.050
CFHT-Pl-12	- -	23.539 0.074	21.759 0.029	18.983 0.001	17.437 0.054	16.027 0.051	15.172 0.050	14.569 0.050	14.088 0.050
CFHT-Pl-16	- -	24.387 0.174	22.801 0.059	19.763 0.002	18.146 0.061	16.584 0.051	15.662 0.051	14.985 0.050	14.448 0.051
CFHT-Pl-13	- -	22.742 0.042	21.385 0.020	18.902 0.001	17.569 0.055	16.255 0.051	15.515 0.051	14.971 0.051	14.507 0.051
MHObd 1	- -	23.153 0.037	21.643 0.016	18.984 0.001	17.637 0.056	16.294 0.051	15.501 0.051	14.948 0.050	14.525 0.051
Roque 13	(22.351 0.074)	- -	22.567 0.039	19.514 0.002	17.968 0.059	16.582 0.051	15.705 0.051	15.095 0.050	14.580 0.051
CFHT-Pl-18	- -	- -	22.790 0.059	19.885 0.003	18.313 0.064	16.897 0.052	15.966 0.051	15.341 0.051	14.850 0.051
IPL 43	- -	23.159 0.050	21.758 0.023	19.175 0.002	17.800 0.056	16.478 0.051	15.710 0.051	15.189 0.051	14.722 0.051
Roque 12	- -	21.451 0.019	22.414 0.029	19.540 0.002	18.145 0.062	16.668 0.051	15.930 0.051	15.365 0.051	14.935 0.051
CFHT-Pl-15	- -	24.129 0.166	22.381 0.042	19.720 0.002	18.332 0.064	16.877 0.051	15.977 0.051	15.348 0.051	14.842 0.051
Teide 1	- -	22.264 0.041	23.172 0.087	20.180 0.003	18.664 0.073	17.067 0.052	16.215 0.051	15.591 0.051	15.096 0.051
Roque 5	- -	- -	- -	21.147 0.008	19.597 0.136	17.857 0.056	16.874 0.053	16.254 0.052	15.666 0.053
Roque 25	- -	- -	- -	22.453 0.029	20.879 0.365	18.936 0.082	17.714 0.063	16.861 0.061	16.251 0.057

**Note:** photometric values in brackets correspond to cases where we encountered problems in the SED reconstruction procedure.

**References:** *ugrizYJHK* are taken from Bouy et al. (2015).

**Table E.12.** Photometry for the Pleiades members retrieved from the literature, part II.

Object	<i>V</i>		<i>I</i>		Ref.	<i>R</i>		<i>I</i>		Ref.	<i>J</i>		<i>H</i>		<i>K</i>		Ref.
	[mag]	[mag]	[mag]	[mag]		[mag]	[mag]	[mag]	[mag]		[mag]	[mag]	[mag]	[mag]	[mag]	[mag]	
HCG 509	(16.20	0.10)	(15.30	0.10)	(1)	14.89	0.21	13.20	0.12	(2)	11.10	0.02	10.59	0.02	10.26	0.04	(2)
HCG 332	(17.40	0.10)	(16.30	0.10)	(1)	15.86	0.21	14.18	0.12	(2)	12.21	0.02	11.51	0.02	11.30	0.04	(2)
HHJ 36	-	-	-	-		18.14	0.21	16.30	0.12	(2)	13.32	0.04	12.76	0.04	12.49	0.04	(2)
HHJ 6	-	-	16.99	0.20	(4)	19.34	0.21	17.15	0.12	(2)	14.67	0.04	14.06	0.04	13.71	0.04	(2)
HHJ 16	-	-	-	-		-	-	-	-		-	-	-	-	-	-	
HHJ 10	20.74	0.20	16.90	0.20	(4)	18.94	0.21	17.04	0.12	(2)	14.75	0.02	14.13	0.02	13.75	0.04	(2)
HHJ 18	19.99	0.20	16.57	0.20	(4)	-	-	-	-		-	-	-	-	-	-	
HHJ 14	-	-	16.55	0.20	(4)	-	-	-	-		-	-	-	-	-	-	
HHJ 3	21.24	0.20	17.51	0.20	(4)	19.56	0.21	17.53	0.12	(2)	15.08	0.02	14.50	0.02	14.23	0.04	(2)
HHJ 19	-	-	-	-		18.45	0.21	16.74	0.12	(2)	14.51	0.04	13.88	0.04	13.52	0.04	(2)
HHJ 11	-	-	-	-		18.77	0.21	17.02	0.12	(2)	14.55	0.04	13.87	0.04	13.65	0.04	(2)
BPL 169	-	-	-	-		-	-	-	-		-	-	-	-	-	-	
PLZJ 50	-	-	-	-		-	-	-	-		-	-	-	-	-	-	
PPL 15	22.46	0.20	17.82	0.20	(3)	-	-	-	-		-	-	-	-	14.26	-	(4)
Calar 3	-	-	18.73	0.20	(3)	21.50	0.05	19.00	0.05	(5)	-	-	-	-	15.05	-	(4)
CFHT-Pl-10	-	-	-	-		20.03	0.05	17.82	0.05	(5)	-	-	-	-	-	-	-
BPL 163	-	-	-	-		-	-	-	-		-	-	-	-	-	-	-
CFHT-Pl-9	-	-	-	-		19.89	0.05	17.71	0.05	(5)	15.35	0.02	-	-	14.39	0.09	(4)
PPL 1	-	-	-	-		-	-	-	-		-	-	-	-	14.34	-	(4)
MHObd 3	-	-	18.27	0.20	(4)	-	-	-	-		15.43	0.04	14.89	0.06	14.36	0.07	(4)
CFHT-Pl-11	-	-	-	-		20.12	0.05	17.91	0.05	(5)	-	-	-	-	-	-	-
BPL 327	-	-	-	-		-	-	-	-		-	-	-	-	-	-	-
PPL 14	21.56	0.20	17.73	0.20	(3)	-	-	-	-		-	-	-	-	14.43	-	(4)
CFHT-Pl-12	-	-	-	-		20.47	0.05	18.00	0.05	(5)	-	-	-	-	-	-	-
CFHT-Pl-16	-	-	-	-		21.22	0.05	18.66	0.05	(5)	-	-	-	-	-	-	-
CFHT-Pl-13	-	-	-	-		20.23	0.05	18.02	0.05	(5)	-	-	-	-	-	-	-
MHObd 1	-	-	17.95	0.20	(4)	-	-	-	-		15.54	0.04	-	-	14.50	0.10	(4)
Roque 13	-	-	-	-		-	-	-	-		-	-	-	-	-	-	-
CFHT-Pl-18	-	-	-	-		21.38	0.05	18.81	0.05	(5)	-	-	-	-	-	-	-
IPL 43	-	-	-	-		-	-	-	-		-	-	-	-	-	-	-
Roque 12	-	-	-	-		-	-	-	-		-	-	-	-	-	-	-
CFHT-Pl-15	-	-	-	-		20.96	0.05	18.62	0.05	(5)	-	-	-	-	-	-	-
Teide 1	-	-	18.80	0.20	(4)	-	-	-	-		-	-	-	-	15.12	-	(4)
Roque 5	-	-	-	-		-	-	-	-		-	-	-	-	-	-	-
Roque 25	-	-	-	-		-	-	-	-		-	-	-	-	-	-	-

**References:** (1) Hambly et al. (1993); (2) Steele et al. (1993); (3) Stauffer et al. (1994); (4) Stauffer et al. (1998a); (5) Bouvier et al. (1998).

**Table E.13.** Other identifiers for the Pleiades LDB sample.

Object	Other id.	DANCe id.	$P_B$	$P_O$	$P_{\text{emb}}$
HCG 509	HHJ430, V V692 Tau,	J035630.43+241718.5	0.1576	0.173278	0.855910
HCG 332	SK362, HHJ339, V348 Tau,	J034826.59+231129.7	0.8864	0.658344	0.188240
HHJ 36		J034915.62+232249.3	0.9995	0.999211	0.007580
HHJ 6		J034142.41+235457.2	0.9994	0.998524	0.956460
HHJ 16		J034729.93+233315.1	0.9987	0.998292	0.001710
HHJ 10		J034835.19+225342.3	0.9926	0.999504	0.129050
HHJ 18		J034306.50+221749.3	0.9992	0.995568	0.000370
HHJ 14		J034512.62+235345.1	0.9982	0.999732	0.000860
HHJ 3		J034850.44+224430.0	0.9528	0.949897	0.959530
HHJ 19		J033715.61+262929.7	0.9996	0.999109	0.000350
HHJ 11		J034600.92+221229.5	0.9973	0.995850	0.000720
BPL 169	Lick-Pl-1	J034814.31+241550.4	0.9967	0.992284	0.000240
PLZJ 50	LZJ-50	J034356.00+253625.3	0.9997	0.998895	0.000000
PPL 15	NPL35, SHF48, IPMBD23	J034804.67+233930.0	0.9958	0.991150	0.998700
Calar 3	BPL 235, CFHT-PI-21	J035125.57+234521.4	1.0000	0.999295	0.000080
CFHT-Pl-10		J034432.32+252518.1	0.9998	0.999390	0.000000
BPL 163		J034758.04+220650.9	0.9997	0.999461	0.000000
CFHT-Pl-9	MHObd6, BPL202	J034915.12+243622.5	0.9998	0.999738	0.000001
PPL 1		J034541.27+235409.8	1.0000	0.998807	0.999937
MHObd 3	DH174	J034154.16+230504.8	1.0000	0.997389	0.999995
CFHT-Pl-11	Roque16, BPL152	J034739.01+243622.3	0.9999	0.999725	0.000001
BPL 327		J035523.07+244905.1	0.9996	0.997954	0.000000
PPL 14		J034434.30+235124.5	0.9995	0.999317	0.000000
CFHT-Pl-12	BPL 294	J035355.12+232336.1	0.9999	0.993790	1.000000
CFHT-Pl-16		J034435.16+251342.9	1.0000	0.998915	1.000000
CFHT-Pl-13	Teide2, BPL254, PLIZ3, PLZJ46, BRB11	J035206.71+241600.6	0.9999	0.999026	0.000018
MHObd 1		J034452.42+243649.3	0.9997	0.995210	0.001083
Roque 13	BPL79 SHF19	J034550.66+240903.4	0.9998	0.982541	0.976441
CFHT-Pl-18		J035323.13+231920.3	0.0000	0.018494	0.046708
IPL 43		J034623.73+225016.4	1.0000	0.999724	0.000000
Roque 12		J034819.01+242512.7	0.9995	0.997343	0.000000
CFHT-Pl-15		J035512.61+231737.3	0.0000	0.119570	0.000400
Teide 1	BPL137, NPL39	J034717.93+242231.5	1.0000	0.999102	0.000120
Roque 5		J034422.45+233901.2	1.0000	0.999098	0.000001
Roque 25		J034830.74+224450.2	0.9999	0.998689	0.000643

**Notes:** “Other id.” compiles other identifiers from several previous works. “DANCe id.” are the DANCe (Bouy et al. 2015) identifier.  $P_B$  is the membership probability calculated in Bouy et al. (2015).  $P_O$  is the membership probability calculated in Olivares et al. (2018).  $P_{\text{eqm}}$  is the equal-mass binaries membership probability calculated in Olivares et al. (2018).

**Table E.14.** Photometry for the Blanco 1 members retrieved from the literature.

Object	<i>B</i>		<i>V</i>		$I_c$		$z_{\text{CFHT12}}$		$K_s$		Ref.
	[mag]	[mag]	[mag]	[mag]	[mag]	[mag]	[mag]	[mag]	[mag]	[mag]	
JCO-F18-88	16.085	0.070	14.829	0.022	13.345	0.003	-	-	11.622	0.029	(2)
JCO-F2-78	-	-	-	-	14.339	0.018	-	-	12.373	0.038	(2)
JCO-F13-55	-	-	-	-	15.757	0.033	-	-	13.594	0.069	(2)
JCO-F9-190	-	-	-	-	16.230	0.089	-	-	14.114	0.140	(2)
CFHT-BL-16	-	-	-	-	18.330	0.050	17.60	0.05	15.460	0.030	(1)
CFHT-BL-22	-	-	-	-	18.500	0.050	17.72	0.05	15.580	0.030	(1)
CFHT-BL-25	-	-	-	-	18.650	0.050	17.86	0.05	15.570	0.030	(1)
CFHT-BL-38	-	-	-	-	19.010	0.050	18.19	0.05	15.890	0.030	(1)
CFHT-BL-36	-	-	-	-	18.990	0.050	18.10	0.05	15.860	0.030	(1)
CFHT-BL-24	-	-	-	-	18.540	0.050	17.80	0.05	15.570	0.030	(1)
CFHT-BL-29	-	-	-	-	18.800	0.050	17.99	0.05	15.750	0.030	(1)
CFHT-BL-45	-	-	-	-	19.330	0.050	18.44	0.05	16.040	0.030	(1)
CFHT-BL-43	-	-	-	-	19.110	0.050	18.28	0.05	15.960	0.030	(1)
CFHT-BL-49	-	-	-	-	19.490	0.050	18.57	0.05	15.910	0.030	(1)

**References:**  $BVI_cK$  are taken from (1) Cargile et al. (2010) and Cargile et al. (2009),  $I_c z_{\text{CFHT12}} K_s$  from (2) Moraux et al. (2007).

**Table E.15.** Photometry for the Hyades members retrieved from the literature.

Object	$I_{\text{CFHT12}}$	$z_{\text{CFHT12}}$	$J$		Ref.	$H$	$K$
	[mag]	[mag]	[mag]	[mag]			
Hya03	-	-	-	15.647	0.076	(1)	-
Hya08	-	-	-	15.463	0.044	(1)	-
Hya11	-	-	-	-	-	-	-
Hya09	-	-	-	-	-	-	-
Hya10	-	-	-	16.506	0.059	(1)	-
Hya12	-	-	-	16.778	0.069	(1)	-
2M0418	-	-	-	-	-	-	-
CFHT-Hy-1	(12.87 0.06)	12.33	0.06	-	-	-	10.37 0.05
CFHT-Hy-2	(12.91 0.06)	12.45	0.06	-	-	-	10.50 0.05
CFHT-Hy-4	(13.35 0.06)	12.78	0.06	-	-	-	10.74 0.05
CFHT-Hy-3	(13.29 0.06)	12.70	0.06	-	-	-	10.60 0.05
CFHT-Hy-10	(14.17 0.06)	13.57	0.06	-	-	-	11.49 0.05
CFHT-Hy-5	(13.40 0.06)	12.85	0.06	-	-	-	10.95 0.05
CFHT-Hy-7	(13.53 0.06)	13.01	0.06	-	-	-	11.03 0.05
CFHT-Hy-6	(13.48 0.06)	12.96	0.06	-	-	-	11.07 0.05
CFHT-Hy-8	(13.59 0.06)	13.07	0.06	-	-	-	11.16 0.05
CFHT-Hy-11	(14.39 0.06)	13.82	0.06	-	-	-	11.74 0.05
CFHT-Hy-13	(14.52 0.06)	13.81	0.06	-	-	-	11.51 0.05
CFHT-Hy-9	(13.59 0.06)	12.97	0.06	-	-	-	11.00 0.05
CFHT-Hy-12	(14.44 0.06)	13.80	0.06	-	-	-	11.74 0.05
CFHT-Hy-16	(14.81 0.06)	13.99	0.06	-	-	-	11.62 0.05
CFHT-Hy-15	(14.78 0.06)	14.07	0.06	-	-	-	12.02 0.05
CFHT-Hy-14	(14.71 0.06)	14.02	0.06	-	-	-	11.95 0.05
CFHT-Hy-17	(14.83 0.06)	14.12	0.06	-	-	-	12.07 0.05
CFHT-Hy-18	(15.20 0.08)	14.45	0.06	-	-	-	12.03 0.05
Hya01	-	-	-	-	-	-	-
CFHT-Hy-19	(17.49 0.10)	16.31	0.08	-	-	-	12.90 0.05
Hya06	-	-	-	15.462	0.081	(1)	-
Hya05	-	-	-	15.729	0.071	(1)	-
Hya02	-	-	-	-	-	-	-
Hya04	-	-	-	15.595	0.044	(1)	-
Hya07	-	-	-	15.956	0.073	(1)	-
CFHT-Hy-20	(21.58 0.08)	19.79	0.06	17.02	0.05	(2)	16.51 0.05
CFHT-Hy-21	(22.16 0.10)	20.80	0.08	18.48	0.05	(2)	17.36 0.05

**Note:** photometric values in brackets correspond to cases where we encountered problems in the SED reconstruction procedure.

**References:**  $I_{\text{CFHT12}} z_{\text{CFHT12}} HK'$  are taken from Bouvier et al. 2008;  $J$  is taken from two different works: (1) Lodieu et al. 2014 and (2) Bouvier et al. 2008.



**Table E.19.** Stellar properties for the Hyades LDB sample. Quantities obtained from Martín et al. (2018).

Object	$\varpi$ [mas]	$\mu_\alpha \cos(\delta)$ [mas yr $^{-1}$ ]	$\mu_\delta$ [mas yr $^{-1}$ ]	$\rho_{\mu_\alpha * \mu_\delta}$	$d_{MAP}$ [pc]	$d_{min}$ [pc]	$d_{max}$ [pc]	$T_{\text{eff}}$ $\chi^2$ [K]	$L_{\text{bol}}$ [10 $^{-3} L_\odot$ ]	$-\Delta L_{\text{bol}}$ [10 $^{-3} L_\odot$ ]	$+\Delta L_{\text{bol}}$ [10 $^{-3} L_\odot$ ]	
Hya03	-	-	-	-	-	48	39	57	2 298	0.168	0.094	0.272
Hya08	-	-	-	-	-	45	36	54	1 993	0.173	0.081	0.315
Hya11	-	-	-	-	-	50	43	57	1 512	0.146	0.101	0.203
Hya09	-	-	-	-	-	57	49	65	2 000	0.169	0.124	0.221
Hya10	-	-	-	-	-	58	50	66	1 771	0.124	0.086	0.171
Hya12	-	-	-	-	-	56	48	64	1 811	0.112	0.069	0.170

**Notes:** The distances were taken from Martín et al. (2018). Bolometric luminosities were calculated using these distances.

**Table E.20.** Stellar properties for the Hyades LDB sample. Quantities obtained from Lodieu et al. (2019b).

Object	$\varpi$ [mas]	$\mu_\alpha \cos(\delta)$ [mas yr $^{-1}$ ]	$\mu_\delta$ [mas yr $^{-1}$ ]	$\rho_{\mu_\alpha * \mu_\delta}$	$d_{MAP}$ [pc]	$d_{min}$ [pc]	$d_{max}$ [pc]	$T_{\text{eff}}$ $\chi^2$ [K]	$L_{\text{bol}}$ [10 $^{-3} L_\odot$ ]	$-\Delta L_{\text{bol}}$ [10 $^{-3} L_\odot$ ]	$+\Delta L_{\text{bol}}$ [10 $^{-3} L_\odot$ ]			
Hya11	39.1	16.3	138.1	13.3	-19.4	9.0	-	29	17	192	1 512	0.052	0.016	2.308
Hya09	20.6	2.5	76.3	2.9	-17.7	1.5	-	48	40	67	2 000	0.123	0.083	0.237
Hya10	28.5	3.9	120.2	3.6	-12.2	5.5	-	34	28	50	1 771	0.043	0.028	0.102
Hya12	24.1	2.1	100.2	1.9	-15.1	2.0	-	41	35	50	1 811	0.061	0.038	0.108
2M0418	25.8	2.9	141.5	2.7	-45.7	2.3	-	38	32	51	1 814	0.043	0.029	0.077
Hya02	17.7	2.0	116.4	2.0	-26.9	1.5	-	56	47	75	1 970	0.250	0.164	0.461
CFHT-Hy-20	30.8	3.0	141.3	2.9	-14.5	3.2	-	32	27	41	1 070	0.020	-0.006	0.079
CFHT-Hy-21	33.5	12.7	82.1	9.8	-15.5	8.6	-	32	20	180	1 811	0.010	0.004	0.341

**Notes:** The parallaxes and proper motions were taken from Lodieu et al. (2019b). Bolometric luminosities were calculated using these distances derived from these parallaxes.

**Table E.21.** Other identifiers for the 32 Ori MG LDB sample.

Object	Other id.	<i>Gaia</i> DR2	Pan-STARRS DR1	DENIS	2MASS	WISE
THOR-14Ab	-	3341625126275164032	124680838233826256	-	J05351761+1354180	J053517.61+135417.5
THOR-14Aa	-	3341625121978020736	124680838233826256	-	J05351761+1354180	J053517.61+135417.5
THOR-27	1RXS J052748.7+064544	3238015740407127936	116110819523395693	-	J05274855+0645459	J052748.55+064545.6
THOR-17Ab	1RXS J052743.4+144609	3389908598858685696	125720819297114362	-	J05274313+1446121	J052743.14+144611.7
THOR-17Aa	1RXS J052743.4+144609	3389908598860532096	125720819297114362	-	J05274313+1446121	J052743.14+144611.7
THOR-18	SCR0522-0606	3209175443035096320	100670806696252366	J052240.7-060623	J052240.69-0606238	J052240.71-060624.1
THOR-15	1RXS J053306.7+140011	3389588293083264128	124810832739272523	-	J05330574+1400365	J053305.75+140036.1
THOR-20	1RXS J051930.4+103812	3386885525999518976	120760798726343064	-	J05192941+1038081	J051929.42+103807.8
THOR-21	1RXS J052515.0+003027	3221837251438378624	108600813132168138	J052515.1+003023	J052515.17+003022.9	
THOR-19	1RXS J052532.3+062534	3237973752806799360	115710813856941688	-	J05253253+0625336	J052532.54+062533.4
THOR-23	1RXS J054424.7+050153	3320524914022156288	114040861019574221	-	J05442447+0502114	J054424.48+050211.4
THOR-08B	-	3341556922194703232	124310843359170753	-	J05372061+1335310	J053720.61+133530.6
THOR-04B	-	3221986647580887296	109470821687871498	-	J05284050+0113333	J052840.51+011333.1
THOR-25	-	3387055125667571968	121150783596485041	-	J05132631+1057439	J051326.31+105743.7
THOR-16	1RXS J054304.3+060646	3333228804511967488	115330857648411792	-	J05430354+0606340	J054303.55+060633.9
THOR-42	CRTS J055255.7-004426	3218460376351485056	107110882322151434	-	J05525572-0044266	J055255.72-004426.9
THOR-14B	1RXS J053516.6+135404	3341625087618092672	124680838177560174	-	J05351625+1353594	J053516.26+135359.0
THOR-22	1RXS J054926.3+040541	3319628434087776000	112910873597313009	-	J05492632+0405379	J054926.32+040537.6
THOR-24	-	3237508762467678336	114700799332671108	-	J05194398+0535021	J051943.99+053501.8
THOR-28	-	3337724677494561792	119360817036292205	-	J05264886+0928055	J052648.86+092805.2
THOR-32	-	3334165249117507968	116640816697198918	-	J05264073+0712255	J052640.73+071225.3
THOR-29	1RXS J052315.0+064412	3241048880671509888	116070808099508068	-	J05231438+0643531	J052314.38+064352.9
THOR-31	-	3341238918520502912	123610841538702692	-	J05363692+1300369	J053636.92+130036.6
THOR-26	-	3216793104408043520	104470826061711843	-	J05302546-0256255	J053025.47-025625.6
THOR-30	1RXS J053132.6+055639	3237712515716135936	115140828871060328	-	J05313290+0556597	J053132.90+055659.4
THOR-33	-	3216729878197029120	104320829911177914	J053157.8-030336	J05315786-0303367	J053157.96-030338.3
THOR-36	1RXS J052355.2+110110	3339253170454118272	121220809819151364	-	J05235565+1101027	J052355.65+110102.5
THOR-35	-	3338707537810168448	119960794567877802	-	J05174962+0958221	J051749.63+095821.8
THOR-40b	-	3341538436653898240	124190843750381886	-	J05373000+1329344	J053730.00+132934.1
THOR-40a	-	3341538436655619840	124190843750381886	-	J05373000+1329344	J053730.00+132934.1
J05053333	-	3228582201223411200	108880763889481502	J050533.3+004403	J05053333+0044034	J050533.35+004403.2
THOR-17B	-	3389908598860532224	125710819335229833	-	J05274404+1445584	J052744.05+144558.0
THOR-37	-	3339935348702249472	121710837538854498	-	J05350092+1125423	J053500.93+112542.0
THOR-38	-	3238048652740273408	116010811254372030	-	J05243009+0640349	J052430.10+064034.6
THOR-39	-	3238063569162793472	116210817764702963	-	J05270634+0650377	J052706.34+065037.4
THOR-34	-	3216753556349327232	104370830250595136	J053205.9-030115	J05320596-0301159	J053205.95-030116.4